INFORMATION TO USERS

This manuscript has been reproduced from the microfilm master. UMI films the text directly from the original or copy submitted. Thus, some thesis and dissertation copies are in typewriter face, while others may be from any type of computer printer.

The quality of this reproduction is dependent upon the quality of the copy submitted. Broken or indistinct print, colored or poor quality illustrations and photographs, print bleedthrough, substandard margins, and improper alignment can adversely affect reproduction.

In the unlikely event that the author did not send UMI a complete manuscript and there are missing pages, these will be noted. Also, if unauthorized copyright material had to be removed, a note will indicate the deletion.

Oversize materials (e.g., maps, drawings, charts) are reproduced by sectioning the original, beginning at the upper left-hand corner and continuing from left to right in equal sections with small overlaps.

Photographs included in the original manuscript have been reproduced xerographically in this copy. Higher quality 6" x 9" black and white photographic prints are available for any photographs or illustrations appearing in this copy for an additional charge. Contact UMI directly to order.

Bell & Howell Information and Learning
300 North Zeeb Road, Ann Arbor, MI 48106-1346 USA

UMI®
800-521-0600

Constitutive Analysis and Extrusion Modeling of 6061 Alloy and Particulate Composite

Edward Herba

A Thesis

in

The Department

of

Mechanical Engineering

Presented in Partial Fulfilment of the Requirements

for the Degree of Master of Applied Science at

Concordia University

Montreal, Quebec, Canada

September 1997

ABSTRACT

Constitutive Analysis and Extrusion Modeling of 6061 Alloy and Particulate Composite

Edward Herba

Isothermal hot torsion tests were performed on 6061 Al alloy followed by a constitutive analysis of the alloy and three metal matrix composites previously tested (10%Al_2O_3/6061, 15%SiC/6061, and 20%Al_2O_3/6061). The flow stresses decrease with increasing deformation temperature and the rate at which this occurs increases with percent reinforcement. Flow stress as a function of strain rate and temperature was suitably represented by the hyperbolic sine and Arrhenius equations for the alloy and metal matrix composites. Extrusion modeling was performed for the four materials using the constitutive equations above and the finite element software DEFORM which is a registered trademark of Scientific Forming Technologies Corporation. Simulations were run for various extrusion conditions and the output was placed in table format to facilitate interpolation. The simulation results were validated with comparison to real life extrusions and modeling of other researchers. The results showed that an increase in billet temperature, a reduction in ram speed, or a reduction in extrusion ratio, had the effect of reducing the ram load. According to the modeling results, maximum strain rate and maximum extrudate velocity increased with increasing ram speed or extrusion ratio and were not influenced by the percent reinforcement or initial billet temperature. The rate of

decrease of ram load as a function of time (distance) increased with increasing percent reinforcement as a result of deformation heating.

ACKNOWLEDGEMENTS

The author wishes to express his gratitude and appreciation to his supervisor Dr. Hugh J. McQueen who provided guidance and encouragement throughout this research project. Special thanks goes to Dr. W.S. Ghaly who gave advice concerning the heat transfer boundary conditions in the finite element model. The author would also like to thank Dr. Paul Wycliffe of Alcan International Kingston Research and Development Center for providing rapid chemical analyses of the torsion specimens throughout the project. He would also like to thank Ms. Marylène Sauerborn for her helpful suggestions in the use of DEFORM and UNIX. Special thanks to Mr. Joe Hulet for installing extra hard drive space on the SGI machine.

PREFACE

The work described in this thesis was carried out by the author in the Department of Mechanical Engineering, Concordia University and the Department of Mining and Metallurgy, McGill University between September 1995 and August 1997, under the supervision of Dr. H.J. McQueen. No part of this thesis has been previously submitted for a degree at this or any other university. The data used in this thesis if they are from other research work have been duly acknowledged in the text. A list of references is included at the end of this thesis. Part of this thesis was presented at the 35th Annual Conference of Metallurgists in Montreal, Canada, in August 1996.

TABLE OF CONTENTS

CHAPTER

Page

Page

CHAPTER

LIST OF FIGURES

Page

FIGURE

FIGURE

Page

Page

FIGURE

FIGURE

Page

LIST OF TABLES

NOMENCLATURE

A: Material Constant [s^{-1}]

A_B: Cross Sectional Area of Billet [m^2]

c_p: Specific Heat [J/Kg-°K]

F_{id}: Ideal Deformation Load [N]

h: Interface heat transfer coefficient [W/m^2 °C]

h_{air}: Convection heat transfer coefficient [W/m^2 °C]

k: Thermal Conductivity [N/ sec °C]

k: Shear Strength [Mpa]

k: Flow stress in shear [MPa]

k_f: Flow Stress [MPa]

L: Billet Length [mm]

L_o: Specimen Gauge Length [mm]

m: Strain Rate Sensitivity Exponent

m: Shear Factor

N: Number of Turns

n: Stress Exponent in the Hyperbolic Sine equation

n: Slope

n': Stress Exponent in the Power Law equation

n": Strain Hardening Exponent

p: Ram Pressure [MPa]

$\dot{q}$: Rate of Heat Generation [W/m^3]

Q_{HW}: Activation Energy for Hot Working [kJ/mol]

R: Universal Gas Constant [8.314 J/mol-K]

R: Extrusion Ratio

r: Specimen Gauge Radius [mm]

s: Slope

T_{BS}: Billet temperature at interface [°C]

T_{Bi}: Billet temperature at point i [°C]

T_{ca}: Container temperature [°C]

T_m: Melting temperature [°C]

T_{max}: Maximum temperature reached during extrusion [°C]

T_o: Temperature of outer surface of container [°C]

T_{TS}: Tool temperature at interface [°C]

T_∞: Ambient temperature [°C]

V_{max}: Maximum extrudate velocity [mm/s]

W_{id}: Ideal Work of Deformation [N-m]

Z: Zenèr-Hollomon Parameter [s^{-1}]

α: Stress Multiplier [MPa^{-1}]

γ: Torsional Strain

ε: Equivalent Strain

$\dot{\varepsilon}$: Strain Rate [s^{-1}]

η: Efficiency Factor

ρ: Density [kg/m^3]

σ: Equivalent Flow Stress [Mpa]

$\bar{\sigma}$: Average Stress [MPa]

τ: Shear Stress [MPa]

τ_n: Stress normal to surface [MPa]

τ_s: Friction Stress [MPa]

Γ: Torsional Moment [Nm]

μ: Coefficient of Coulombic Friction

1. INTRODUCTION

The objective of this research is to model the extrusion of 6061 aluminum alloy and the metal matrix composites (MMC) reinforced with either particles of silicon carbide (SiC) or alumina (Al_2O_3) using the commercial software DEFORM which is a registered trademark of Scientific Forming Technologies Corporation. First, the project involves the determination of the hot working behavior of 6061 Al and the MMC with 6061 as the matrix. Torsion tests were performed to study the flow characteristics of these materials at hot working temperatures and strain rates. Secondly, the flow stress data was fitted to the Arrhenius relationship linking flow stress with temperature and strain rate. The constitutive constants were used as the material flow stress input for the simulation of the extrusion. Thirdly, boundary conditions for the simulation of the extrusion process were implemented. Simulations were performed for four materials (6061 Al, 10% Al_2O_3/6061, 15% SiC/6061 and 20% Al_2O_3/6061) varying the extrusion parameters to determine under what conditions the MMCs could be extruded with the same breakthrough pressure as the alloy. Varying the extrusion parameters also provided information on how these parameters affect the extrusion process.

General characteristics of aluminum matrix composites and 6061 aluminum alloy will be discussed in chapter 2. A literature review of hot working, the softening mechanisms in the alloy and MMCs, the extrusion process and the modeling of this process is presented in chapter 3. A description of hot torsion testing and the finite element model is given in chapter 4. The results are presented in chapter 5 in two parts.

Part one presents the hot deformation behavior of the composites and the alloy as well as the constitutive analysis. Part two presents the simulation results which include the temperature, strain rate, stress, velocity profiles and load versus time curves. The modeling results are discussed in chapter 6 along with comparisons to others' work. Finally, conclusions are drawn concerning the constitutive analysis and modeling of these four materials based on the present work.

2. GENERAL MATERIAL CHARACTERISTICS

2.1 Aluminum-Matrix Composites

Aluminum alloys reinforced with particles of either Al_2O_3 or SiC are engineered to overcome the limitations of conventional aluminum alloys. These composites offer improved strength and stiffness as well as greater wear resistance and improved high temperature properties. In MMC, the metal acts as the matrix and its main function is to transfer and distribute the load to the reinforcement. The transfer of load depends on the strength of the interface bond between the matrix and reinforcement. Aluminum alloys are often used as the matrix because aluminum possesses good corrosion resistance, high thermal conductivity, low density and medium strength. The reinforcements are usually ceramic particles or fibers which possess high yield strength, high Young's modulus but are quite brittle. SiC and Al_2O_3 are commonly used as a reinforcement material for the aluminum matrix since they possess the necessary properties and are compatible with the matrix [1, 2].

The reinforcements can either be continuous filaments, discontinuous whiskers or particles. Continuous filaments provide the greatest improvement in strength but are expensive to fabricate and implement as a reinforcement. Discontinuous whiskers are very fine fibers which result in the highest strength of discontinuously reinforced MMC but are also expensive to manufacture. Particle reinforcement offers a cheaper alternative to fiber reinforcement. They are the least expensive reinforcement to manufacture and result in isotropic properties in the MMC. The drawbacks are inferior strength and stiffness

compared to the fiber reinforcement. When particles are used as the reinforcement, conventional forming methods such as extrusion, forging and rolling can be used to form the metal to the desired shape. Table 2.1 summarizes the advantages and disadvantages of continuous and discontinuous reinforcements [1, 2].

'✓' denotes the advantage and '×' the disadvantage

Advantages	Discontinuous Reinforcement	Continuous Reinforcement
Isotropy	✓	×
Orientable Properties	×	✓
Formability, Ductility	✓	×
Fabrication Costs	✓	×
Material Cost	✓	×
Recyclability	✓	×
Reinforcement Efficiency	×	✓

Table 2.1: Advantages and disadvantages of discontinuous and continuous reinforcements [2]

2.1.1 Fabrication of Particulate Reinforced MMCs

The two main methods of bulk particulate MMC production are: liquid metal fabrication (casting) and powder metallurgy (P/M). The casting method has the advantages of low cost and near-net shape components can be produced requiring little or no machining. Some of the drawbacks of casting are the difficulty in wetting all the particles and preventing clustering. Due to the low cost, the aluminum industry uses the Direct Chill (DC) casting process to produce bulk material such as extrusion ingots and sheet ingots. It should be noted that the term "ingot" signifies an object produced by casting, whereas "billet" is a more general term for a round or square object fabricated by casting, rolling, forging, sintering or hot isostatically pressing [3, 4].

Many of the problems associated with casting such as clustering and poor wetting are avoided in powder metallurgy. The P/M method involves mixing the pre-alloyed powder with the ceramic reinforcement, followed by pressing and sintering and finally consolidating into a form. Powder metallurgy is more suited for the production of complex or small objects rather than large billets or slabs. The main drawbacks of P/M are high cost and low productivity [3, 4, 5].

2.1.2 Processing and Applications of Particulate Reinforced MMCs

In most cases, the discontinuously reinforced MMC requires subsequent deformation regardless of the method used to produce the billet. Processes such as extrusion, forging, rolling and machining operations can be used to form the MMC to its final shape. Extrusion of the billet leads to improvements in the elastic modulus and

strength, although usually at the expense of ductility. Defects can occur during extrusion such as surface cracking or tearing which affect the quality of the final product [6].

MMCs using 6061 Al as the matrix are used on a small scale in the automotive industry for such components as driveshafts, cylinder linings, and brake rotors. Success in the auto industry is strongly dependent on the cost of fabrication therefore being able to produce MMC using traditional techniques such as DC casting and then hot extrusion is crucial. Other applications of 6061 MMCs include bicycle frames and components. It is well suited for bicycle applications since light weight, corrosion resistance, high strength and stiffness are required. However, the use of MMCs in mass produced products is still quite sparse. To increase the use of MMCs, production costs must be lowered by improving the manufacturing processes [7, 8].

2.2 Fabrication, Processing and Applications of 6061 Aluminum alloy

6061 Al is usually produced by ingot metallurgy (I/M) techniques but P/M methods may be used for oxide dispersion strengthening as explained above for the MMCs. Controlling the size and distribution of the precipitate Mg_2Si is done by subsequent heat treatments where the billet is heated above its solution temperature (529°C), then slowly cooled in the furnace until the deformation temperature is reached. The as-cast ingot with no heat treatment will contain large segregated particles imparting a high hot strength and a low ductility. A billet that has been homogenized followed by slow cooling will contain equilibrium particles resulting in medium hot strength and high

ductility. If a homogenized billet is cooled rapidly to room temperature, fine particles will form on reheating resulting in a high hot strength and medium ductility [9].

The 6xxx series aluminum are used for the majority of extrusions because of its good ductility and satisfactory strength. 6061 Al can be age hardened to improve its properties and is used mainly for structural applications. It can be welded with relative ease and has sufficient strength to be used as vehicular frames for land transport [10].

3. LITERATURE REVIEW

Hot Working is considered to be deformation at a temperature above 0.5 T_m (melting temperature, °K) and a strain rate between 10^{-3} to 10^{3} s^{-1}. The strains may vary from 0.1 to as high as 50. At these temperatures, most metals have a low flow stress and a high ductility. Both dynamic and static softening mechanisms take place during the hot working process which includes the preheating, deformation and subsequent cooling. Hot working is employed because metals can be subjected to large and rapid changes in shape without cracking. The continuing need for improved processes and products generates increased interest in high temperature deformation [11, 12]

3.1 Restoration Mechanisms in Hot Working

Deformation of any metal will cause an increase in dislocation density within its grains, which serves to strain harden the material and ultimately leads to fracture if some form of restoration mechanism is not active to relieve the buildup of stresses. Since hot working is generally performed in several steps, the restoration processes can be divided into two main groups: those occurring during deformation are referred to as dynamic and those taking place in the absence of stress or strain on the material are termed static. In any shaping process, one or all of the following restoration mechanisms may be active [13]:

(i) Dynamic Recovery (DRV)

(ii) Dynamic Recrystallization (DRX)

(iii) Static Recovery (SRV)

(iv) Static Recrystallization (SRX)

The major factor that determines whether recovery or recrystallization will take place during hot working is the stacking fault energy (SFE). The factors that trigger and control recovery and recrystallization is dependent on both material properties and parameters such as temperature, strain, strain rate and time after deformation [11, 12]. For metals with high SFE, such as aluminum, only DRV is observed. For metals with low or moderate SFE, DRX takes place above a critical strain. In aluminum MMC, DRX has been observed to a small extent [14, 15].

3.1.1 Dynamic Recovery (DRV)

Dynamic recovery is the basic mechanism that leads to the annihilation of pairs of dislocations during deformation and the rearrangement of the remainder into low energy, low angle subgrain boundaries (SGB). Figure 3.1a shows a characteristic flow curve of a material that undergoes DRV where strain hardening occurs up to a steady state plateau. The flow curve can be divided into three distinct stages. In the first stage, the elastic strain increases from zero to the yield stress. During the second stage, strain hardening takes place but the rate of strain hardening diminishes and this is reflected in the continuously decreasing slope. The amount of work hardening decreases as temperature is raised and the strain rate lowered. In the third stage, the work hardening rate becomes

zero and the flow stress has leveled off to a steady state value. A balance is reached between the work hardening and recovery; dislocations are annihilated at the same rate as they are generated. In hot working, the temperature, strain rate, and the flow stress are constant in the steady state regime. In practice, the flow curve may decrease after the plateau has been reached as a result of either deformation heating or precipitate coarsening [11, 12].

3.1.2 Dynamic Recrystallization

Dynamic recrystallization (DRX) occurs in metals where dislocations cannot leave their slip planes easily to undergo DRV or where there is sufficiently high dislocation density caused by localized stress to act as a recrystallization nuclei. The flow curve for a material that exhibits DRX has a peak, followed by gradual softening as shown in figure 3.1b. In region 1, there is an accumulation of dislocations which eventually nucleate DRX. In region 2, a peak is reached, after which new grains grow rapidly containing a lower dislocation density than the original grains, therefore softening occurs. Region 3 shows the steady state condition when repeated deformation and recrystallization occurs [14, 15, 16].

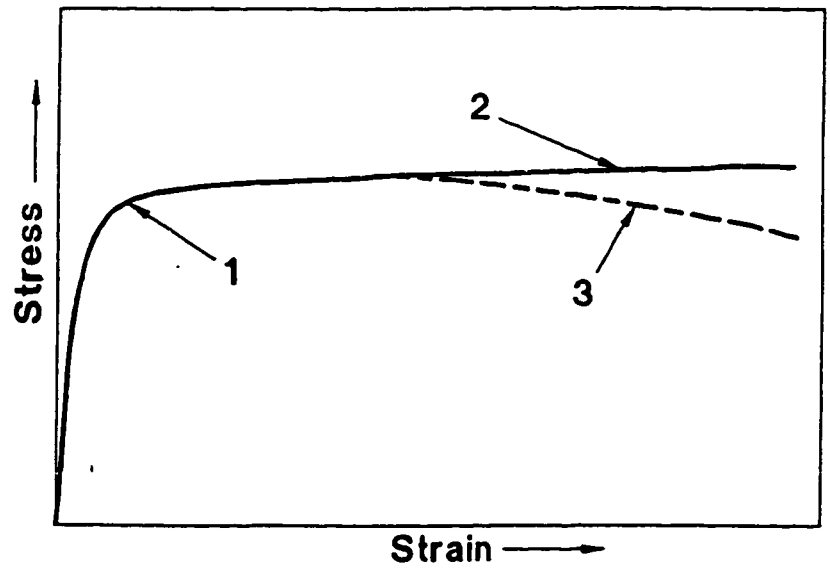

(a)

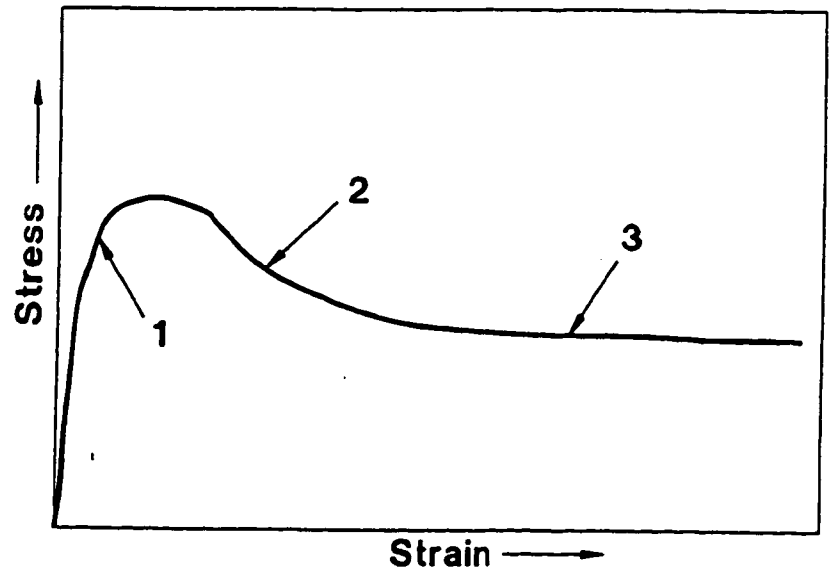

(b)

Figure 3.1: Dynamic softening curves: (a) Typical dynamic recovery curve, (b) Typical dynamic recrystallization curve [2]

3.1.3 Interdependence of Stress, Strain Rate and Temperature

There are a number of mathematical expressions that have been utilized over the years that describe the relationship between flow stress, strain rate and temperature. Without discussing the origin of the equations, three common hot working equations are as follows:

$$A\sigma^{n'} = \dot{\varepsilon} \exp(Q_{Hw}/RT) = Z \quad (3.1)$$

$$A \exp(\beta\sigma) = \dot{\varepsilon} \exp(Q_{Hw}/RT) = Z \quad (3.2)$$

$$A [\sinh(\alpha\sigma)]^n = \dot{\varepsilon} \exp(Q_{Hw}/RT) = Z \quad (3.3)$$

where Ai, α, β, n, n' : empirical constants

Z : Zener Hollomon Parameter

Q_{Hw} : Activation Energy for Hot Working

R : Universal gas constant (8.31 J/mol K)

The power law equation (equation 3.1) works satisfactorily for low stresses and the value of n' is around 4 to 5. The exponential law equation (equation 3.2) is useful for high stresses. The hyperbolic sine law (equation 3.3) covers the entire stress range and is used to relate flow stress to temperature and strain rate in the present work. The Arrhenius term for temperature indicates a thermally activated mechanism involving crystal defects such as dislocations and vacancies (11, 12, 17, 18).

3.2 Softening Mechanisms in 6061Al and Particle Reinforced MMC

In order to extrude a metal, the flow stress must be lowered to a point where the ductility is sufficient to prevent fracture. For the flow stress to be lowered, the softening mechanisms must be triggered and aided by thermal energy. This section will discuss the softening mechanisms in the 6061 alloy and the MMC reinforced with either Al_2O_3 or SiC particles.

3.2.1 Softening Mechanisms in 6061Al

To understand the softening mechanisms in the MMC, one must first comprehend the strengthening mechanisms in the alloy itself. Strain hardening is caused by the interaction of dislocations generated by the sources in the form of pile-ups, tangles, cell structure and forest theory. 6061 aluminum contains Mg and Si as its main alloying elements which combine to form equilibrium Mg_2Si particles. The size of the particles and their resistance to being cut by dislocations determines whether or not they cause rapid strain hardening. Medium to large soft particles do not interact much with dislocations therefore there is little strain hardening. However, very large rigid particles, usually associated with particle cutting, cause a rise in yield strength but very little increase in strain hardening. Very small particles (usually the result of a particle having been cut) cause a rise in yield strength but very little strain hardening. Whereas, small particles that are not being cut produce clusters of dislocations around them. This is known as the "Orowan Mechanism" which results in rapid strain hardening. To counter the effects of strain hardening, restoration mechanisms must be triggered [13, 19].

During the extrusion process, which includes preheating, deformation and cooling, the microstructure changes. In the preheating stage, the billet is heated to a sufficiently high temperature which will allow the precipitates to dissolve during extrusion. It was found by Kaneko et al. that the hot workability of Al-Mg-Si alloys could be improved by submitting the as cast billet to a two stage heat treatment. The two step heat treatment consisted of a first step of heating for the purpose of homogenizing and solutionizing, followed by water quenching and then a second step of heating at a temperature near the hot working temperature as to obtain optimum dispersion of precipitates. Fast cooling and rapid reheating can lead to dynamic precipitation with very high flow stresses [9]. A fast cooling rate and slow reheating resulted in a fine precipitates which imparted high ductility to the alloy whereas a slow cooling rate (furnace cooled) resulted in coarse precipitates which lowered the deformation resistance. The flow stress can be reduced by having the precipitates dissolve during the extrusion process and this is more easily accomplished if the precipitate is fine. Therefore, to achieve high ductility and low deformation resistance a compromise in particle size must be made and it is best met by applying the heat treatment in two steps [20, 21, 22].

Plastic deformation of the billet is possible due to the movement of dislocations. As the temperature is increased the dislocations have increased mobility which permits them to annihilate or rearrange in a lower state of stress. During the hot working of aluminum alloys, dynamic recovery is the primary softening mechanism. The high level of DRV in aluminum prevents a high dislocation density from forming thus making nucleation of new grains impossible. Although some researchers believe that dynamic

recrystallization (DRX) is possible in aluminum alloys, McQueen has shown strong evidence to the contrary [17, 18, 23, 24, 25].

3.2.2 Softening Mechanisms in the MMC

The softening mechanisms in the MMC differ from the alloy, since the addition of relatively large reinforcement particles affects the dislocation behavior. The rigid reinforcement particles strengthen the matrix, not by pinning the dislocation directly but rather by generating a high dislocation density around themselves. Upon cooling, differences in the coefficients of thermal expansion between the matrix and the reinforcement cause a high stress field around the particles and a high dislocation density is found around the particles and for some distance into the matrix [26, 27]. As the MMC is hot worked , DRV is the principle softening mechanism, but DRX does occur to a small extent. DRX is possible in the MMC because nuclei can form in the regions of high dislocation density around the reinforcements. Xia and McQueen observed DRX grains at the particle/ matrix interface and in the aluminum matrix. Contrary to what occurs in low SFE metals, the DRX grains do not completely replace the original matrix in the steady state condition [28, 29, 30]. Lloyd found that dynamic recrystallization occurred only at high strain rates and high temperatures. TEM examination by McQueen et al. of 6061 Al reinforced with either Al_2O_3 or SiC revealed that in comparison to the bulk alloys, the dislocation substructures were very inhomogeneous, ranging from subgrains to high uniform distributions in which small cells developed as nuclei. All these distributions shifted to lower densities as temperature rose and strain rate fell. It was also found that

for any deformation condition, composites with higher particle content have greater strength, dislocation density and heterogeneity. It is this heterogeneity as well as the particles which prevents DRX from overrunning the entire matrix [15, 16, 31].

Research has also shown that as temperature is increased, the matrix can flow around the particles more easily and particle degradation is reduced. Researchers at UBC looked into the extrusion conditions that caused particle cracking and void formation in the present MMC and found that both of these problems could be suppressed by increasing the initial billet and die temperature and the extrusion speed within the boundaries of the incipient melt line [32].

3.3 Extrusion

3.3.1 Extrusion Basics

The hot extrusion process consists essentially of preheating a cylindrical billet of the metal, placing it in a container of slightly larger diameter, closed at one end by a ram, and at the other end by a die. The temperature to which the billet is pre-heated depends on the material to be extruded, the ram speed, and the extrusion ratio. The die has an opening with the cross section of the required product. As the ram is moved inward, the billet is forced under sufficiently large pressure to extrude through the opening in the die as illustrated in figure 3.2a [29, 33].

Hot extrusion is used to produce long, straight metal products of constant cross section, such as bars and tubes. For the hot extrusion of aluminum and aluminum metal matrix composites (MMC), no lubricant is used and hence only nonlubricated extrusion

will be discussed in the present work. With no lubricant on the billet, container, or die, it can produce complex sections with mirror surface finishes and close dimensional tolerances. A flat faced shear die is usually used in non-lubricated hot extrusion for which there are two methods: direct extrusion (forward) and indirect extrusion (backward). In forward extrusion, the ram travels in the same direction as the extruded section, and the billet moves relative to the container. (See figure 3.2a.) In backward extrusion a die is pushed against the billet to extrude the metal in the opposite direction and the billet does not move relative to the container [29, 33]. (Figure 3.2b)

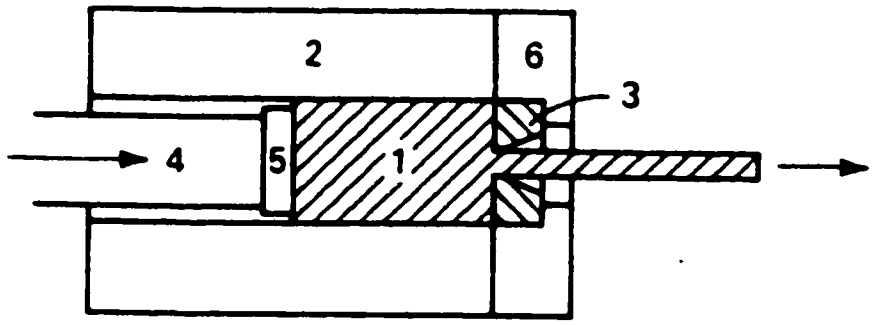

(a)

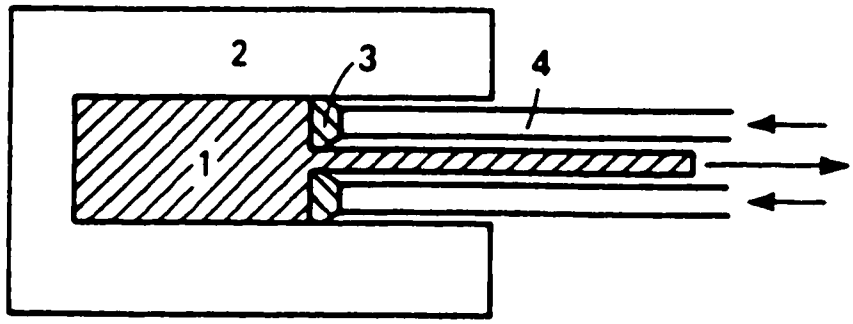

(b)

Figure 3.2: Basic Methods of Extrusion: (a) Forward (direct), (b) Backward (indirect). Object 1=billet, 2=chamber, 3=die, 4=stem, 5=dummy block, 6=die holder [29].

A typical sequence of operations for direct extrusion is as follows:

- The heated billet and dummy block are loaded into the container.
- The force of the ram first upsets the billet against the container, then forces the metal to flow through the die. During extrusion, a thin shell of material may be left on the container walls. Extrusion is stopped when only a thin disk of the billet remains in the container.
- The die is separated from the container; the ram pushes out the dummy block, the butt, the extruded section and the die.
- The butt is sheared off from the extrusion at the die face and discarded.
- The die, the container, and the ram are returned to their initial loading positions.

One of the most important characteristics of the extrusion process is the ram load versus ram stroke curve. As will be discussed later, this relation depends on the cross sectional area of the billet, the extrusion ratio, the friction between the billet and the tooling, and the flow stress which is dependent on strain rate and the temperature field. Typical load versus stroke curves for direct and indirect extrusion are illustrated in figure 3.3. The curve for direct extrusion shows that the load initially increases very rapidly as the billet upsets to fill the container with a further increase in pressure for the extrusion to begin. After the maximum load has been reached, the extrusion pressure falls as the billet length decreases until a minimum is reached. The curve decreases first due to deformation and frictional heating lowering the flow stress in the zone in front of the die and a reduction in friction as less billet contacts the wall. The sharp increase that occurs at the

end is due to the difficulty in extruding the thin remaining disk in which the metal must flow radially toward the die aperture under high friction [29].

The load versus stroke curve for the indirect extrusion method is much flatter than for direct extrusion as shown in figure 3.3a. Since there is no relative movement between the billet and the chamber wall, frictional forces are significantly less and less heat is generated [29].

The physical meaning of the load versus stroke curve for direct extrusion can be explained by figure 3.3b. Part A represents work done on the billet due to initial upsetting and part B represents work needed to initiate deformation. Part C is the ideal work of deformation and part D is the work needed to overcome friction and internal shearing of the metal [33].

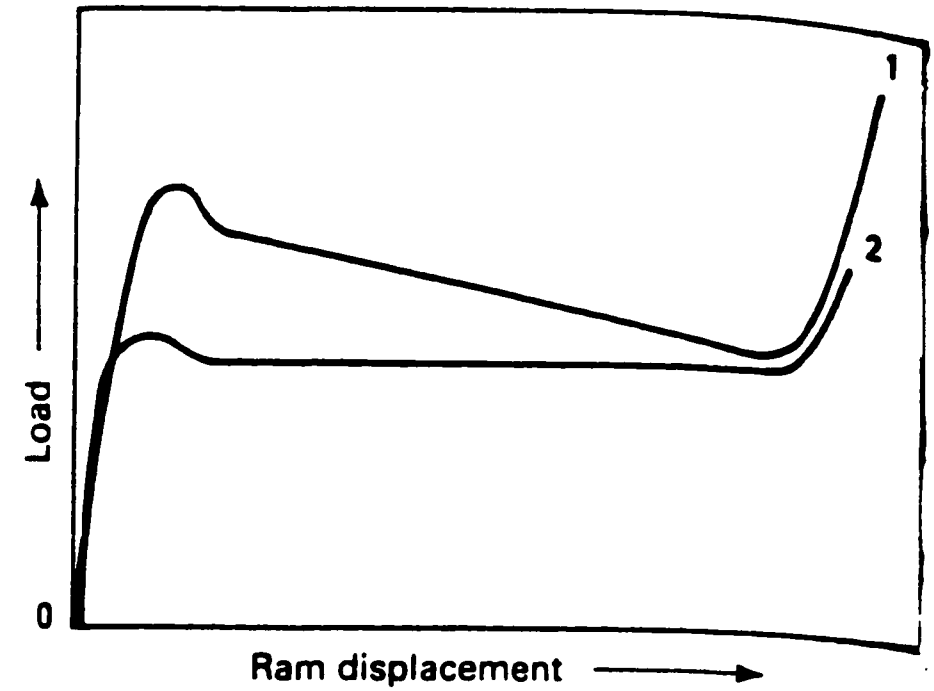

(a)

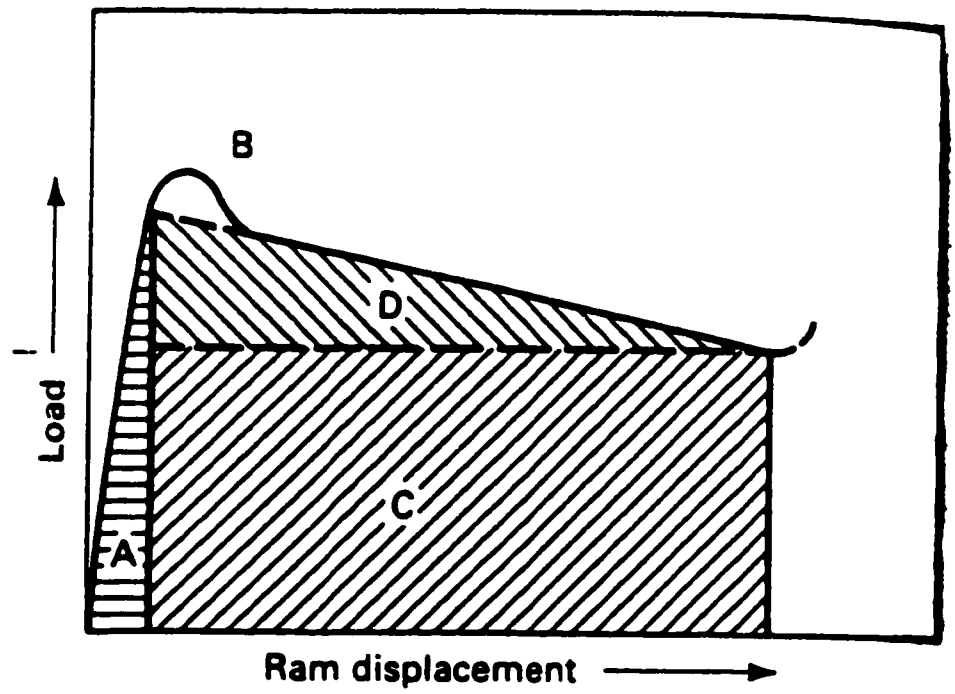

(b)

Figure 3.3: Typical load versus ram displacement curves (a) Load vs displacement for extrusion, Curve 1=direct extrusion, curve 2= indirect extrusion (b) Division of work done during extrusion [29].

3.3.2 Extrusion Limits

The extrusion process involves a compromise between highly productive extrusion conditions and material or press limits. Industry's objective is to run with the highest ram speed, largest extrusion ratio and lowest initial billet temperature in order to maximize production. The limits of extrusion ratio, preheat temperature, ram pressure, and ram velocity for a given extrusion press can be represented in an extrusion limit diagram. (Figure 3.4) The extrusion limit diagram can be drawn to represent the extrusion ratio possible with any given preheat temperature and extrusion pressure. The higher the preheat temperature, the lower the strength of the metal and the higher the extrusion ratio possible for any given extrusion pressure. This is designated by a rising line above which extrusion would be impossible [34].

If extrusion is carried out under adiabatic conditions where all heat is trapped in the billet (corresponding to very high extrusion speeds) then all the work of deformation would go into raising the temperature of the metal. Thus for an increasing extrusion ratio there is a decreasing preheat temperature such that the deformation heating of the billet will just cause incipient melting (melting of the alloy constituent having the lowest melting temperature). If the extrusion is carried out so slowly that all the heat generated during deformation is dissipated without raising the billet temperature, then the preheat temperature could be in theory just below the melting temperature of the metal so that the limit curve would move to a vertical position corresponding to zero ram velocity. The two situations just discussed are the extremes of the process and in reality the extrusion process has a number of curves between the isothermal and adiabatic conditions depending

on ram velocities. Figure 3.4 shows that the extrusion variables must be carefully chosen in order to extrude the metal without melting or causing any defects to occur. It can be seen that the window of possible extrusions can be expanded by either increasing ram pressure, or decreasing velocity [28, 35].

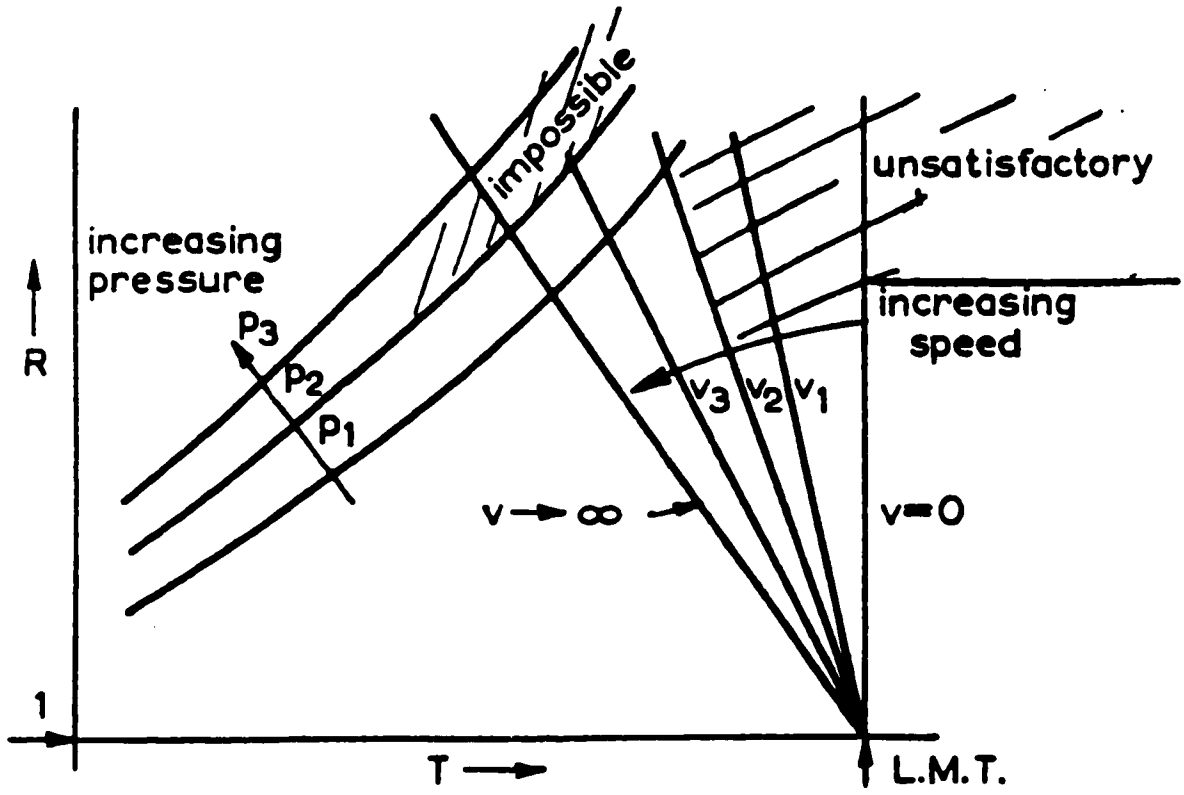

Figure 3.4: Extrusion limit diagram. R=ram speed, T=temperature, p=ram pressure, v=ram velocity [28]

3.3.3 Effects of Friction

Frictional stresses can be calculated in one of two ways depending on the type of forming operation. The two friction models are constant shear and coulomb friction. Constant shear (sticking friction) is used mostly for bulk-forming operations and is presented in equation 3.4. Coulomb (sliding) friction is used for sheet metal forming operations since it most closely resembles the type of friction encountered in this process and is presented in equation 3.5.

Constant shear factor friction; $$\tau_s = mk = m \cdot \frac{\bar{\sigma}}{\sqrt{3}} \qquad (3.4)$$

where m=shear factor
$\bar{\sigma}$=flow stress
k=flow stress in shear
τ_s=friction stress

Coulomb friction; $$\tau_s = \mu \cdot \tau_n \qquad (3.5)$$

where τ_s=friction stress
τ_n=stress normal to surface
μ=friction coefficient

In equation 3.5, the maximum allowable frictional stress is flow stress in shear, ie.,

$$\tau_s \leq k = \frac{\bar{\sigma}}{\sqrt{3}} \qquad (3.6)$$

Therefore μ in equation 3.5 cannot exceed $\frac{1}{\sqrt{3}}$=0.577 since the material shears at this point. The value of "m" in equation 3.4 has a range from 0 to 1, where m=1 corresponds to shearing.

Friction varies considerably depending on the metal being extruded , the lubricant being used (if any) and thermal effects. Under sticking conditions the friction component of the extrusion load is strongly temperature dependent as is the shear stress of the material. Krysko and Lui [36] demonstrated the effect of billet temperature on friction in figure 3.5. The load versus stroke curve for the low temperature decreases much more rapidly than the high temperature curve therefore it can be concluded that friction equal to shear stress is very temperature dependent. At higher temperatures less pressure is required since the flow stress is decreased [37].

Another major role of friction is its effects on the quality of the end product. This can be illustrated by examining the metal flow patterns that occur under three friction conditions; minimum friction, sticking friction and excessive friction. These cases are shown in figure 3.6, type A, B, and C respectively. Type A flow represents no friction between the billet and the container, and the material flows uniformly before exiting the die. At the bottom corner of the container, the outside of the billet is held back while the center of the billet flows easily. Type A flow is not possible in direct extrusion because friction is always present. Type B flow represents friction between the billet and container and results in metal flow distortion occurring earlier, resulting in a deeper pipe and more non-uniform flow stresses. A dead metal zone occurs in the corner of the container which can trap impurities and that may be released toward the end of the extrusion thus entering into the extruded part. This back end defect occurs to a greater extent in type C flow where excessive friction exists and the dead zone extends further back into the container [33, 37, 38, 39].

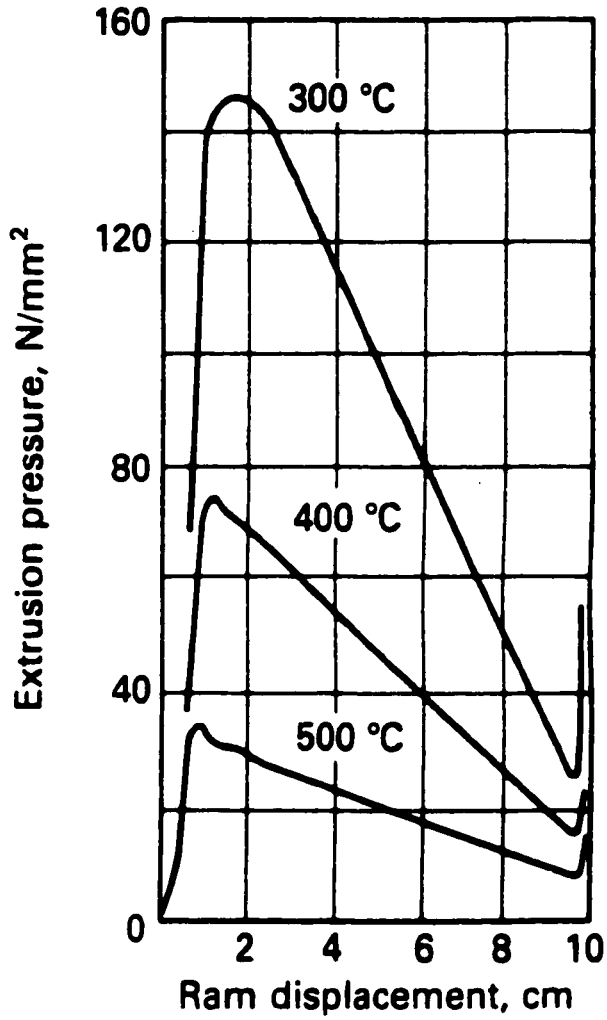

Figure 3.5: Influence of the temperature on the variation in extrusion pressure with ram displacement [37].

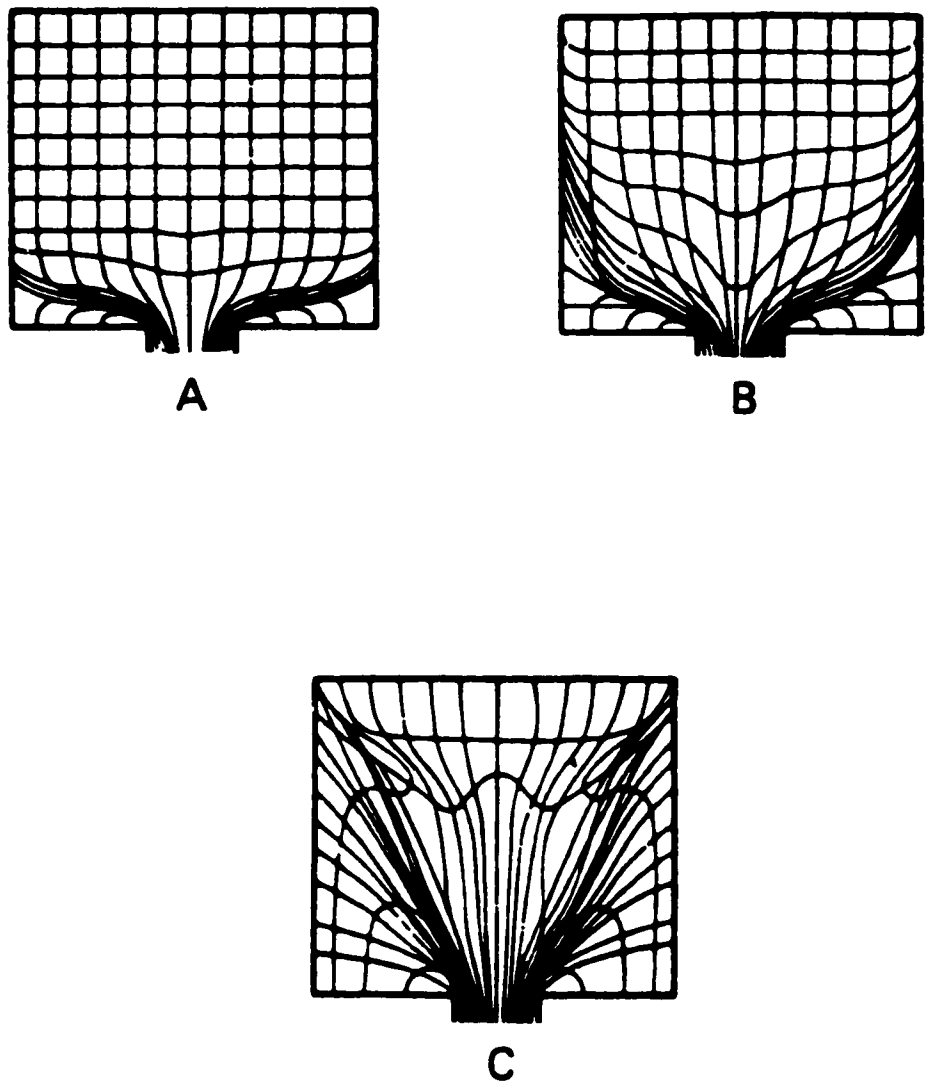

Figure 3.6: Flow Patterns in Extrusion: (a) Minimal friction, (b) Moderate friction, (c) High friction [37]

3.3.4 Extrusion Defects

Much of the research work done on extrusion has focused on the causes of defects in the extruded material and methods of preventing them from occurring. It is not in the scope of this thesis to discuss all the possible extrusion defects and what has been done to solve them, but rather to simply demonstrate some of the results of choosing improper extrusion conditions. It has been found that several extrusion defects have a thermal origin. Funnels, pipes, back-end defects, and fir-tree cracking are defects that are associated with the friction between the billet and the container. Since friction is rather sensitive to the temperature field, these defects are therefore also affected accordingly. It is therefore possible to modify the process parameters so as to reduce the occurrence of such defects [33, 40].

The defect known as fir tree cracking is initially triggered by excessive deformation and frictional heating which result in hot short cracks. These cracks are then opened up by the friction stresses. One way to control this defect is to reduce the extrusion speed thereby reducing the exit temperature. Controlling the exit speed and therefore the extrudate temperature will also affect the metallurgical quality of the end product [33].

3.4 Extrusion Modeling

Several methods for calculating the deformation load required to extrude a material have been developed over the years. They differ from each other in the assumptions made, the complexity of analysis, the theoretical basis and the degree of approximation of the solution. The early methods that will be briefly described are:

elementary analysis and plasticity analysis using slip line field theory. The approach used today is the finite element method which allows for a more sophisticated model producing more accurate results. The finite element method used by others and in the present work will be discussed following a summary of the early modeling methods.

3.4.1 Method of Elementary Ideal Analysis

The solution obtained by the method of elementary analysis has proven to be the most useful in practice because of its simplicity. The main assumption made is that the billet deforms homogeneously. This assumption is made based on the fact that considerable calculation would be required to obtain a solution if the non-uniform distribution of strain and deformation energy in the deformation zone is accounted for. Tresca's yield criterion is used for the dimensional state of stresses of $\sigma_1>\sigma_2>\sigma_3$ that develops in each element of volume under the applied load therefore this results in a lower bound solution. Frictionless deformation of an element requires ideal deformation load, F_{id}. The ideal work of deformation is derived to be [37]:

$$F_{id} = \frac{W_{id}}{L} \tag{3.7a}$$

$$F_{id} = A_B \cdot k_f \cdot \ln\frac{L_1}{L_o} \tag{3.7b}$$

$$F_{id} = A_B \cdot k_f \cdot \ln\frac{A_B}{A_i} \tag{3.7c}$$

$$F_{id} = A_B \cdot k_f \cdot \ln R \tag{3.7d}$$

$$\frac{p}{2k_f} = \frac{F_{id}}{A_B \cdot 2k_f} = \frac{\ln R}{2} \tag{3.7e}$$

where W_{id} = Ideal work of deformation

L = Billet length at any time

L_o = Original billet length

L_1 = Final billet length

A_B = Cross sectional area of the billet

k_f = Flow stress

R = Extrusion ratio

p = Ram pressure

When R=3 in equation 3.7e, $p/2k_f=0.55$ which is the minimum value possible since it is assumed that the material deforms ideally.

3.4.2 The Slip-Line Theory

The shear line theory or also known as slip-line theory is a method of calculating the stresses involved in a forming operation based on the graphical construction of a field of lines which indicate the direction of principle shear stress. It is one of the most accurate upper bound solutions which must be distinguished from lower bound solutions derived in the previous section. In the method of "statically admissible stress field" the stress required to deform is determined by keeping every point just below yielding. In reality, the forces required are higher than this, therefore this results in a lower bound solution. The upper bound solution is obtained by choosing possible flow lines to predict the direction of material flow. It is known that no matter the flow pattern chosen, the material will find a

path that requires less work, therefore this results in an upper bound solution. The shear line theory makes the following assumptions about the material:

1. Plastic- Rigid material (no strain hardening)
2. Axes of principle strains & stresses coincide.
3. Plastic strains proportional to stress deviation.
4. Volume constant

A shear line field is drawn consisting of a grid of orthogonal lines which indicate the directions of planes of maximum shear stress. Equations are derived which show the variation of stress along the lines as a function of the direction of the line. These equations as explained in more detail by Alexander & Brewer [28] are then used to calculate the stress at the tool face from the stress state at the free surface.

The velocity profile is drawn on the workpiece with the following assumptions and rules:

1. Shear lines are directions of maximum shear and deformation occurs in pure shear.
2. Elements along the slip lines may distort but do not elongate or shorten, therefore there is no change in velocity along a slip line due to elements stretching.

For plastic deformation to occur, there must be a velocity discontinuity between the velocity of the rigid material and the plastic material. The velocity discontinuity must be tangent to the maximum shear stress and is therefore a shear line.

Applying the shear line theory to the case of frictionless plane strain extrusion (R=3), one can see that the most convenient shear line field consists of two fans radiating from the die corner. The fans touch each other and the chamber walls, as shown in figure

3.7. Line OB in fig. 3.7 is a velocity discontinuity whereby material flows in this direction. Using fig 3.7, the stress in the dead zone, force on the die, force on the ram and the average ram pressure are all calculated.

Alexander and Brewer [28] perform the calculation for the situation of a frictionless extrusion, with an extrusion ratio of 3, a square die and no dead zone using the three methods. The shear line method shown in fig 3.8 shows the slip lines, streamlines and velocity discontinuities used in the analysis. From this graphical solution,

$$\text{Pressure against the die face} = 2k(1+\pi/2) \tag{3.8a}$$

$$\text{Force on the die face} = 2k(1+\pi/2)(H-h) \tag{3.8b}$$

$$\text{Force on the ram} = \text{the force on the die} \tag{3.8c}$$

$$\text{Average ram pressure} = 2k(1+\pi/2)(H-h)(1/H) \tag{3.8d}$$

$$p = 2k(2+\pi)/3 \tag{3.8e}$$

This results in $p/2k=1.71$ where p is the ram pressure, k is the flow stress, H is the original billet diameter and $h=H/3$. The value of $p/2k$ is used later to compare the results of the three methods.

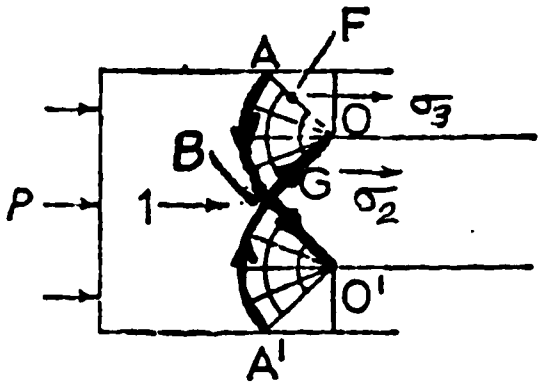

Figure 3.7: Shear line field for the case of frictionless plane strain extrusion [28]

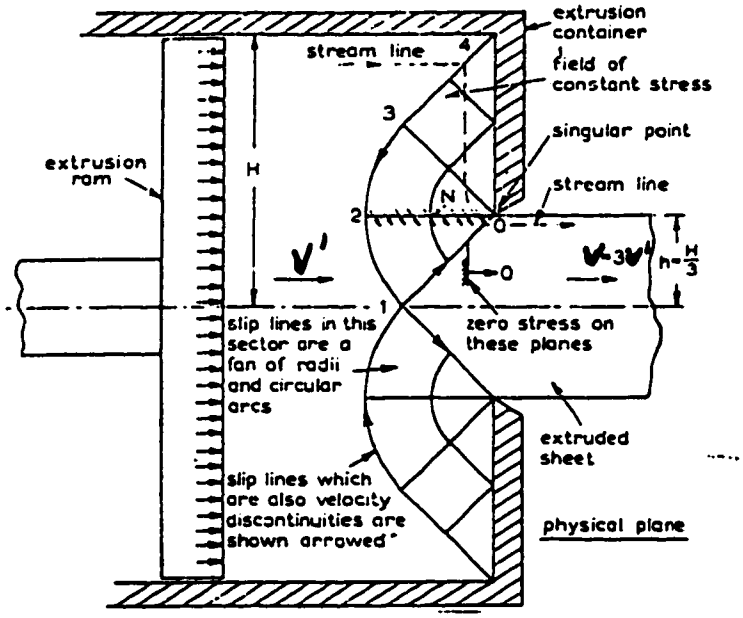

Figure 3.8: Slip lines, streamlines (45° to slip lines) and velocity discontinuities [28]

If the kinematically admissible velocity field solution (upper bound) is used to calculate ram pressure, the result is

$$\frac{p}{2k} = \frac{1+R}{\sqrt{R}} \tag{3.9}$$

where p/2k=2.31 when R=3 [28]. This is considerably higher than the result obtained using shear line solution as one would expect since the flow pattern is over simplified. Figure 3.9 shows the streamline used for this method and it is known that in reality, the metal will find an exit path that requires less work. The calculation can be refined by adding more lines of discontinuity in velocity which results in more gradual streamline as shown in fig.3.10 [41].

Lastly, using the statically admissible stress field solution (lower bound), the previous two solutions for average ram pressure can be compared. Fig 3.11 shows that regions A,B,C,E,F, are just at the yield stress, which are the regions where plastic deformation occurs. The average ram pressure is calculated by determining the contributions of each region to the total load. This results in

$$\frac{p}{2k} = 2.5 \cdot \left(1 - \frac{1}{R}\right) \tag{3.10}$$

where p/2k=1.667 when R=3. Therefore the real solution is predicted quite accurately between the shear line solution and the static stress solution. These solutions presented above can be refined by changing the boundary conditions to ones that are more realistic. For example, including a dead zone and friction between the billet and wall. It is not the objective in this thesis though to refine the shear line theory for extrusion calculations but rather to present the various methods of predicting ram load [28].

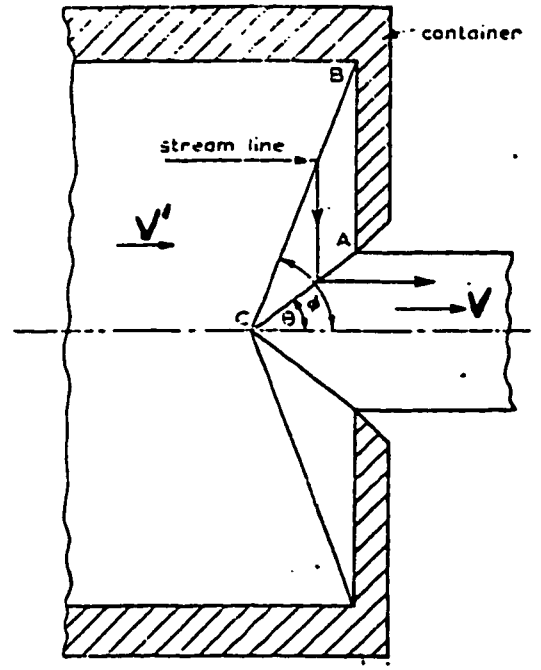

Figure 3.9: Kinematically admissible velocity field (upper bound solution), large reduction [28]

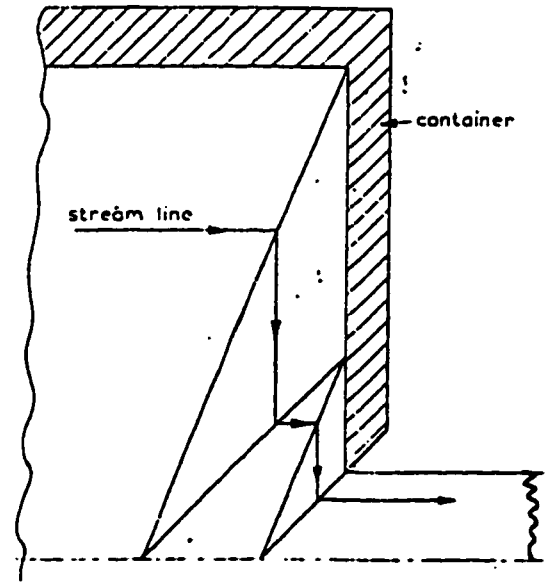

Figure 3.10: Kinematically admissible velocity field (upper bound solution), small reduction [28]

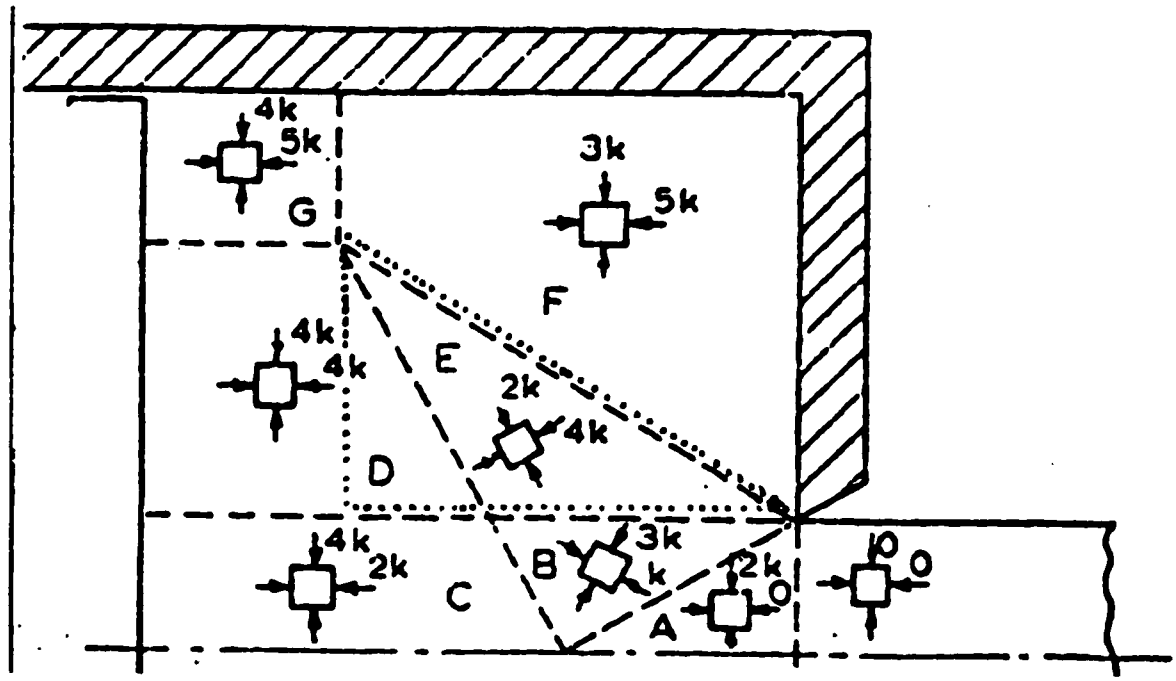

Figure 3.11: Statically admissible stress field (lower bound solution) [28]

3.4.3 Introduction to the Finite Element Method

The Finite Element Method (FEM) consists of the following basic steps:

- The object is first divided into distinct, non-overlapping regions called elements over which the main variables are interpolated.
- These elements are connected at a discrete number of points along their periphery known as nodal points.
- For each element the stiffness matrix and applied load vector are calculated.
- The stiffness matrix for each element are assembled to give the global stiffness matrix. The same is done for the load vector.
- The resulting system of simultaneous equations is solved for the unknown nodal variables.

Finally quantities such as stress components, temperature, etc. are evaluated for each element [42].

Extrusion modeling using the FEM, has been done in the past to a limited extent and some of this work will be discussed.

Behrens, Schafstall and Landgrebe [43] modeled a two stage cup drawing operation. The main objective of their work was to write a semi-automatic remeshing algorithm that could be integrated into an existing, commercially available FEM code called MARC. Most FEM codes remesh when the elements become severely distorted but there is the risk that the simulation will stop if the values cannot be interpolated from the previous mesh. Therefore they found it necessary to modify the FEM code so that remeshing would occur after a certain degree of mesh distortion is reached and this is done

repeatedly for high deformation rates. The algorithm was tested on a simulation of a cup drawing operation but was shown to be quite effective in extrusion modeling. The simulation of an Al-Mg-Si alloy extrusion was validated by experimental results [43].

Many researchers have modeled extrusion with the assumption that the metal flows as a fluid and used the analytical techniques used in fluid mechanics. Bhattacharyya et al. [44] modeled the plane strain and axisymmetric extrusion of lead using the commercial software PHOENICS. Simulations were run for a range of extrusion ratios. The extrusion was modeled in two ways; First assuming that the metal flows with constant viscosity and secondly assuming the viscosity changes from point to point depending on the strain rate at each point. It was found that the first assumption tended to grossly overpredict the extrusion pressure at high extrusion ratios. Much better results were obtained by treating the metal flow as a thixotropic fluid (varying viscosity) [44]. To validate the simulation results, experimental data was borrowed from Thomsen et al. [45].

Akeret [46] modelled the generation of heat in a billet being extruded by dividing the billet into thin disks, and treating the foremost disk as a heat source. A mathematical expression was obtained for the temperature rise in the foremost disk. This disk was then removed, the billet is moved forward and now the heating process occurs in the second disk. Akeret used this model to study the effects of varying the temperature of the tools relative to the billet temperature [46].

Two-Dimensional extrusion modeling of an Al-Mg-Si alloy was undertaken by Grasmo et al. [47] using a finite element (FE) program called ALMA-2D. The software is based on the Eulerian description whereby the mesh does not move with the material. The

other type of FE code is the Lagrangian description whereby the mesh is embedded in the material and moves with it. Software that uses the Lagrangian description will be discussed later. The ALMA 2-D program divides the billet, container, ram and die into triangular elements, placing a finer mesh in the regions of the billet where strain rate gradients are high. Heat generation caused by friction and deformation heating is coupled with a temperature dependent flow stress, thereby reducing the flow stress. Heat transfer between the billet and surrounding tools was taken into account but no direct heat transfer was considered between the tools. Friction conditions between the billet and the tools varied from "full stick" to "full slip." As the simulation is run, the aluminum mesh is linearly compressed, and at defined ram positions the billet is remeshed using the old mesh values. The material behaviour used in their model is based on a modified Zener-Hollomon relationship and the parameters are established by hot torsion testing [47].

Simulation results were compared to experimental work in the following ways:

- Compare peak load from simulation with measured value.
- Compare temperature of billet at the exit, die temperature and ram temperature.
- Compare simulated metal flow with experiments on a billet with embedded grid pattern.

Experimental work consisted of extruding billets of Al-Mg-Si alloy that had pins of Al-1.8% Cu inserted inside. The pins are inserted to provide information on the flow pattern at different steps in the extrusion. The billet is partially extruded, removed from the press, cut longitudinally then ground and etched whereby the flow pattern is revealed. This is repeated for several steps in an extrusion to show the progression of the flow pattern.

Figure 3.12 compares the flow pattern obtained experimentally with that obtained from the simulation and they are quite similar. During the extrusions, billet, die and ram temperatures were recorded which were used later to compare to simulation results [47].

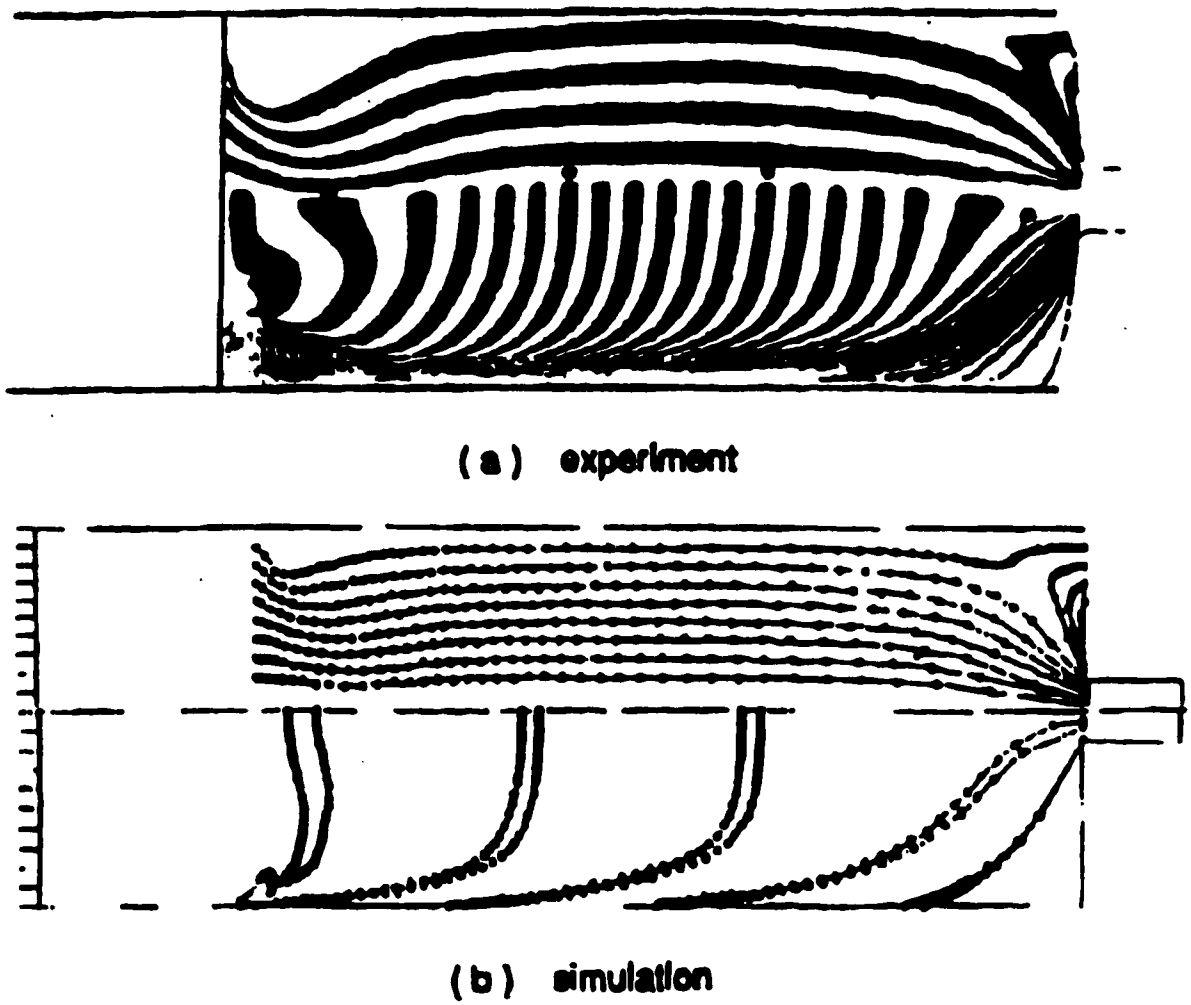

Figure 3.12: Flow pattern by Grasmo et al.: (a) experiment, (b) simulation [47]

It was found both experimentally and by calculation that die temperature remained constant and in some cases even decreased as the extrusion proceeded. The temperature gradients in the die were also found to be quite steep. Ram load was found to be strongly dependent upon billet temperature therefore any error in the temperature calculation leads to an error in the ram force. Deviation between experimental results and simulations were explained by simplified boundary conditions and assuming that the aluminum was isotropic [47].

Modeling of the extrusion of MMC's, namely 6061 Al reinforced with particles of Al_2O_3, was performed by Chen [32] at the University of British Columbia. The objectives of his work were to develop constitutive equations for the MMC's, to study the deformation behaviour of MMCs during extrusion by modeling the process, to compare the modeling results to real life extrusions, examine the microstructural evolution and finally to determine the deformation parameters that lead to low speed cracking [32].

In order to obtain a constitutive equation for each MMC, compression tests were performed on a "Gleeble" machine. The hyperbolic sine equation was used to predict the flow stress as a function of temperature and strain rate during hot working. Constitutive constants were obtained for the MMCs and the alloy by varying α (until the correlation coefficient, r was maximized).

The next step in their research was to run real-life extrusions. Billets were heated in a three zone furnace so that the billet end closest to the dummy block has the lowest temperature in the billet and it gradually increases towards the deformation zone. This is referred to as "taper heating." The dummy block was preheated to around 49 to 92 °C.

The die was preheated to about 427°C in a die box and was placed on the stack which was at ambient temperature. The container was heated to 427°C but there was considerable variation in temperature.

The extrusion press was a 3000T horizontal press with extrudate quenching capability. The extrusion speed was controlled manually and was varied to control surface quality. During the extrusion runs, the load, ram speed, and container temperatures were recorded.

Modeling of two plant trials was then performed using the finite element program, DEFORM. Velocity, stress, strain rate and temperature profiles were generated and the results are as follows:

- The velocity of the material at the die exit were significantly higher than those in the container due to the high extrusion ratio.
- A dead metal zone existed in the corner between the die and the container.
- The mean stress distribution in the billet showed mostly compressive stresses except tensile stresses existed at the die land due to the fact that material flows faster in the center zone and there is high friction stress at the die land. These tensile stresses can cause void formation.
- The maximum strain rate occurs at the die exit corner. (The die corner is defined from this point onwards as the inner edge of the die opening as shown by point "A" in figure 3.9)

- The temperature profiles showed an increase in billet temperature of approximately 70°C and the maximum temperature occured at the surface of the extrudate in the die land zone.
- The maximum die temperature was found to be approximately 10°C less than the maximum billet temperature due to thermal resistance at the die interface.
- The load versus stroke curve for the simulation had a similar peak value as for the plant trial but variations existed elsewhere in the two curves.

The plant trial data was used to validate the simulation predictions. The present work will also use these plant trials to validate the simulations. The effects of the extrusions parameters on the ram load will be discussed in later chapters as well as the comparison between present work, the UBC simulations and real life trials [32, 48].

Early work by McQueen, Charlton and the author focused on using constitutive equations obtained from hot torsion tests as material input for extrusion modeling. The commercial software, DEFORM was used to model the extrusions. The billet materials were the same as in the present work except different constitutive equations were used. Results showed that the constitutive equation must be very accurate in calculating flow stress in the 400 to 500°C extrusion temperature range otherwise the load versus stroke curves will cross-over as shown in figure 3.13. The cross-over was due to constitutive equations that were not accurate in the high temperature range. Figure 3.14 showed that the magnitude of flow stress is highest for the 20% and decreases with percent reinforcement at the low temperatures. In the high temperature zones, the curves cross over and the 15% then became softer than the 10% and even the alloy which was

incorrect. This problem triggered the present project which initially involved refining the constitutive equations for the 4 materials [49].

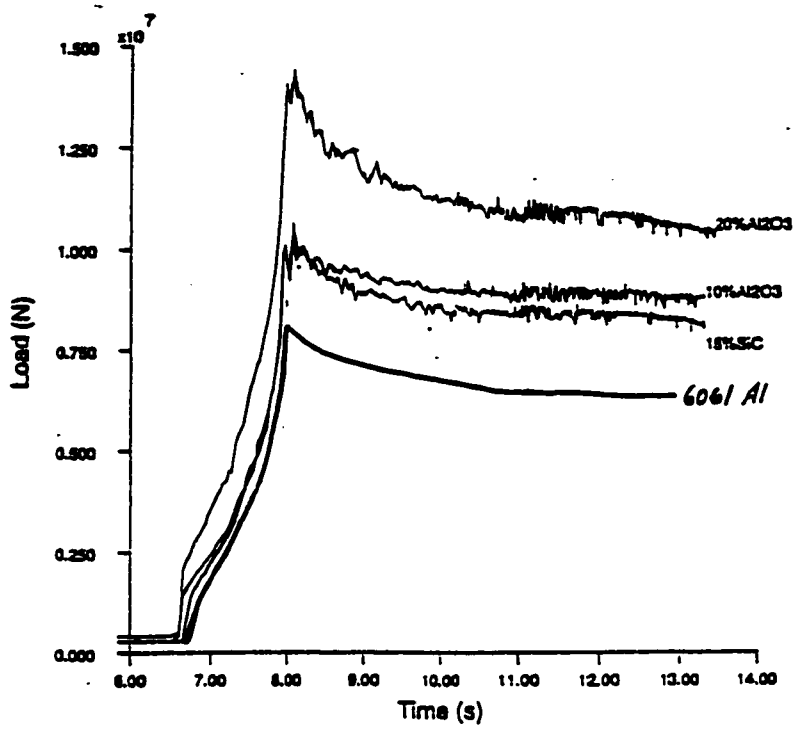

Figure 3.13: Load versus time for early DEFORM simulations

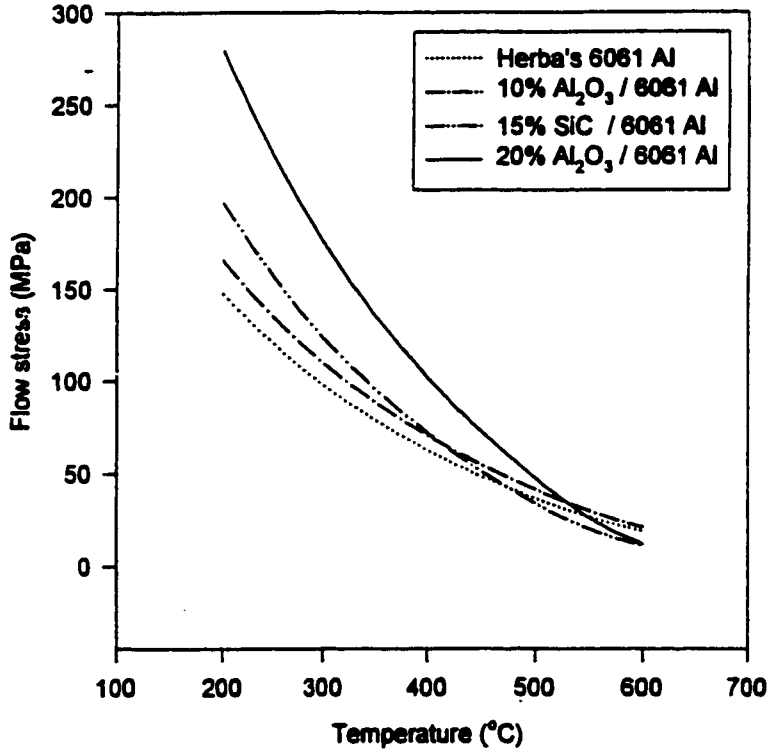

Figure 3.14: Flow stress versus temperature for original constitutive constants

4. EXPERIMENTAL AND MODELING PROCEDURE

4.1 Experimental Procedure

4.1.1 Hot Torsion Testing

Hot Torsion testing was used to obtain the flow stress data for the 6061 alloy and the MMC reinforced with Al_2O_3 or SiC. There are a number of reasons for choosing hot torsion testing over other methods such as compression or tension. The main advantages of torsion testing is that the geometry remains constant during deformation which is not the case in compression or tension testing. In tension, localized necking occurs and in compression, barreling occurs due to frictional forces at the ends of the specimen [50].

The torsion data is recorded in the form of torque versus angle of twist. Torque(Γ) must then be converted to shear stress (τ) by using the Fields Backofen equation:

$$\tau=\Gamma(3+m+n")/2\pi r^3 \qquad (4.1)$$

where Γ = Torsional moment

m = strain rate sensitivity

n"= strain hardening exponent

r = specimen gauge radius

The strain hardening exponent, n" is taken as zero for the steady state because the tests were conducted above 0.5 Tm. The strain rate sensitivity, m varies with temperature but has a minor influence on calculated stress because it is added to a larger value as is evident from the above equation. Equation 4.1 is used to obtain the surface shear stress from torque since torque integrates all the shear stresses. The shear stress varies as a function of radius since there is a strain rate gradient from center to surface.

The torsional strain on the surface (γ) of the specimen is calculated using:

$$\gamma = 2\pi r N / Lo \tag{4.2}$$

where N=Number of turns

Lo = Original gauge length

To compare flow stress data from torsion testing data obtained from either torsion or compression testing, the torsional shear stress and strains must be converted to effective stresses and strains. This is done using von Mises criterion for plastic yielding [50]:

$$\sigma = \sqrt{3}\,\tau \tag{4.3}$$

$$\varepsilon = \gamma / 3 \tag{4.4}$$

4.1.2 Testing Equipment

Specimens of 6061 Al were torsion tested by the author, whereas the MMC specimens were tested by Peter Sakaris and the results of his tests were discussed in several papers [2, 14, 51, 52, 53]. All the specimens were deformed in a computer directed, servo controlled, hydraulic torsion machine in the department of Mining and Metallurgy of McGill University. See figure 4.1. Torque is applied to the specimen via a hydraulic actuator mounted on a converted lathe bed. One end of the specimen is twisted while the other end is held fixed by a load cell.

Heating of the specimen was provided by a quadruple elliptical radiant furnace connected to a programmable controller. The furnace is water cooled and temperatures up to 1200°C can be attained. Argon is circulated through the furnace to prevent oxidation of the specimen. Specimen temperature is measured by a thermocouple which rests on the radius between the guage length and the shoulder of the specimen.

4.1.3 Computerized Testing System

The torsion machine was linked to an IBM-PC compatible 486/33mhz. Software called "Teststar" is used to control the test procedure, and for graphical output "Lotus 1-2-3" is used. The computer performs the following tasks in torsion testing:

- Accepts and interprets all test parameter information from the user.
- Use the input information to activate the required hardware devices which will in turn send the appropriate command signals to the closed loop system and drive the test.

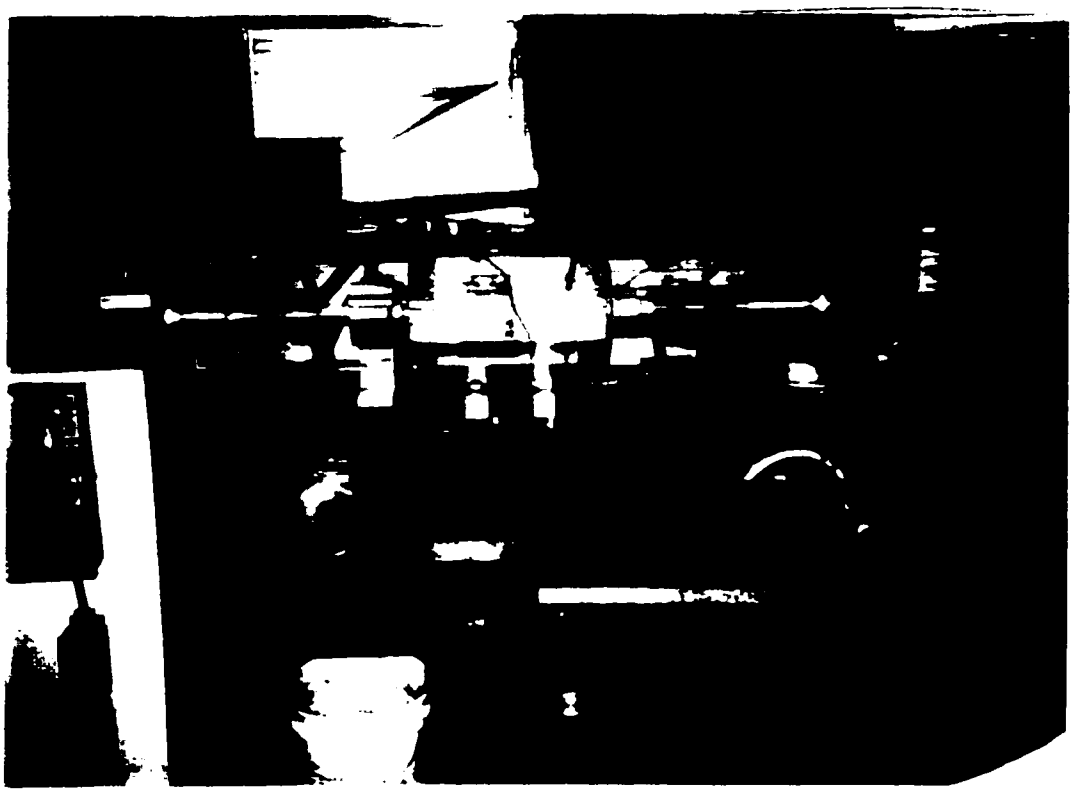

Figure 4.1: Torsion Machine: (a) photo

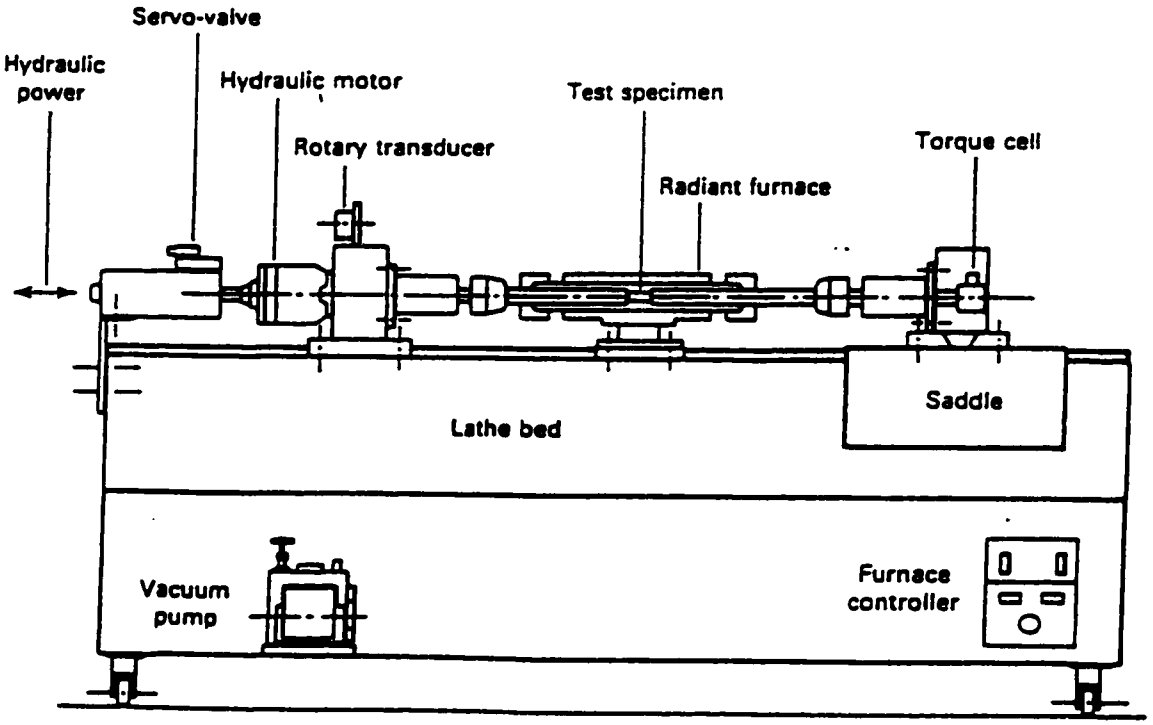

Figure 4.1: Torsion Machine (b) schematic [2]

- Monitor and record all output feedback information from the transducers within the closed loop system as the run is being executed.
- Interpret the transducer information and arrange it so it may be presented in a legible manner to the user.

4.1.4 Test Materials

As mentioned previously, torsion testing of the 6061 alloy was performed by the author and the MMCs were tested by Mr. Peter Sakaris. The MMCs tested were 10% Al_2O_3/6061 Al, 20% Al_2O_3/6061 Al, and 15% SiC/6061 Al. The composites were supplied by the Dural Aluminum Composite Corporation through Alcan Kingston Research and Development Center, Ontario, Canada. Compositions of all test materials is presented in table 4.1. Torsion specimens with axes parallel to the rolling or casting direction were machined to close tolerances, especially in the gauge section, to ensure that twisting would be uniform. The test pieces have a gauge length of 22.2 mm (0.875 in) and a diameter of 6.4 mm (0.25 in). All specimens tested were of the dimensions shown in figure 4.2.

Material	Composition wt%									
	Mg	Si	Cu	Fe	Cr	Zn	Ti	Mn	Al	reinforcement
6061 Al	0.97	0.71	0.28	0.58	0.24	0.045	0.016	0.04	rem	0
10%Al203/6061Al	1	0.6	0.3	0.7	0	0	0	0.15	rem	10% Al2O3
15%SiC/6061 Al	1	0.6	0.3	0.7	0	0	0	0.15	rem	15% SiC
20%Al2O3/6061Al	1	0.6	0.3	0.7	0	0	0	0.15	rem	20% Al2O3

Table 4.1 Chemical Compositions of 6061 Al and MMCs.

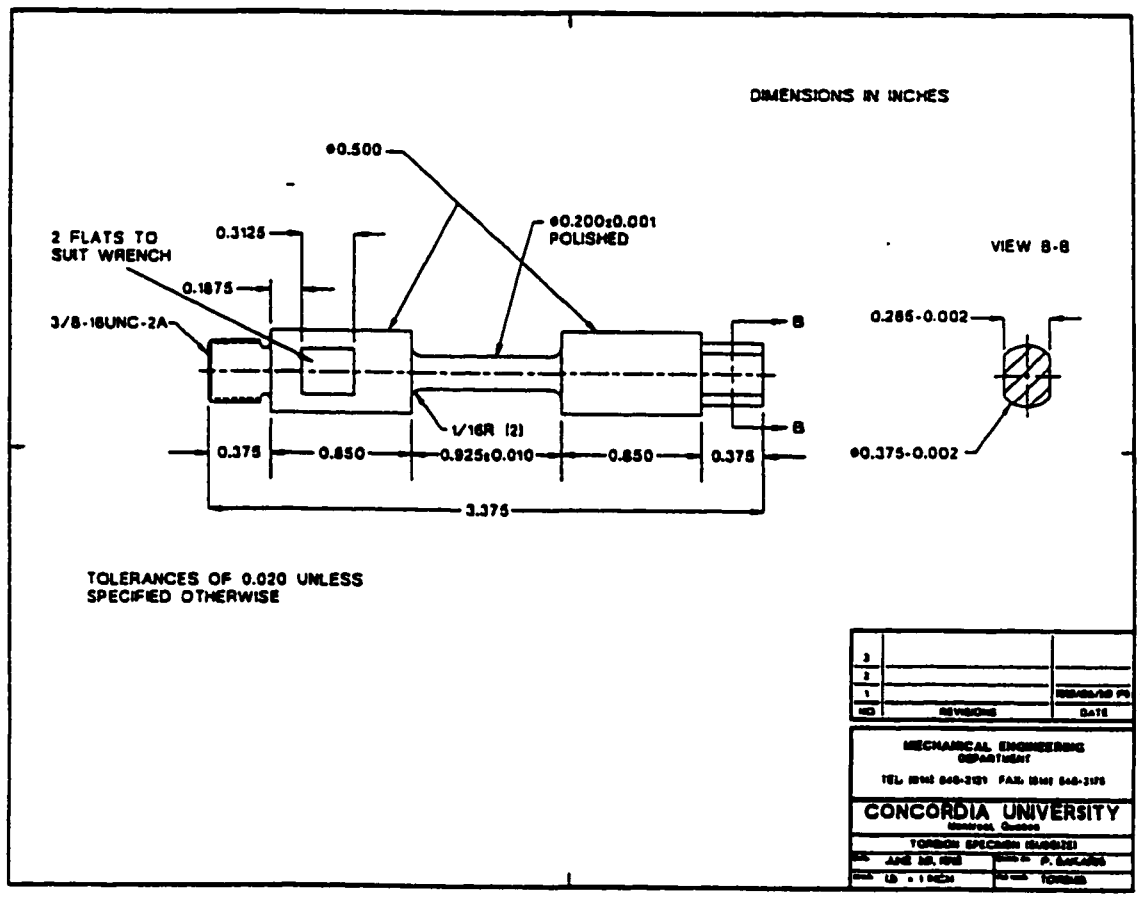

Figure 4.2: Torsion specimen design [2]

4.1.5 Test Procedures

Specimens were inserted into the grips of the machine after applying a high temperature anti-seize agent on the threads to ensure easy removal after the test is completed. One end of the specimen is screwed into the grip which is attached to a torque transducer, while the other end has a rectangular section which fits into a slot attached to the actuator. The setup is designed in this manner to allow for easy mounting and removal of the specimen without straining the specimen accidentally.

Each 6061 Al specimen was given a prior solution heat treatment which consisted of heating the specimen to the solutionizing temperature (529 °C), furnace cooling to the test temperature, and then quenching in air. Prior to deforming the specimen, the specimen was heated to the test temperature and allowed to equilibrate for 10 minutes. Isothermal, continuous tests were conducted for the 6061 alloy at 300, 400, 500 °C and strain rates of 0.01, 0.1, 1, 4 s^{-1}. In the case of the Duralcan® materials, tests were performed at strain rates between 0.1 and 5 s^{-1} and four temperatures between 300 and 540 °C. All tests were conducted in an atmosphere of high purity argon gas to prevent oxidation. After the deformation is completed, the specimens were quenched within 5 seconds.

4.2 Modeling Procedure

4.2.1 Finite Element Flow Formulation

The modeling of extrusion was carried out using the finite element package, DEFORM which is a registered trademark of Scientific Forming Technologies Corporation. DEFORM is based on a flow formulation approach using the penalty function procedure to guarantee volume constancy [54]. The Lagrangian method is used by DEFORM where the FE mesh moves with the deforming material as opposed to the Eulerian method where the mesh remains fixed. Large deformations such as ones encountered in extrusion can be modeled using DEFORM since it possesses an automatic mesh generator which generates a new mesh once the old mesh is too distorted [32].

In this study, the model consists of five objects making up the extrusion press; billet, die, container, pressure pad and stem as shown in figure 4.3. The dimensions of the extrusion press are consistent with the work of Chen at UBC [32] in order to be able to compare the simulation results. The billet has a diameter of 178 mm and a height of 305 mm. The billet was assumed to behave as a rigid-plastic material which is a reasonable assumption considering the billet undergoes large amounts of hot plastic deformation. All the tools were assumed to behave as completely rigid materials and any elastic deformation of the extrusion press was ignored. Along with deformation calculations, are heat transfer calculations which are interdependent. Heat transfer calculations are crucial since the billet and tools are heated to different temperatures, there is deformation heating, and frictional heating. The governing equation for heat transfer is:

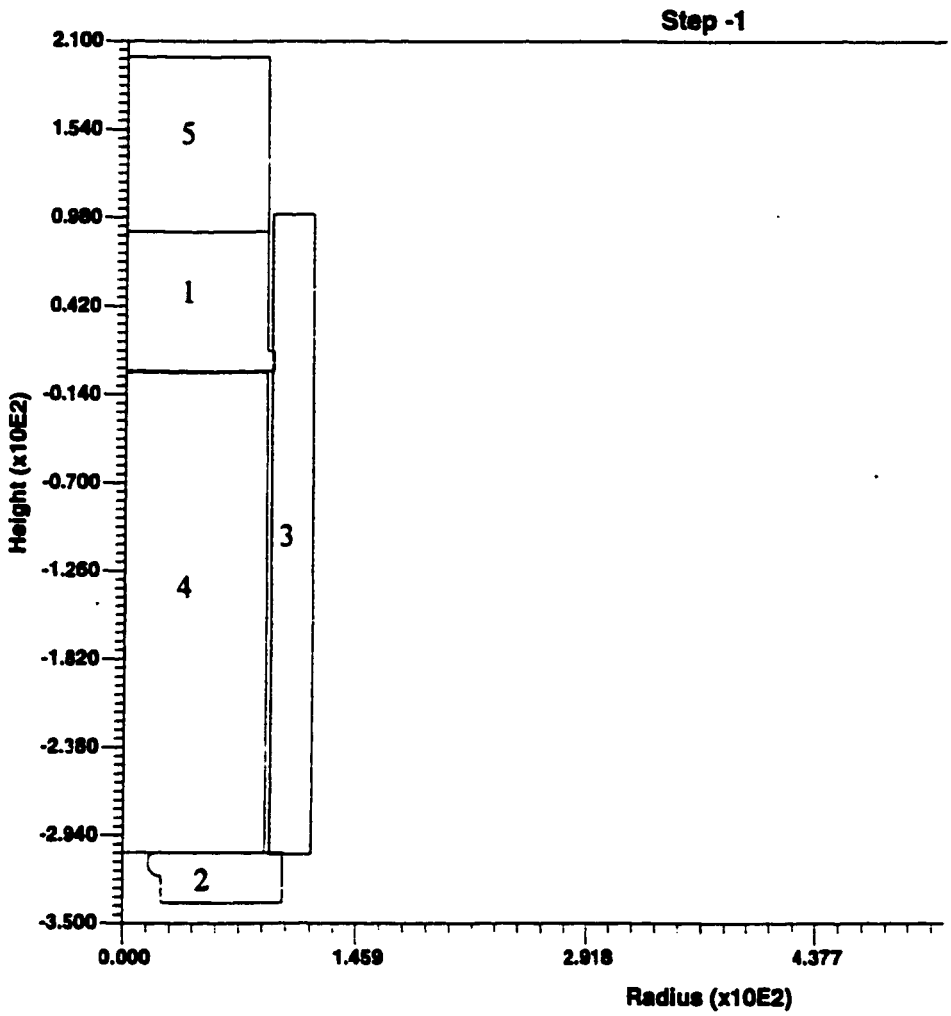

Figure 4.3: Model of extrusion press where object 1=dummy block, 2=die, 3=chamber, 4=billet, 5=stem.

$$kT_{i,i} + \dot{q} - \rho c p \dot{T} = 0 \tag{4.5}$$

where the first term of the equation is the heat transfer rate, with the comma denoting differentiation with respect to spatial coordinates and the repeated subscript meaning summation; k denotes thermal conductivity. The second term is the rate of heat generation due to deformation, which is obtained from the formula:

$$\dot{q} = \eta \bar{\sigma} \dot{\varepsilon} \tag{4.6}$$

where η is the efficiency of conversion of deformation energy to heat and is in the range of 0.9 to 0.95, depending on the material being formed. This heat generation term only applies to the billet since all other objects were assumed to be rigid. The third term in equation 4.5 is the rate of accumulation of internal energy. Eqn. 4.5 is then written in matrix form which DEFORM uses to relate heat transfer and deformation heating [32].

4.2.2 Boundary Conditions

The five objects were meshed with a series of four node iso-parametric elements as shown in figure 4.4. The billet was divided into 1000 elements, the dummy block (pressure pad) had 200 elements, container wall had 300 elements, the stem had 100 elements, and the die had 400 elements. The mesh was refined in regions where localized deformations were large and/or where large temperature gradients exist. Due to axisymmetry, an axisymmetrical section of the extrusion press was analyzed with a 2-D model. Heat transfer between the billet and surrounding tools was included in the analysis but interface heat transfer between the various tools was ignored. The billet was modeled with conduction and convection boundary conditions (BC) over the entire surface. When

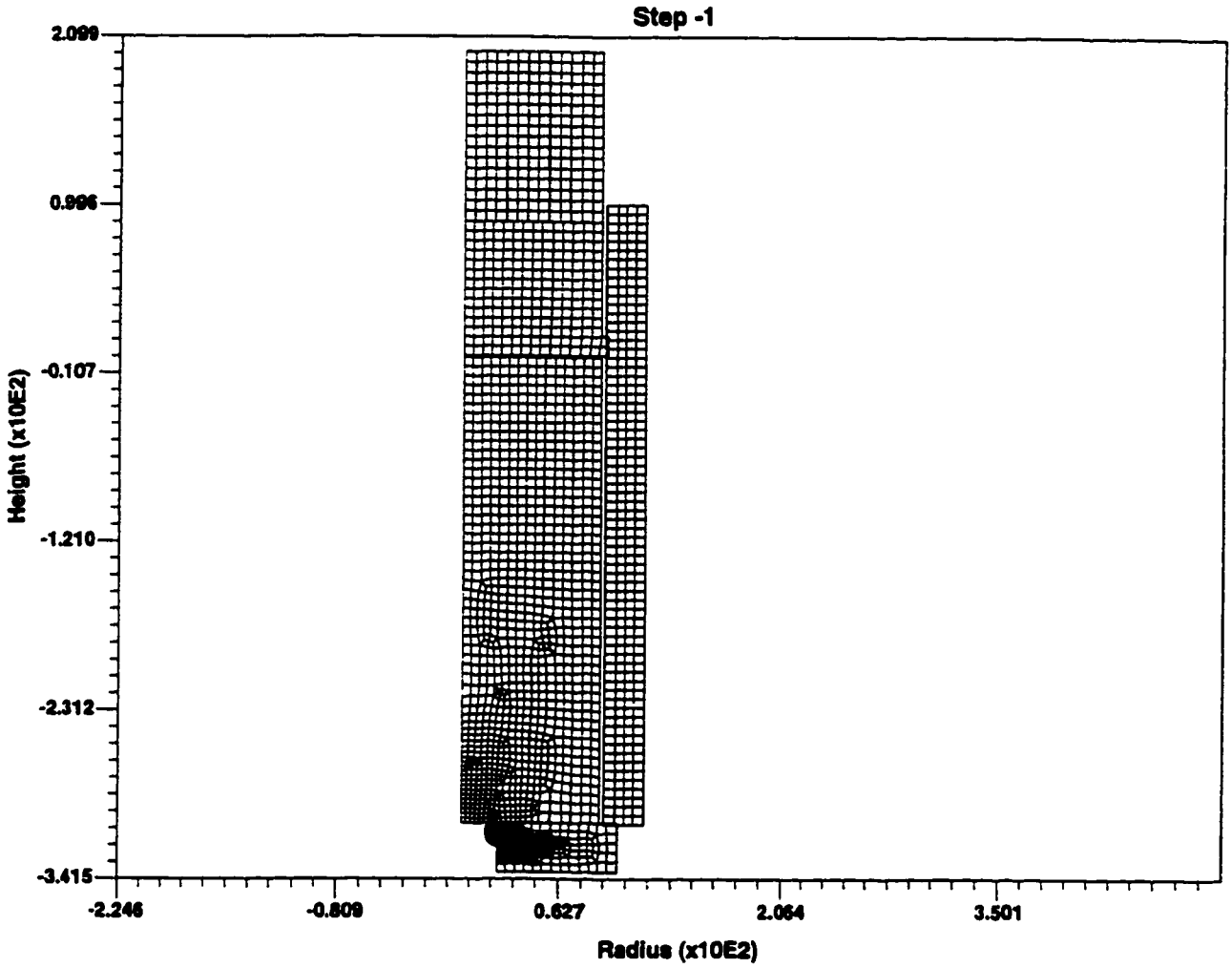

Figure 4.4: Initial finite element mesh for the billet and tools

a part of the billet is contacted by the tooling, the convection part of the heat transfer equation is set equal to zero by DEFORM and conduction is the main mode of heat transfer. The opposite occurs when the billet is surrounded by air and no longer is in contact with the tools; conduction heat transfer is set to zero and convection heat transfer is calculated. Similar heat transfer boundary conditions were imposed on the tools. The dummy block and stem had convection BC on the outer surfaces exposed to ambient air and conduction BC on the bottom surface of the dummy block once its contacts the billet. The die also had convection/conduction BC over its surface. The chamber wall had convection/conduction BC on the inside and the outside temperature of the container was held constant in order to simulate induction heating balancing heat lost to the environment. Based on the boundary conditions described above, the heat transfer equations are as follows;

At interface boundary between billet and tools: $kT_{B,i} = h(T_{BS}-T_{TS})$ (4.7)

At surface boundary exposed to air: $kT_{B,i} = h_{air}(T_{BS}-T_{\infty})$ (4.8)

At centerline of billet (heat transfer is zero): $kT_{B,i} = 0$ (4.9)

At outer surface of container (induction heater) $T_{cs}=T_o$ (4.10)

where T_{BS} and T_{TS} are interface temperatures of the billet and its contacted tool, respectively; h is the interface heat transfer coefficient; h_{air} is the convection heat transfer coefficient, $T_{B,i}$ is the billet temperature at point i; T_{cs} is the container temperature and T_o is the outer surface temperature of the container which is heated by an induction heater.

Mechanical boundary conditions on the deforming billet were also specified. At the centerline of the billet, velocity in the radial direction was set to zero. In addition, friction stress was applied between the billet and the surrounding tools. The shear factor friction law, $\tau = mk$, was adopted in hot deformation, where τ is the friction stress, m is the shear factor and k the shear strength of the billet [32]. The free surfaces of the billet such as the extrudate have no friction conditions applied.

4.2.3 Input Data

The hyperbolic sine constitutive equations obtained from torsion testing were employed in DEFORM to calculate the flow stress as a function of temperature and strain rate. The thermophysical properties of the billet and the tools were assumed to be independent of temperature since the values varied only slightly in the range of temperatures encountered in the simulation. These values are presented in table 4.2.

	6061 Al	H13 Tool Steel
Thermal Conductivity (N/sec °C)	180	28.4
Heat Capacity (N/mm^2 °C)	2.94	2.51
Emmisivity	0.19	0.7

Table 4.2 Thermal Properties data

The thermal conductivity values were obtained from the Metals Handbook [29], heat capacity and emmisivity values were obtained from other handbooks [1, 55]. Thermal property data was assumed to be the same for the MMC as the 6061 alloy. The heat transfer coefficient at the interface between the billet and the tools was calculated based on Akaret's work [46] dealing with predicting the temperature distribution in an extrusion process and was found to be 0.2 N/sec mm °K. Friction at the interface of the billet and the surrounding tools was assumed to be complete sticking friction with m=1 in the shear friction law equation. Chen [32] assumed m=1 between the container and billet and also between billet and die but m was set equal to 0.7 at the pressure pad / billet interface.

Although the boundary conditions and material constants remained unchanged for all simulations, the initial conditions were varied for each simulation. Initial billet temperature, ram speed, and extrusion ratio were varied. Initial billet temperatures used were 450, 475, and 500°C, ram speed was either 2.6 or 5 mm/s, and two extrusion ratios were used; 31 and 64. The results of varying these initial conditions will be presented in the next section. The initial temperatures of the tools were not changed and are as follows; die temperature was set to 425°C, dummy block temperature was set to 175°C, stem temperature was set to 100°C and the container wall temperature was set 20 to 30 °C below the billet temperature.

5. RESULTS

5.1 Data Analysis

5.1.1 Torsion Testing Results

The torque versus twist data obtained from the torsion tests were converted to stress versus strain using equations 4.1 through 4.4 in order to compare the results to the findings of other researchers. The value of m was obtained from the slope of the log torque versus log strain rate. and the values vary from about 0.01 at 300 °C to 0.17 near the melting temperature for all four materials. The values of n" were taken as zero which is valid only for the peak stress values. The continuous stress-strain curves for strain rates of 0.01, 0.1, 1, and $4s^{-1}$ at various temperatures for the 6061 alloy are presented in figures 5.1. The flow curves for the MMCs are presented in figures 5.2 for strain rates ranging from 0.1 to 5 s^{-1}.

Figures 5.1 and 5.2 show the rising flow stress that occurs with an increase in strain rate and a decrease in temperature. The flow stresses of the MMCs are significantly higher than the alloy at low temperatures but the difference diminishes as temperature increases. Increasing the volume fraction of reinforcement has the effect of increasing the flow stress, especially at low deformation temperatures.

The flow stresses decrease rapidly with increasing deformation temperature at the low temperatures whereas at the high temperatures the rate of decrease is lower as show in figure 5.3. The difference between flow stresses at the low temperatures is greater than at the high temperatures where all four materials seem to have similar flow stresses. The

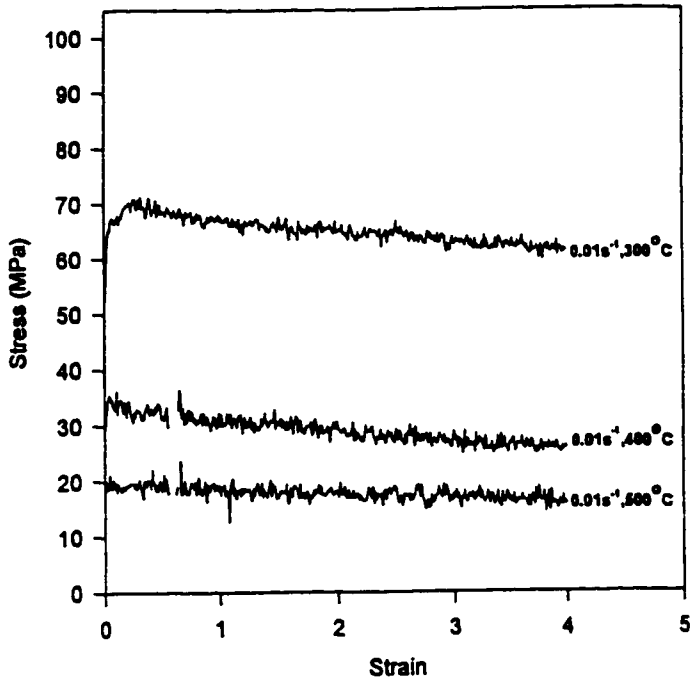

(a)

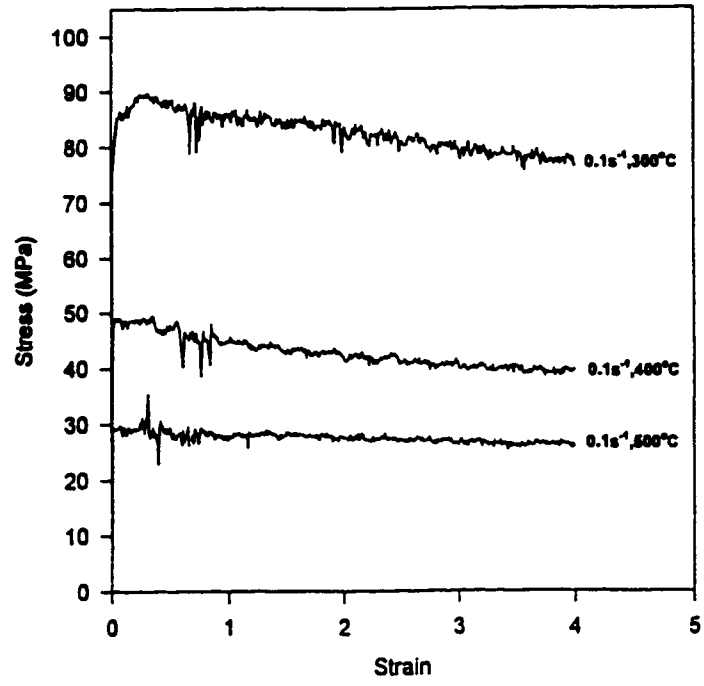

(b)

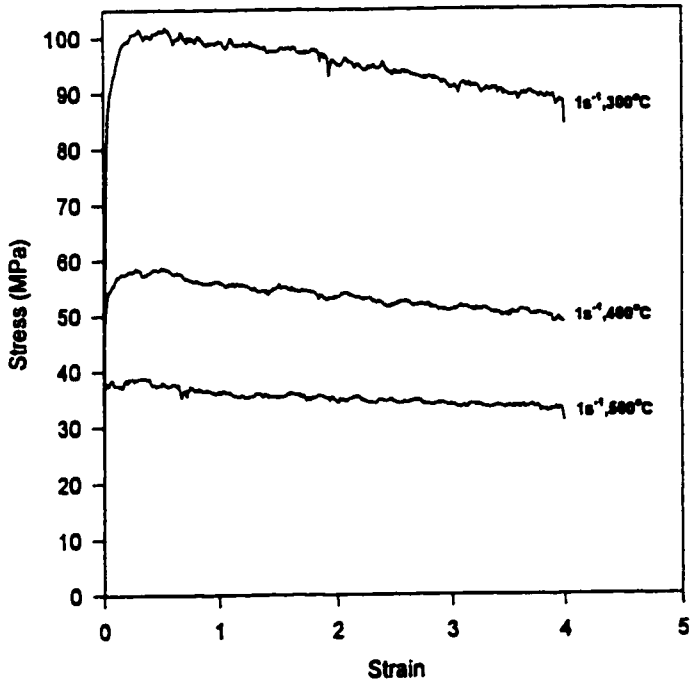

(c)

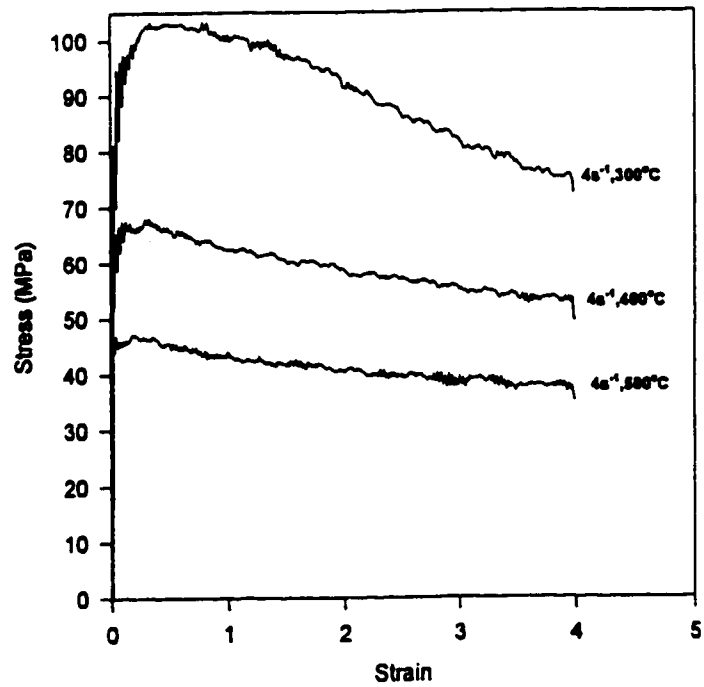

(d)

Figure 5.1: Flow curves for 6061 Al alloy at: (a) $0.01s^{-1}$, (b) $0.1\ s^{-1}$, (c) $1\ s^{-1}$, (d) $4\ s^{-1}$

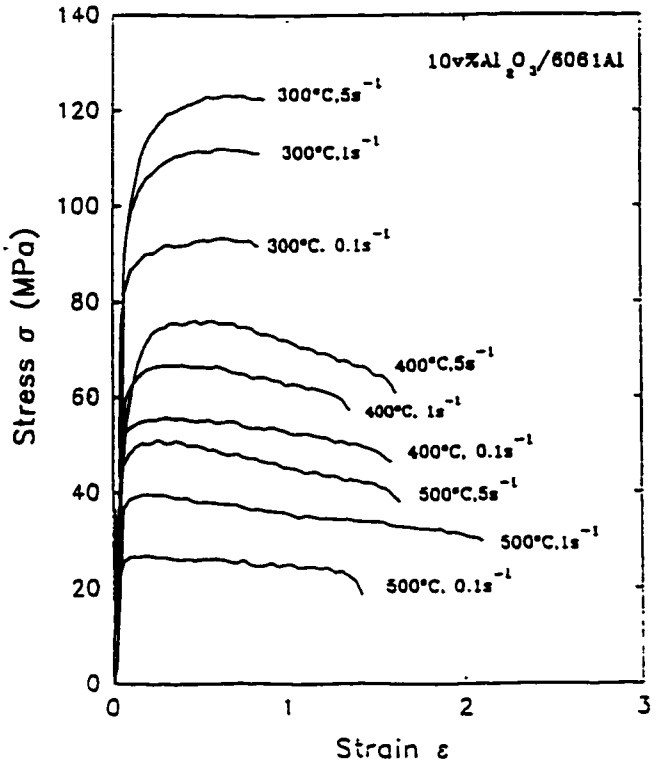

(a)

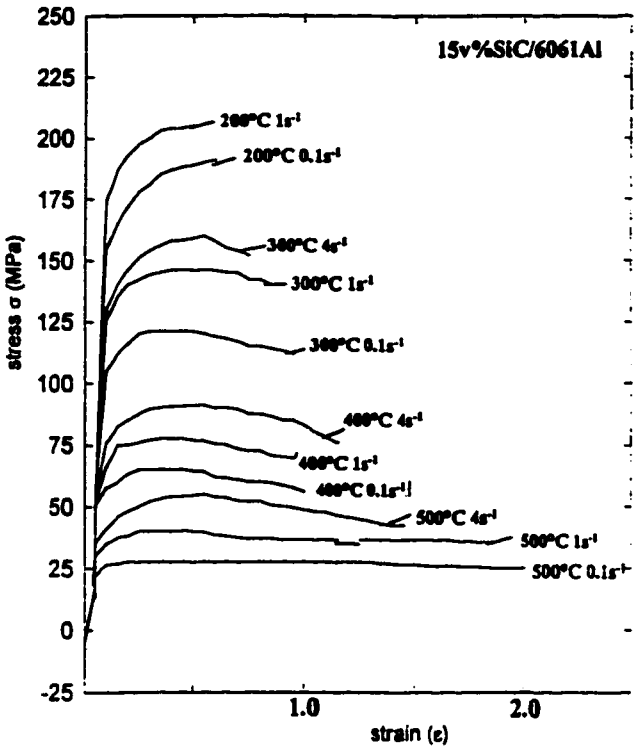

(b)

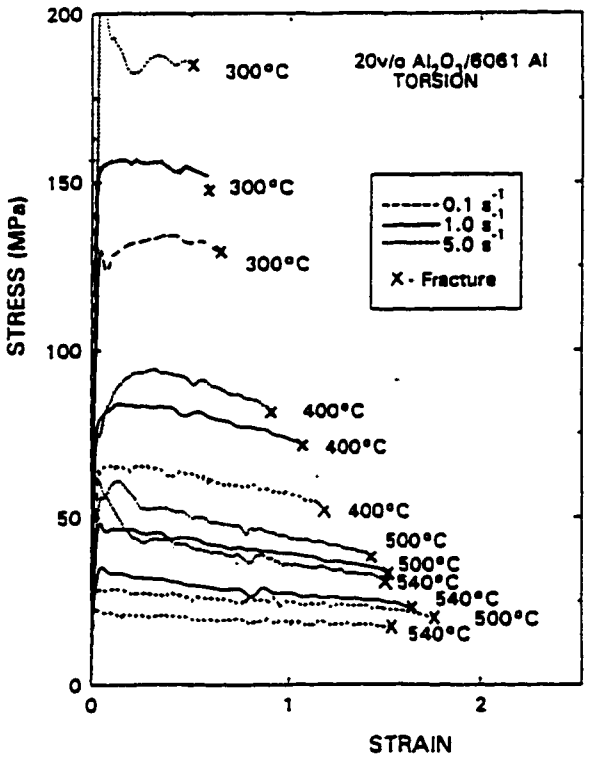

(c)

Figure 5.2: Flow curves for the 6061 MMC: (a) 10%Al_2O_3/6061, (b) 15% SiC/6061, (c) 20%Al_2O_3/6061

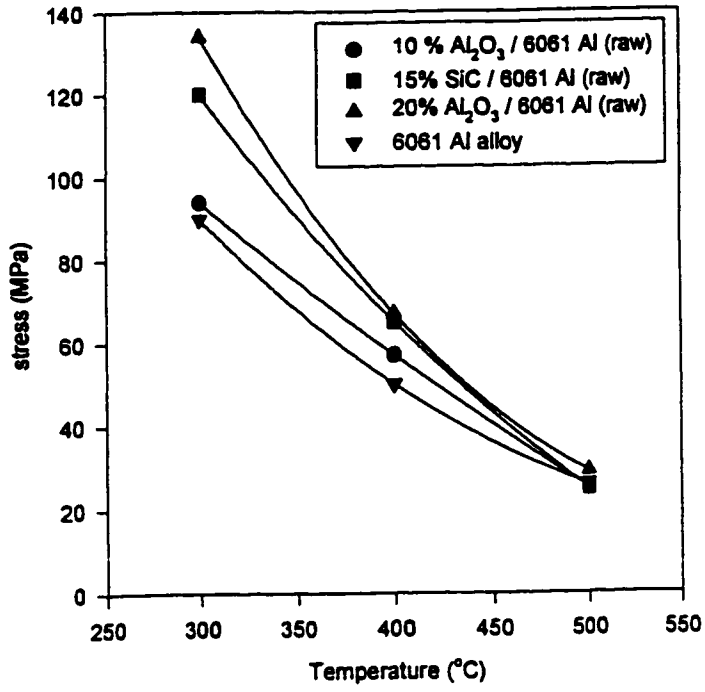

(a)

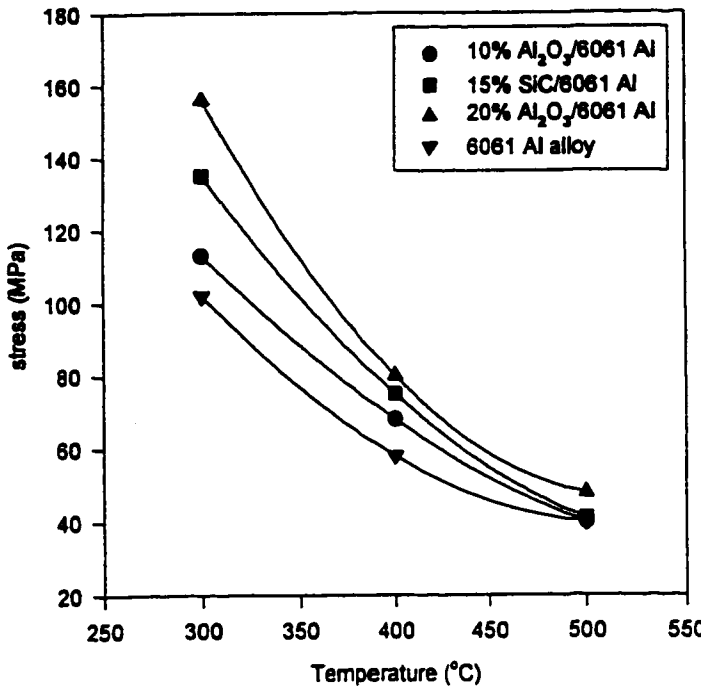

(b)

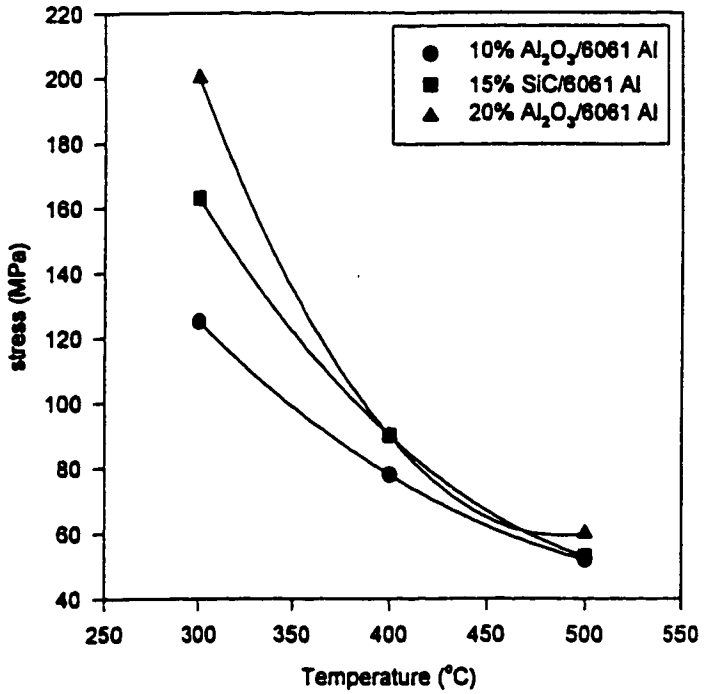

(c)

Figure 5.3: Stress versus temperature for the original raw data: (a) $0.1s^{-1}$, (b) $1s^{-1}$, (c) $5s^{-1}$

composites are clearly much stronger than the matrix alloy at lower temperatures but only slightly so at higher ones. The rate of decline increases with increasing strain rates because of starting from higher stress levels.

5.1.2 Validation of 6061 Torsion Test Data

The results obtained from torsion experiments for the 6061 Al alloy were validated by comparing the results to other researchers' findings. It must be noted that 6061 Al has a range of possible compositions and varying the amounts of Mg, Si or Fe can have a significant effect on the hot working properties of the alloy. Each researcher tested the 6061 grade but slightly different flow stress values were obtained for a given temperature and strain rate. Upon closer examination, it was found that the composition of each researcher's alloy was unique as listed in table 5.1. The present 6061 was compared to work by Pickens et al.[56], Zhao et al.[57], Chen [32], and Davies et al.[58] and is illustrated in figure 5.4. Figure 5.4 shows the amount of possible scatter in flow stress values which is larger at the higher strain rates and smaller at the low strain rates. The present 6061 has the lowest flow stress at 400°C for the three strain rates of 0.1, 1, 4 s^{-1} and vice versa at 500°C. A possible explanation could be related to the fact that the present 6061 has the largest quantity of Si and Fe, which combine to form Fe-Al-Si particles. When Fe combines with Si, less Si is available to combine with Mg producing less Mg_2Si particles which are responsible for strengthening. The variations in flow stress for a particular condition can be explained by differences in composition and also variations in testing techniques. For example the results of Zhao et al. [57] were obtained

from hot compression tests rather than from hot torsion tests which would explain differences in results. Friction affects the results of compression testing whereas it does not play a role in torsion testing. There is also the effect of prior heat treatment which could explain the disparity in results.

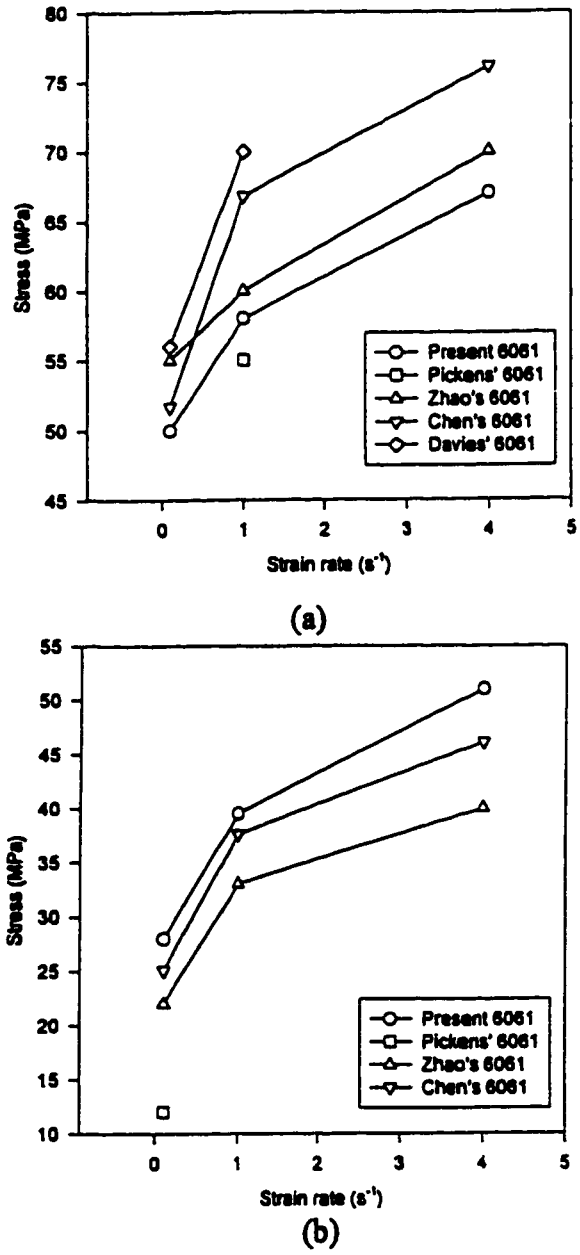

Figure 5.4: Validation of present 6061 Al experimental data: (a) 400°C, (b) 500°C, [32, 56, 57, 58]

Material	Composition (wt %)								
	Mg	Si	Cu	Fe	Cr	Zn	Ti	Mn	Co
Present 6061	0.97	0.71	0.28	0.58	0.24	0.045	0.016	0.04	
Pickens' 6061	1.07	0.57	0.27	0.04	0.0078	0.033	0.0022	0.0018	0.0005
Zhao's 6061	1	0.6	0.28	0.7	0.195	0.25	0.15	0.15	
UBC's 6061	0.91	0.57	0.24	0.26	0.086	0.048	0.015	0.032	
6061 matrix	1	0.6	0.3	0.7				0.15	

Table 5.1: 6061 compositions [32, 56, 57, 58]

5.1.3 Constitutive Plots

The effect of temperature and strain rate on flow stress was analyzed and equation 3.3 expresses this relationship satisfactorily. In order to compare constitutive constants for each material and to previous work, the stress multiplier α was kept at 0.052 MPa^{-1}. Log strain rate versus log sinh ($\alpha\sigma$) was plotted for each material in order to obtain the value of average n which was found from the slopes of the constant temperature lines. Log sinh ($\alpha\sigma$) versus 1/T was plotted and the slopes of the constant strain rate lines yielded the value of average s. Activation energy could now be calculated using the following equation which is derived from equation 3.3:

$$Q_{HW} = 2.3\ nRs \qquad (5.1)$$

First order regressions were performed on the constant temperature lines and the constant strain rate lines to determine the values of n and s respectively. The plots of log strain rate

versus log sinh ($\alpha\sigma$) and log sinh ($\alpha\sigma$) versus 1/T for the four materials are presented in figure 5.5 and 5.6

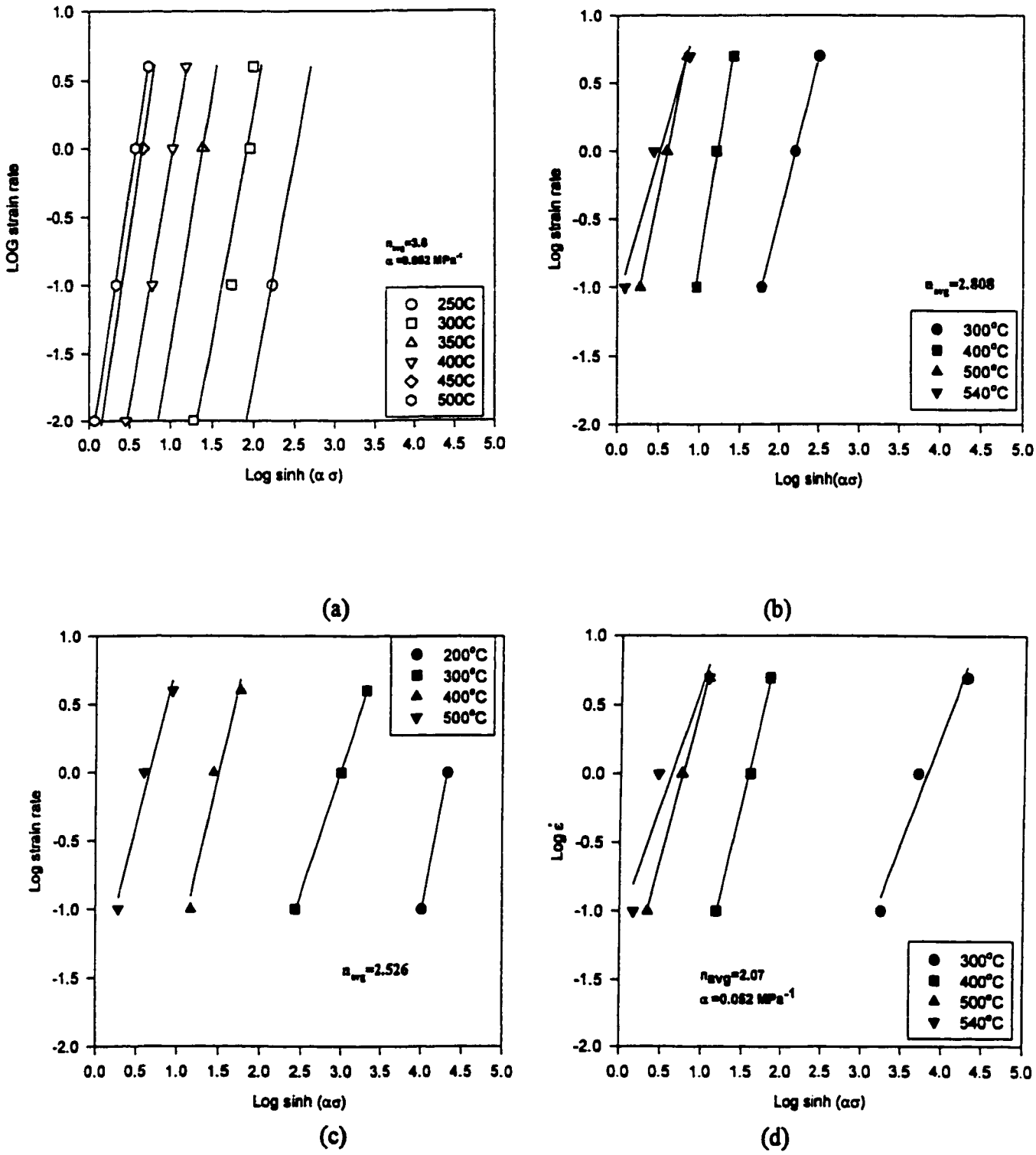

Figure 5.5: Log strain rate versus Log sinh ($\alpha\sigma$) with α=0.052 Mpa^{-1}: (a) 6061 Al, (b) 10% Al_2O_3/6061, (c) 15%SiC/6061, (d) 20% Al_2O_3/6061

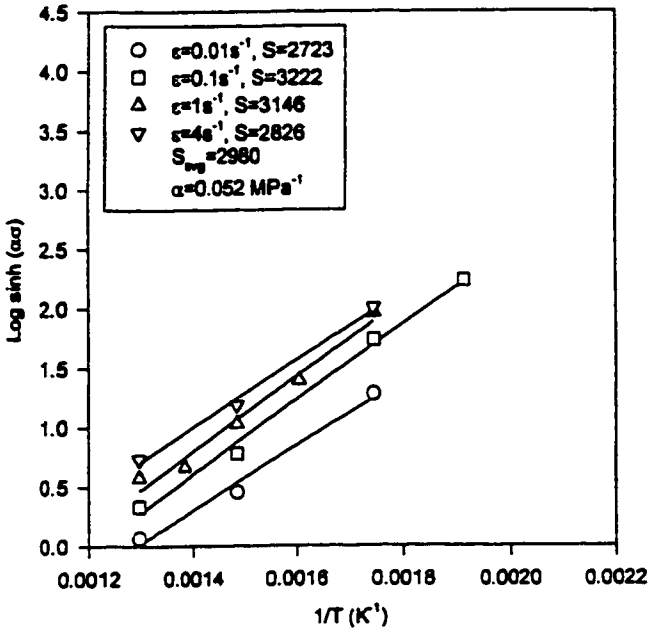

(a)

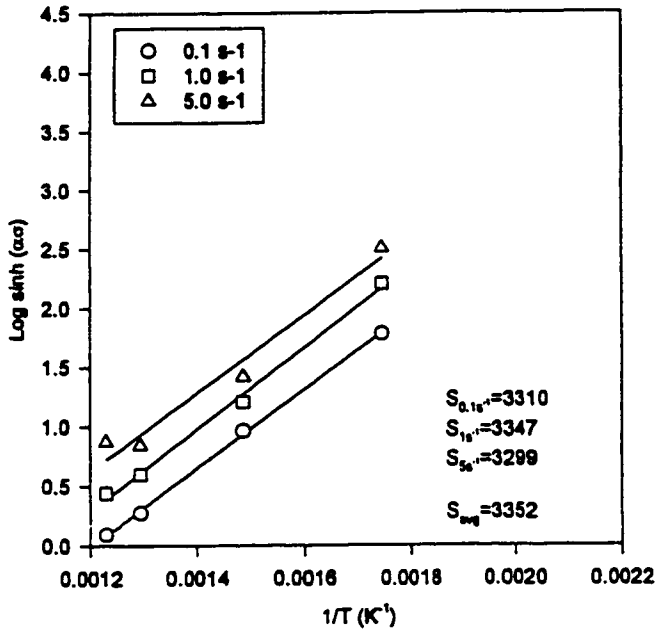

(b)

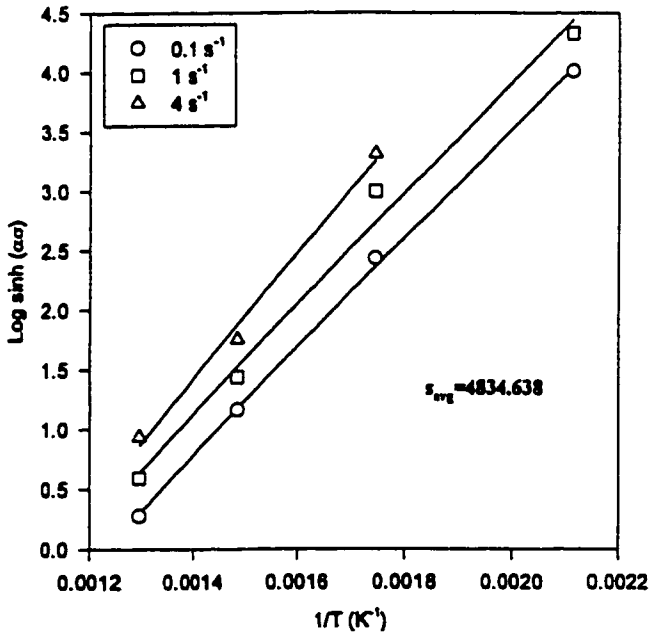

(c)

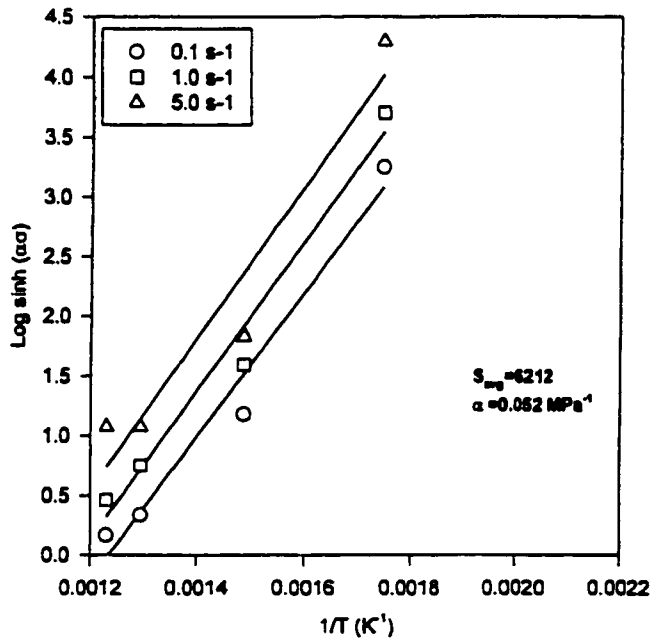

(d)

Figure 5.6: Log sinh ($\alpha\sigma$) vs 1/T with α=0.052 Mpa^{-1} for: (a) 6061 alloy, (b) 10% Al_2O_3/6061, (c) 15%SiC/6061, (d) 20% Al_2O_3/6061

respectively. With Q_{Hw} determined for the four materials, it is possible to check the accuracy of the constitutive equation by plotting all the points on graphs of log Z versus log sinh ($\alpha\sigma$) as shown in figure 5.7. This plot yields the remaining constants in the constitutive equation; A is the y intercept and n_z is the average n. The closeness of the points to the straight line on the log Z plot are representative of the quality of the fit.

Constitutive constants for the MMC were determined in earlier work by McQueen and Sakaris and these constants are presented in Table 5.2. It was found by calculating flow stress using the constitutive equation and plotting stress versus temperature for the four materials, that the equation for the 15% SiC / 6061 Al material did not fit accurately enough to be used for modeling purposes. Figure 5.8a shows that the curve for 15% SiC / 6061 is lower than the 10% Al_2O_3 / 6061 at 420°C and lower than the alloy at temperatures above 480°C. From figure 5.3 b, it is clear that the 15% SiC material should have a higher flow stress than the 10% Al_2O_3 and the alloy at all temperatures. It was therefore necessary to recalculate the constitutive constants for the 15% SiC material to obtain a more accurate equation. The constitutive analysis was repeated for the 15% SiC /6061 but including the flow stress values obtained from torsion tests performed at 200°C which were neglected in the original analysis. The results of this new constitutive analysis yielded improved results as illustrated in figure 5.8b. Table 5.3 lists the new constitutive constants. The constitutive equation obtained by Chen et al. at UBC [32] for their 6061 was added to the present results for comparison purposes. It is evident that the present constitutive equation for the 6061 Al yields similar results to Chen's [32, 59].

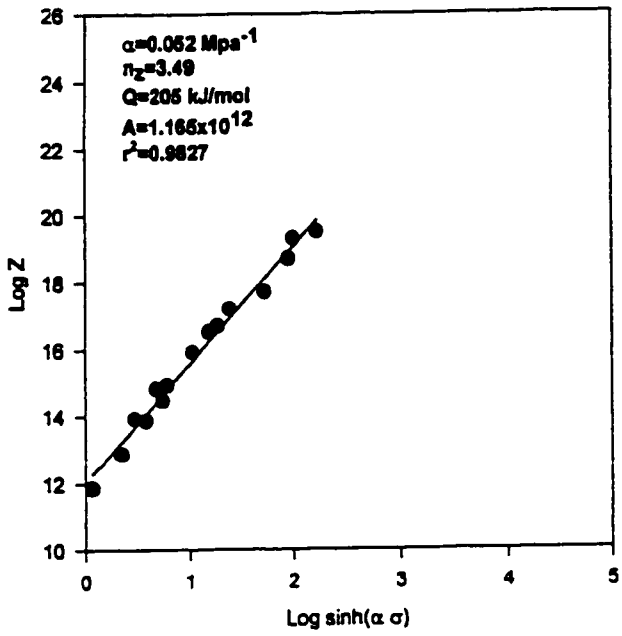

(a)

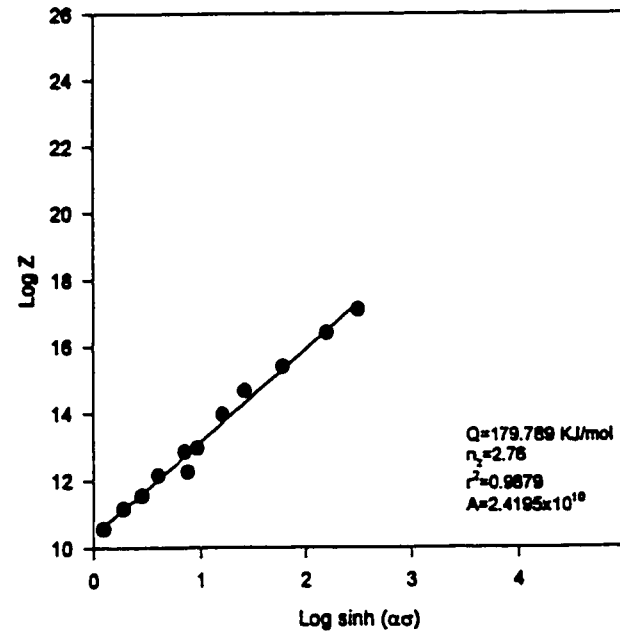

(b)

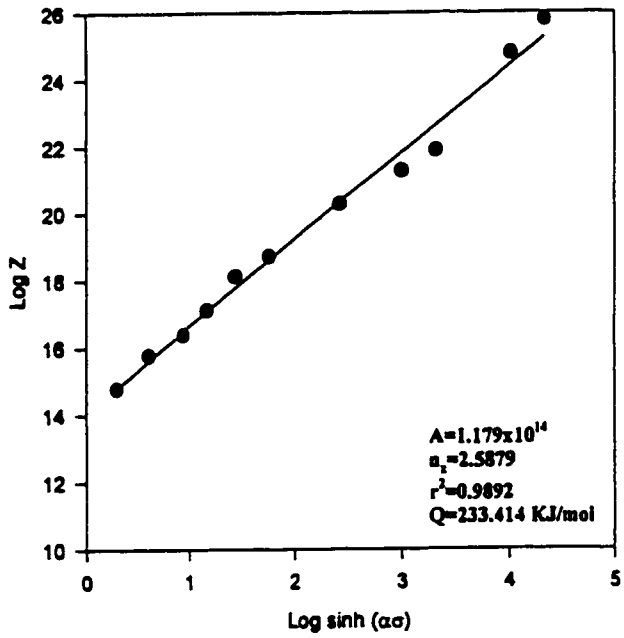

(c)

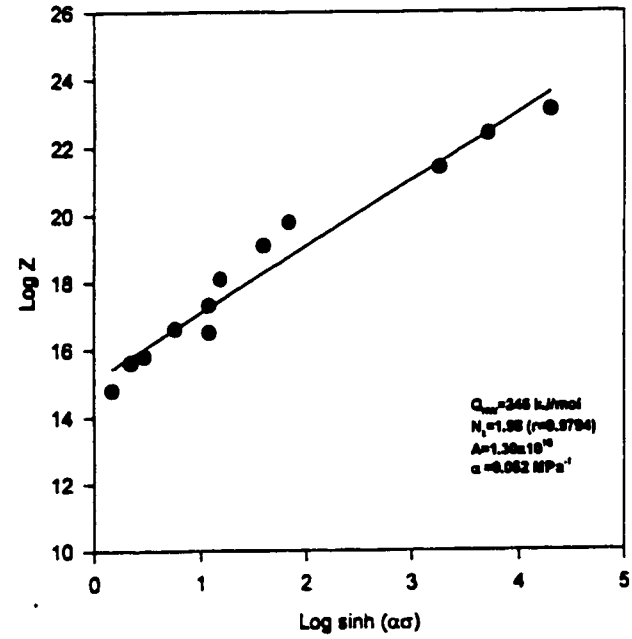

(d)

Figure 5.7: Log Z versus Log sinh (ασ) with α=0.052 Mpa^{-1} for: (a) 6061 alloy, (b) 10% Al_2O_3/6061, (c) 15%SiC/6061, (d) 20% Al_2O_3/6061

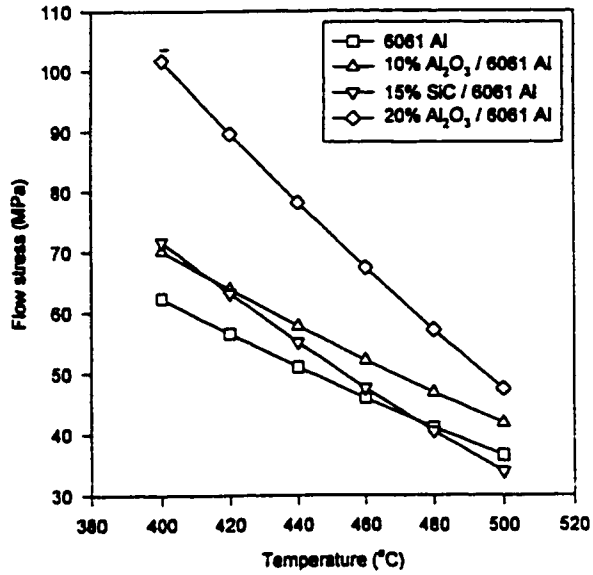

(a)

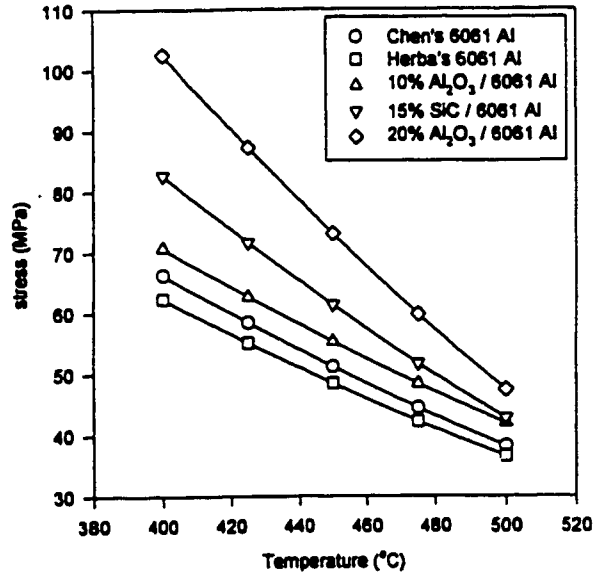

(b)

Figure 5.8: Stress versus temperature calculated from constitutive constants at $1s^{-1}$: (a) Original constitutive constants and (b) New constitutive constants

Material	Q(KJ/mol K)	A (s-1)	stress exp.(MPa-1)	n	r
6061	205	1.17E+12	0.052	3.49	0.9827
10%Al2O3/6061	180	2.42E+10	0.052	2.8	n/a
15%SiC/6061	233	3.40E+14	0.052	2.7	n/a
20%Al2O3/6061	247	1.40E+15	0.052	2.02	n/a

Table 5.2: McQueen and Sakaris' original constitutive constants

Material	Q(KJ/mol K)	A (s-1)	stress exp.(MPa-1)	n	r
6061	205	1.17E+12	0.052	3.49	0.9827
10%Al2O3/6061	179.789	2.42E+10	0.052	2.76	0.9879
15%SiC/6061	233.414	1.18E+14	0.052	2.588	0.9892
20%Al2O3/6061	246	1.30E+15	0.052	1.98	0.9794

Table 5.3: McQueen and Herba's new constitutive constants

5.2 Results of Extrusion Modeling

The extrusion of 6061 aluminum and the MMC was simulated for different processing conditions. The influence of these processing conditions on ram load, material flow, maximum billet temperature, maximum velocity of extrudate, strain rate and mean stress will be presented in this chapter and discussed in the next. A summary of the simulation results is presented in table 5.4.

5.2.1 Load Stroke Curves

Once a simulation is completed, the results can be viewed using the DEFORM Post-Processor. A plot of ram load as a function of time is one of the simulation outputs that can be viewed and figure 5.9 shows a typical such curve. The curve can be divide into three distinct parts as describe in chapter 3;

- The ram moves down until it contacts the billet (flat initial part of curve).
- The billet is upset and fills the container (steep rise in curve up to a peak).
- The billet begins to extrude starting at the peak and the load decreases as temperature rises due to deformation heating.

The curve shown in figure 5.9 is the result of a simulation run with a billet of 20%Al_2O_3/6061, a ram speed of 2.6 mm/s, an extrusion ratio of 31, and an initial billet temperature of 500°C. The effects of varying these parameters on the load stroke curves will be presented later in this chapter.

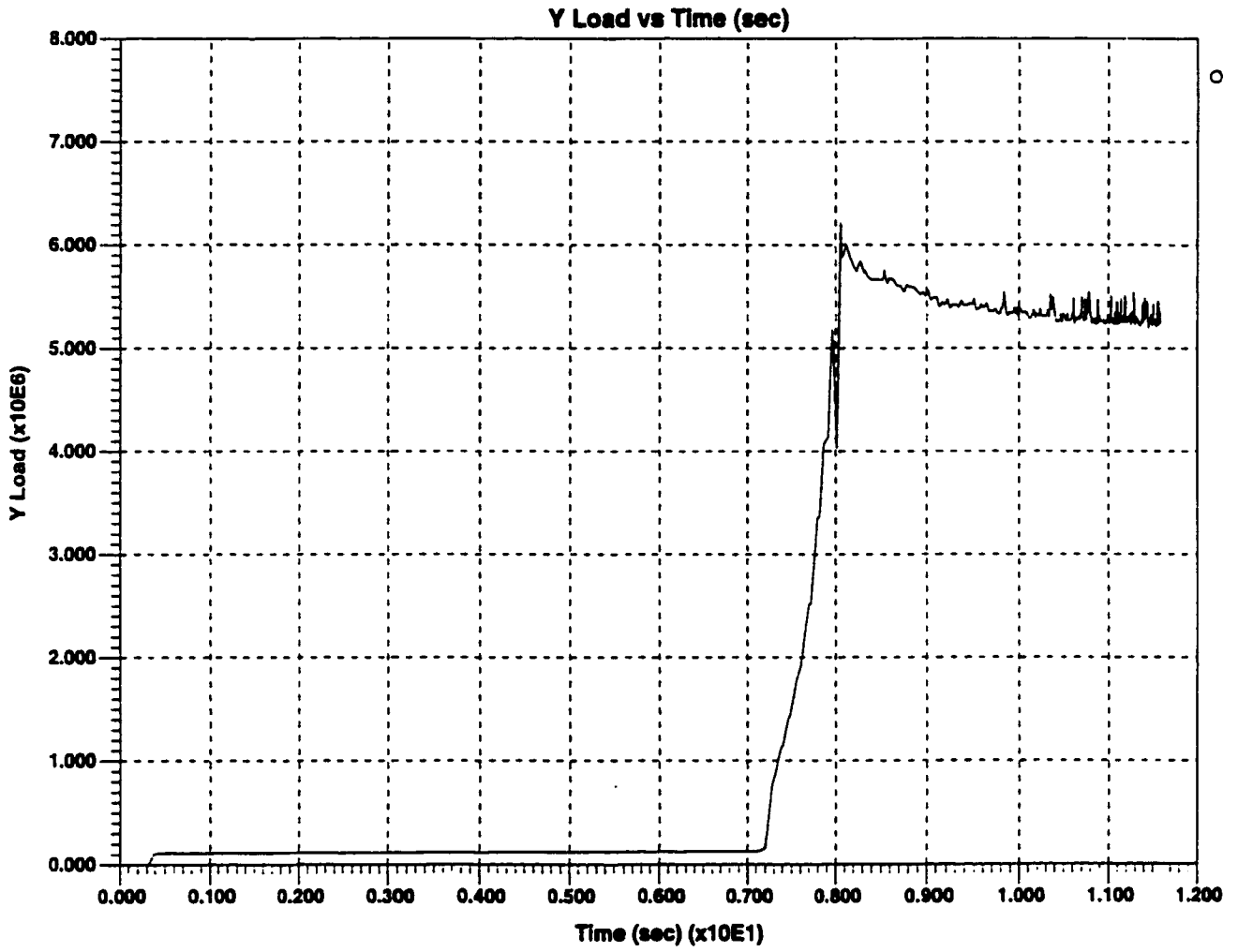

Figure 5.9: Typical Load versus stroke curve from DEFORM simulation

Simulation Name	Billet Temp (°C)	Ram Speed (mm/s)	Extrusion Ratio	Peak Load ($x10^6$N)	Max Temp (°C)	Max ε (s^{-1})	Max Velocity (mm/s)	σ_{MAX} (MPa)
6061IHTCOF	450	2.6	31	7	495	17.77	95.69	45.76
6061	450	2.6	31	7	495	17.77	95.69	45.76
6061T475	475	2.6	31	5.7	512	16.08	88.12	39.5
6061T500	500	2.6	31	5.1	532	17.46	97.5	32.2
Al10	450	2.6	31	7.6	500	17	95.12	53.37
Al10T475	475	2.6	31	6.5	518	21	95.3	47.36
Al10T500	500	2.6	31	5.7	538	18.1	98.04	39.49
15T450	450	2.6	31	8.5	501	19.65	95.7	40.19
15T475	475	2.6	31	7.2	521	18.4	96.4	47.08
15T500	500	2.6	31	5.8	540	20.66	95.8	55.08
20T450	450	2.6	31	10	509	16.13	86.9	45.93
20T475	475	2.6	31	8	527	16.3	94.76	48.82
20T500	500	2.6	31	6.2	543	16.5	93.7	66
20T450S5	450	5	31	11	530	36.8	188	42.27
20T500S5	500	5	31	7	556	34.7	185	49.97
6061T450S5	450	5	31	7.5	507	33.9	191	51.2
6061T500S5	500	5	31	5.5	546	31.8	192	39.12
15T450S5	450	5	31	9.3	518	38.6	189	55.66
15T500S5	500	5	31	6.5	552	35.6	189	42.08
10T450S5	450	5	31	8.5	517	34.3	186	55.37
10T500S5	500	5	31	6.5	553	37.3	192	43.98
6061T450S26R64	450	2.6	64	7.2	513	46.7	186	55.43
6061T500S26R64	500	2.6	64	5.6	551	37.4	185	42.34
10T450S26R64	450	2.6	64	9.5	520	32.8	184	53.44
10T500S26R64	500	2.6	64	6.6	556	33.6	192	37.07
20T450S26R64	450	2.6	64	11.5	534	40.4	177	57.3
20T500S26R64	500	2.6	64	7.5	562	36.4	174	43.7
6061T450S5R64	450	5	64	8.2	527	123.7	356	46.44
6061T500S5R64	500	5	64	6.5	564	75.9	361	
20T450S5R64	450	5	64	12.1	551	69.9	349	63.41
20T500S5R64	500	5	64	8.5	578	68.9	367	45.05

Table 5.4: Summary of modeling results

5.2.2 Temperature Profiles

The temperature contour plots for four distinct steps in a typical simulation are shown in figure 5.10. The contour plots are useful in determining where the maximum temperature occurs, at what step in the extrusion and the actual value as well as showing how heat is generated and how it flows in the billet. Figure 5.10 reveals the following information; Firstly, the billet is cooled by the ram from the top shown by the line marked "E" that moves downwards as the extrusion proceeds. Secondly, heat is generated at the die corner due to the large deformation that occurs at this location. The line marked "F" moves up from step 200 to step 500 and spreads heat towards the center of the billet. Thirdly the maximum temperature rises to its highest value for the entire simulation at step 300, then decreases and remains constant for the rest of the simulation. The maximum temperature is indicated by the small square and the value is given in the table 5.4. Objects 1,2,3,4,5 refer to the dummy block, die, chamber, billet and stem respectively. It was noticed that heat traveled quite easily through the billet whereas heat did not conduct well in the tools. This is expected since the thermal conductivity value for aluminum is much larger than that of H13 tool steel. The temperature profiles for the die, ram, stem and container remained relatively constant throughout the simulations because of their low thermal conductivity. In all of the simulations performed, similar results to the ones described above were found.

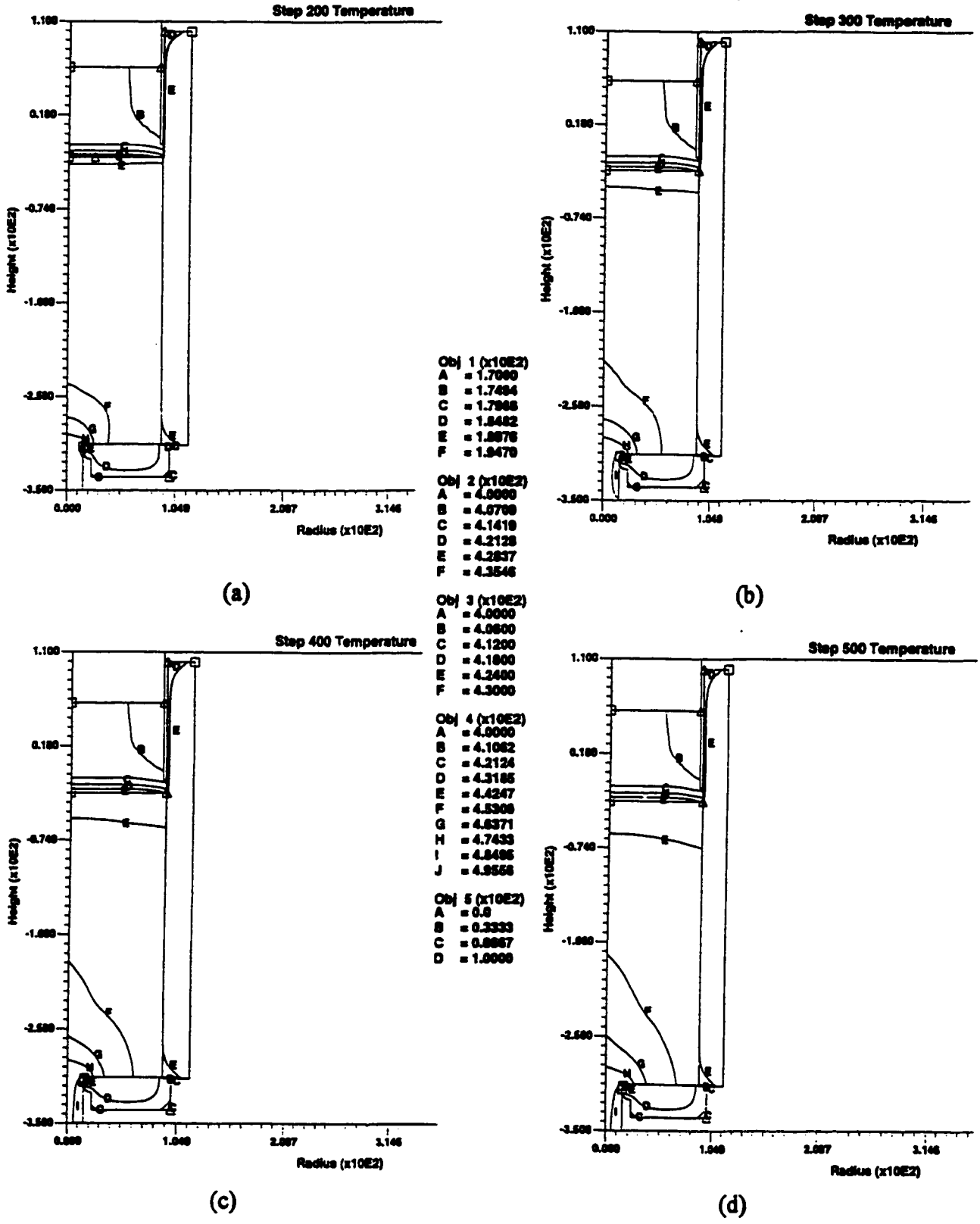

Figure 5.10: Temperature profiles for simulation 6061IHTCOF2 at step: (a) 200, (b) 300, (c) 400, (d) 500

5.2.3 Velocity Profiles

The velocity fields for three distinct steps in a simulation is shown in figure 5.11. The length of the arrows is proportional to the velocity of the material therefore it is evident from figure 5.11 that the material flows much faster at the die exit than in the container. At the beginning of the extrusion, the material velocity is very low as the billet expands to fill the chamber. Once the break-through point is reached, the material velocity increases very rapidly to reach a maximum value for the extrusion. After this point, the material velocity decreased slightly until a steady state value was reached. Figure 5.11a shows the point at which the material reaches its maximum velocity marked by the small square. The maximum velocity occurs on the centerline of the billet at the die exit. The minimum velocity is marked by a triangle and is located in the corner between the die and the chamber wall. This is representative of the "dead-zone" that exists in extrusions. Note that the triangle does not change locations and has a constant value of zero for the three steps shown in figure 5.11. Figure 5.11b and c show two steps during the steady state condition. The maximum velocity value in steps 400 and 708 varies very little which indicates steady state. Velocity profiles for all the extrusion simulations had the maximum velocity occurring just after the break-through point but the actual value varied depending on the initial extrusion conditions and when a steady state was reached.

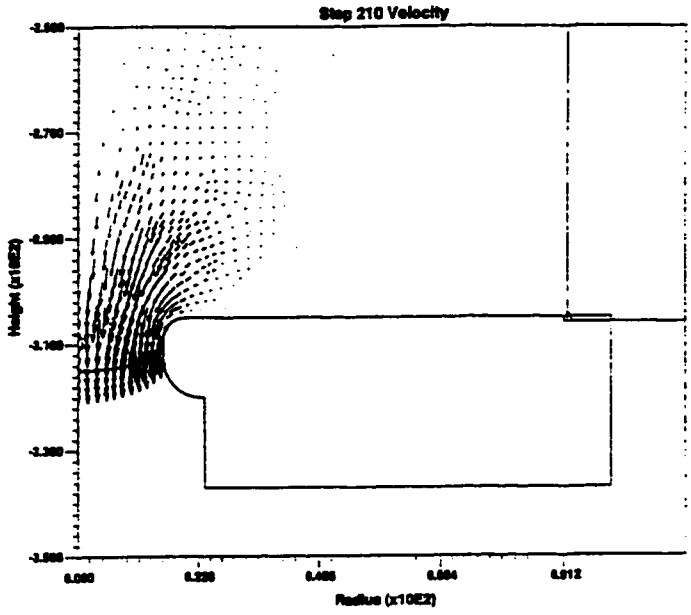

(a)

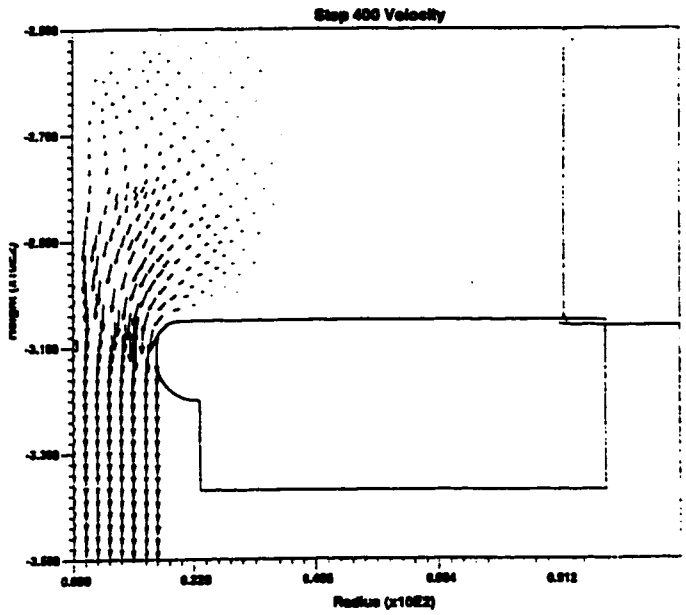

(b)

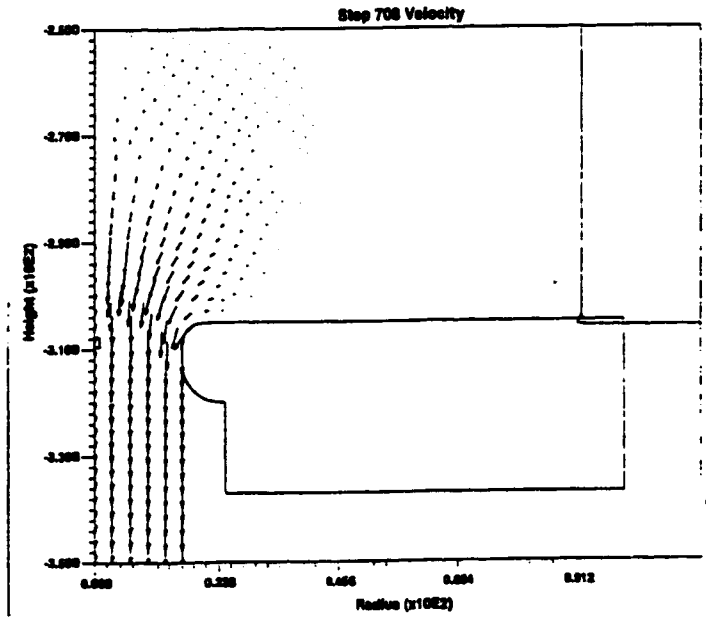

(c)

Figure 5.11: Velocity profiles for simulation 6061T450S5 at step: (a) 210, (b) 400, (c) 708

5.2.4 Stress Profiles

The stress profiles were calculated for the mean stress which is defined as the mean of all the normal stress components. If the mean stress is a negative value, a compressive stress state dominates. However, if the mean stress is positive, there must be a dominant tensile stress component [32]. Figure 5.12 shows the mean stress distribution at three distinct steps in the extrusion. The maximum stress occurs just at the break-through point and figure 5.12b and c show that the stress decreases from this maximum value to a steady state value. It is also evident that the stress state in the deformation zone is almost all compressive except in the surface layer near the die land.

5.2.5 Strain Rate Profiles

The DEFORM post-processor is capable of generating strain rate profiles at every step of a simulation which is useful in determining the location and at what time in the extrusion the maximum strain rate occurs. Figure 5.13 shows the progression of strain rate starting with the maximum value and two later steps. The strain rate reaches a maximum value at the die corner just as the material begins to exit the die as shown in figure 5.13a. After the maximum strain rate is reached, the strain rate decreases and reaches a steady state condition as illustrated by figure 5.13b and c.

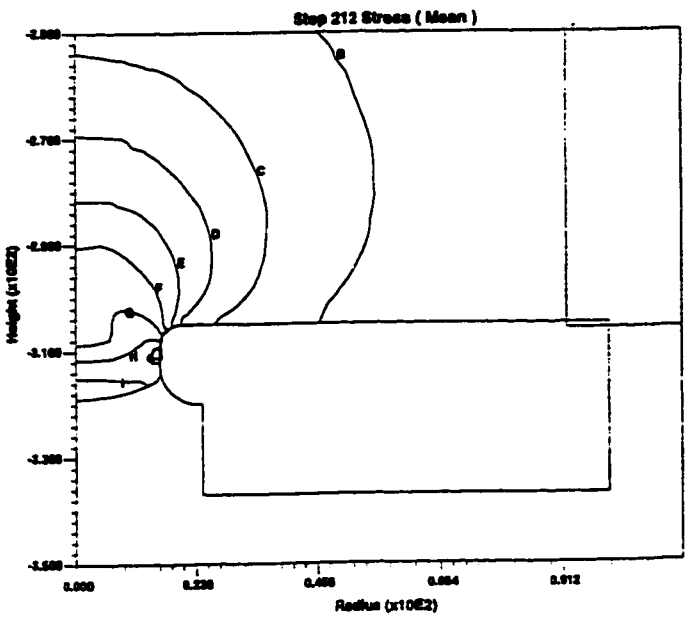

(a)

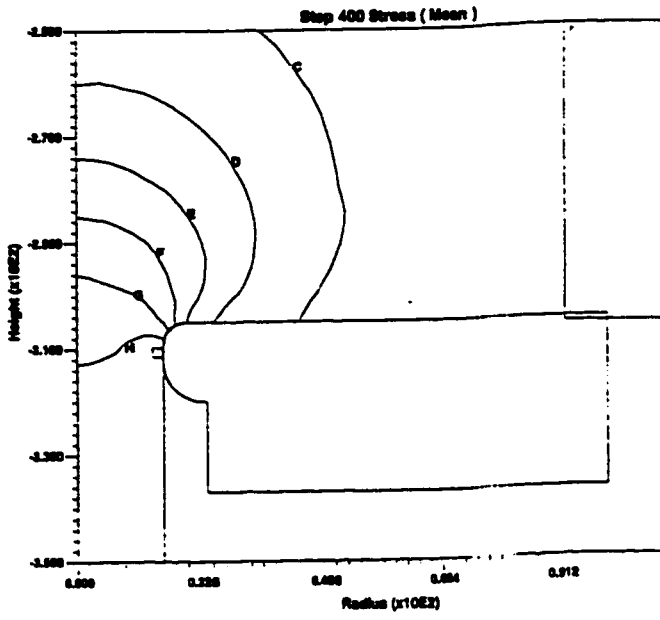

(b)

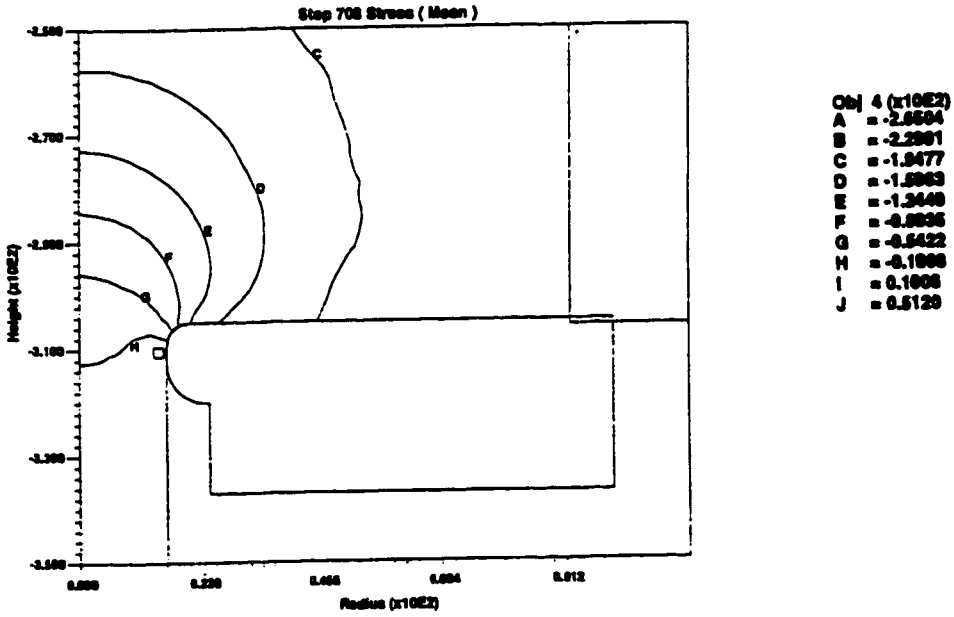

(c)

Figure 5.12: Stress profiles for simulation 6061T450S5 at step: (a) 212, (b) 400, (c) 708

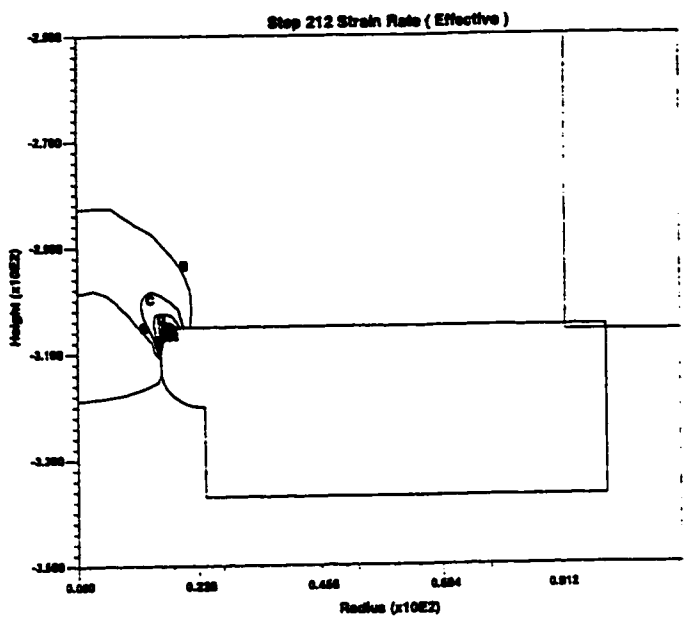

(a)

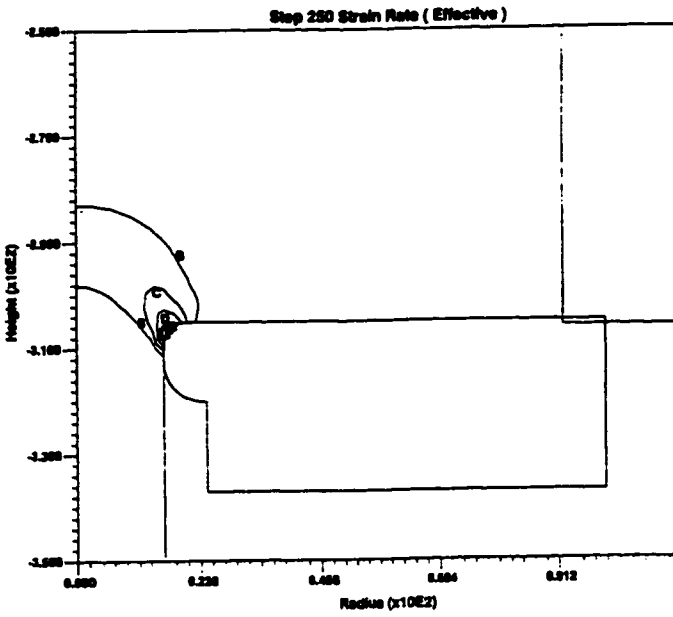

(b)

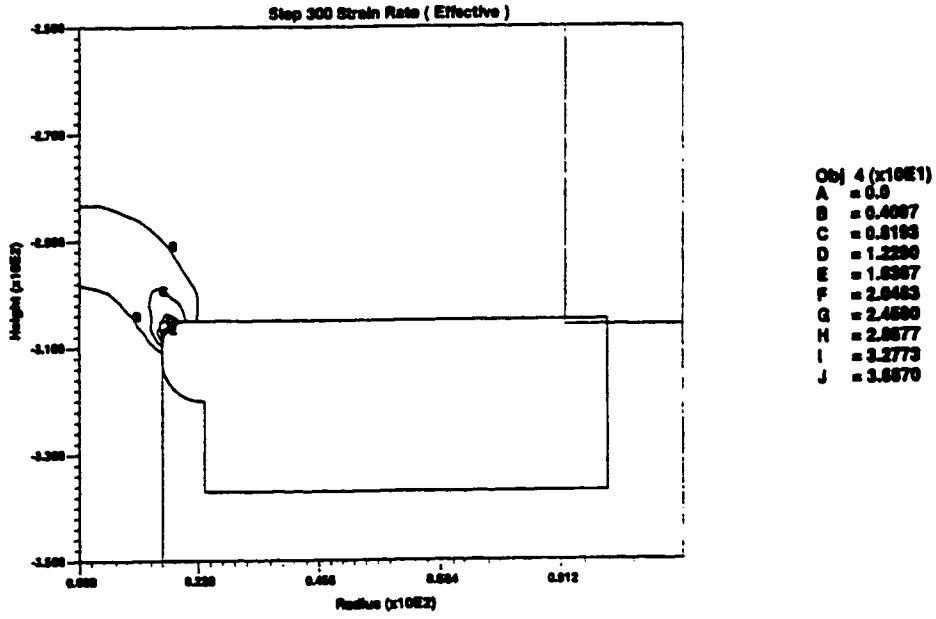

(c)

Figure 5.13: Strain rate profiles for simulation 6061T450S5 at step: (a) 212, (b) 250, (c) 300

5.2.6 Material Flow

The flow of material can be tracked in two different methods in the DEFORM post-processor; by point tracking and by using a flow net. Point tracking, as shown in figure 5.14, gives some insight into how points in the material flow. A number of initial points were chosen as shown in figure 5.14a. Figures 5.14b,c,d reveal that the material in the center of the billet moves most rapidly since point 15 for example moves the greatest distance but in the same time as the other points. Points 1 through 6 do not seem to move which indicates the existence of a dead metal zone.

The flow net illustrated in figure 5.15 demonstrates how square elements in the form of a mesh deform during an extrusion. Figure 5.15a shows the initial undeformed mesh and the subsequent figures show how this mesh deforms. The elements at the die corner appear to undergo more distortion than the elements closest to the centerline. The mesh also shows how material from the sides flows towards the center. This flow pattern will be discussed and compared to other researchers' work on extrusion.

5.2.7 Effect of Initial Billet Temperature

Varying the initial billet temperature has a significant effect on the peak ram load required to extrude the alloy and the MMC as is evident from figure 5.16. As expected, an increase in initial billet temperature lowered the flow stress and resulted in a decrease in the peak load for all four materials (figure 5.16). The load versus time (stroke=velocity/time) curves for the three different initial billet temperatures exhibit a

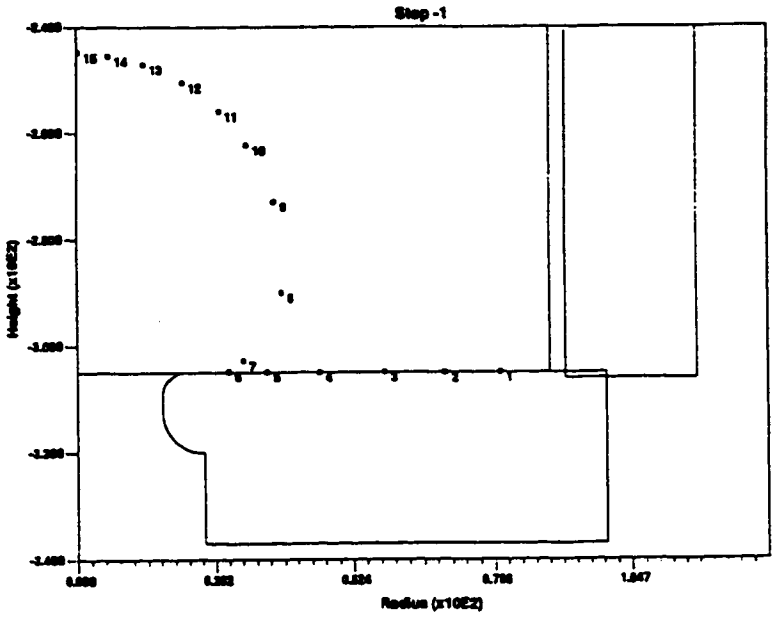

(a)

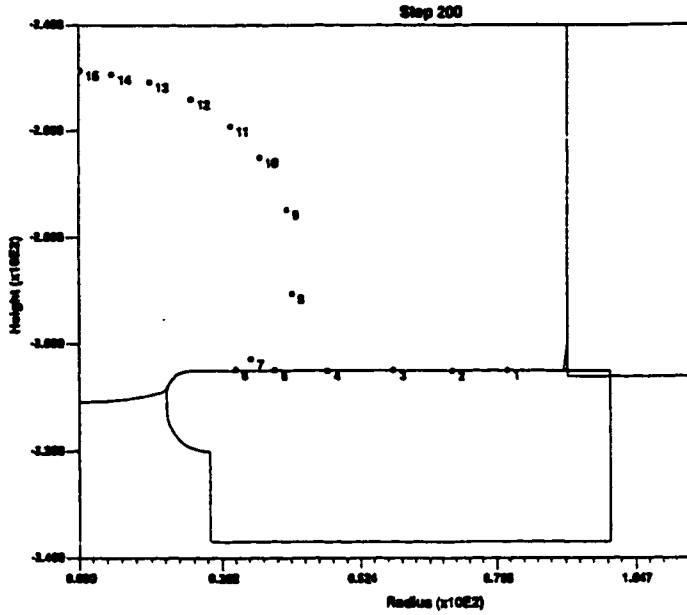

(b)

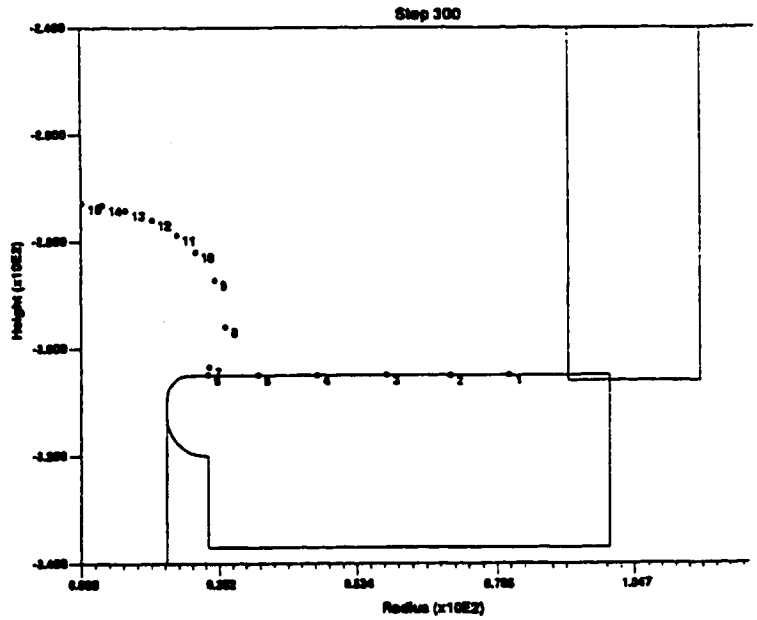

(c)

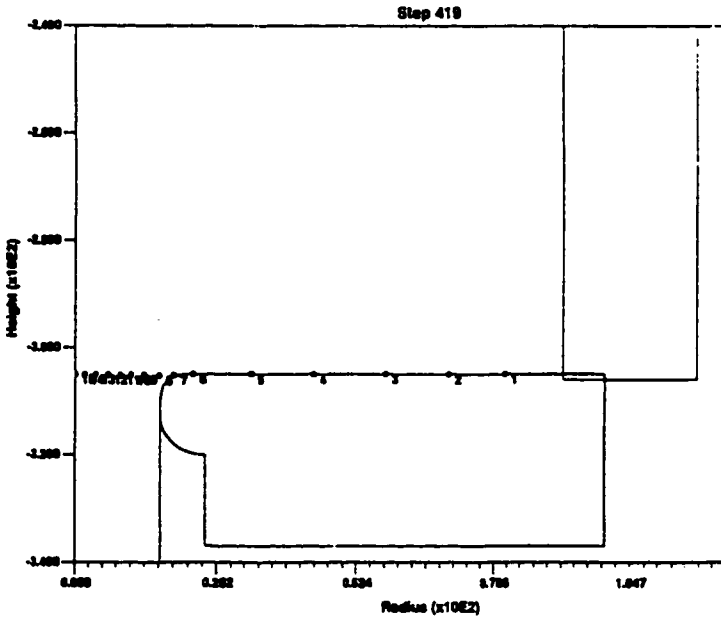

(d)

Figure 5.14: Point tracking for simulation 20T450 at step: (a) -1, (b) 200, (c) 300, (d) 419

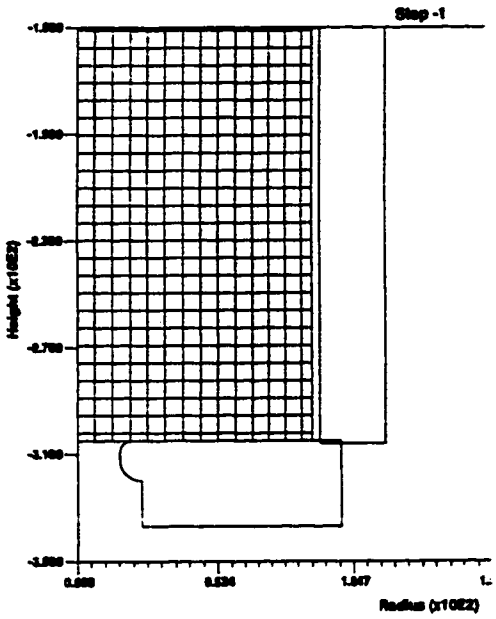

(a)

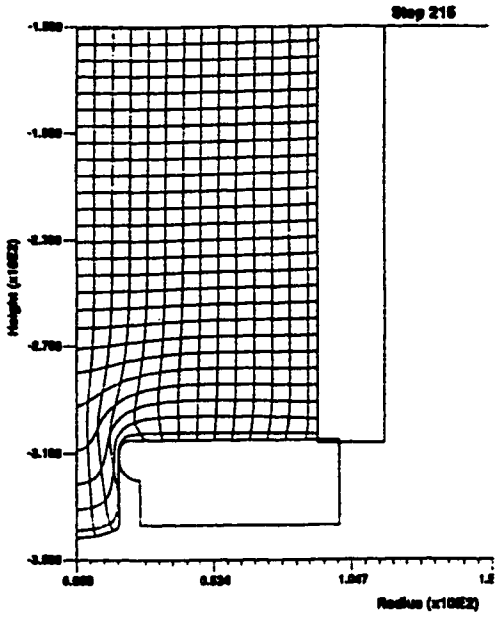

(b)

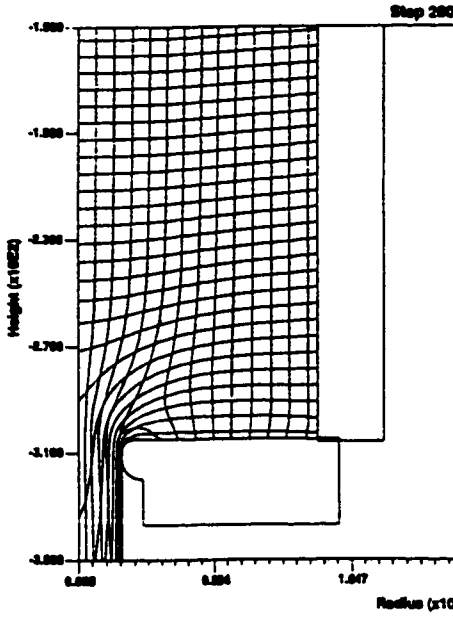

(c)

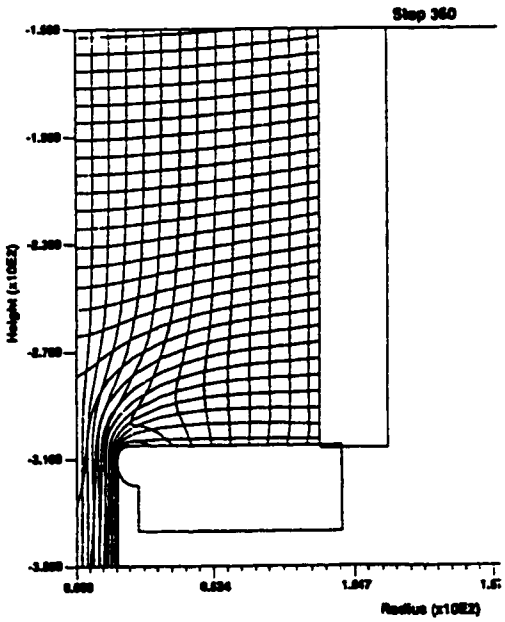

(d)

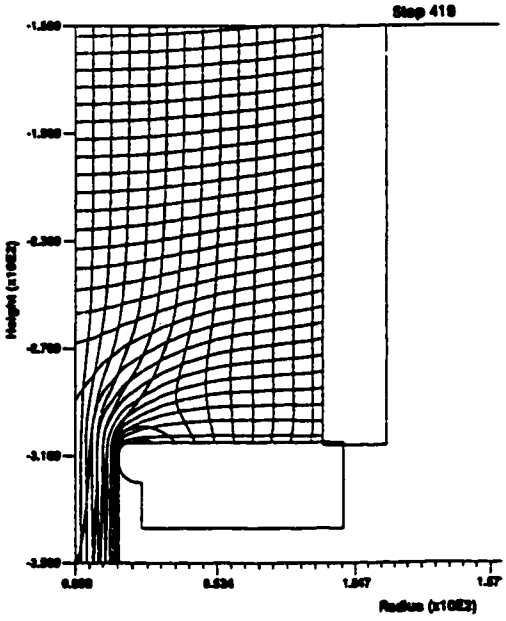

(e)

Figure 5.15: Flow net for simulation 20T450 at step: (a) -1, (b) 215, (c) 260, (d) 360, (e) 419

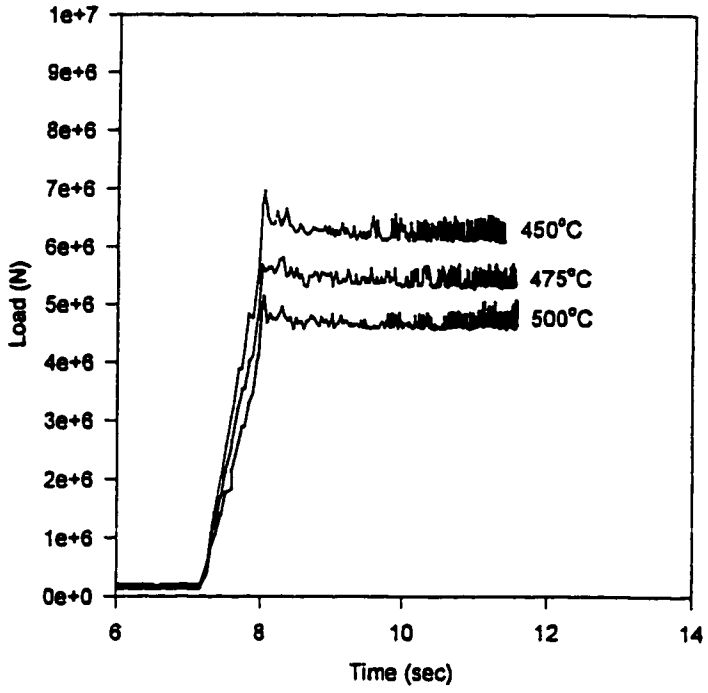

(a)

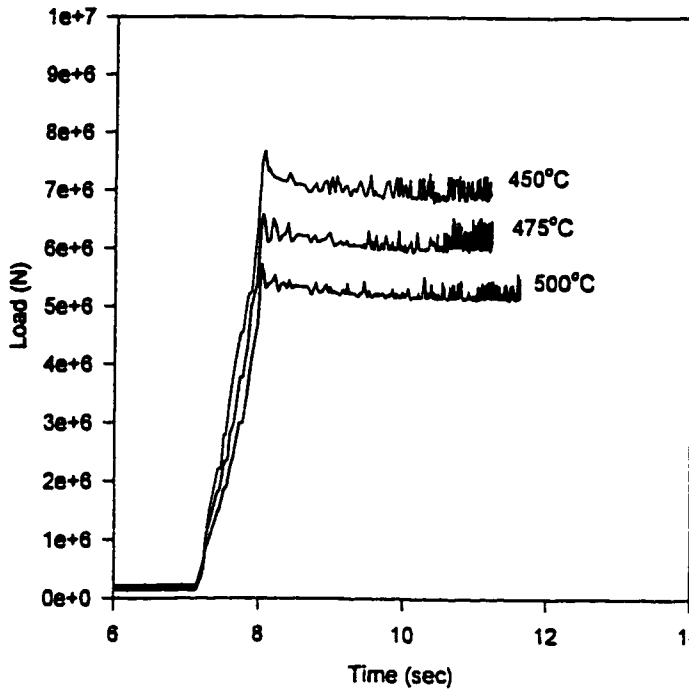

(b)

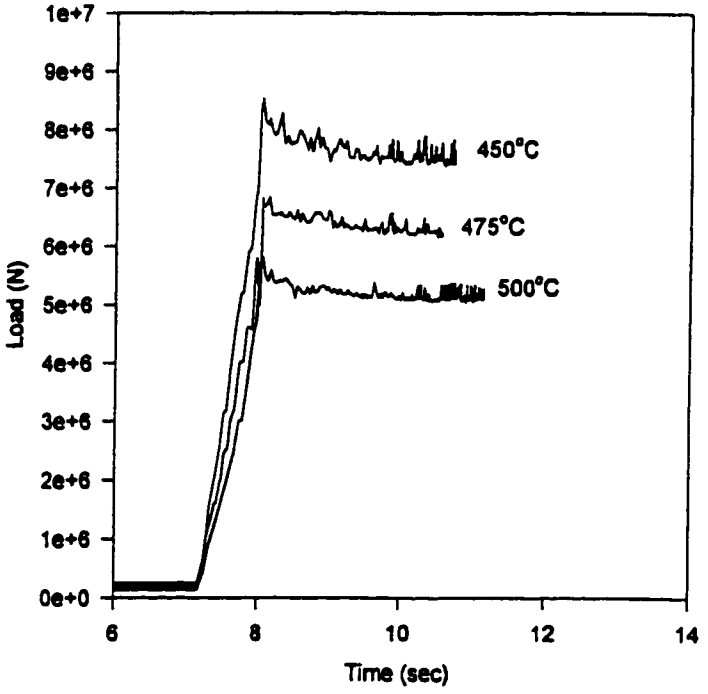

(c)

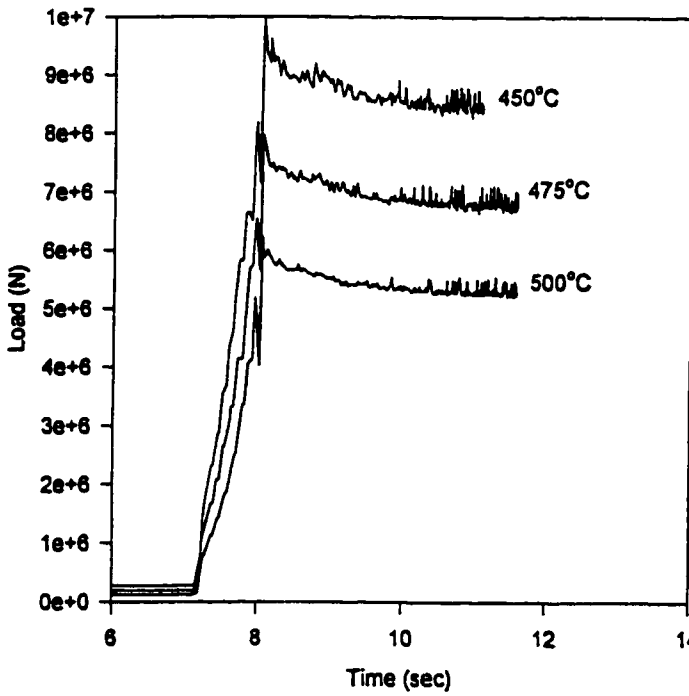

(d)

Figure 5.16: Effect of initial billet temperature on ram load with ram velocity =2.6mm/s and R=31 for: (a) 6061 Al, (b)10% Al_2O_3/6061, (c) 15%SiC/6061, (d) 20% Al_2O_3/6061

smooth decrease as the billet becomes shorter for all four materials. Although the curves are somewhat parallel, the load decreases more rapidly as initial billet temperature is decreased (higher initial pressure) for the alloy and MMCs. It must also be noted by comparing figures 5.16 a,b,c,d, load decreases more rapidly as percent reinforcement increases.

The greater the initial billet temperature, the greater the maximum temperature (Tmax) reached during extrusion (figure 5.17). For every initial billet temperature, Tmax increases with percent reinforcement. The rate of increase of Tmax with initial billet temperature is approximately the same for the alloy, the 10%Al_2O_3/6061 and the 15%SiC/6061 but the MMC reinforced with 20%Al_2O3 appears to increase less rapidly. This result is expected since raising the initial billet temperature for the strongest material has the greatest decrease in flow stress and hence in work and in temperature rise.

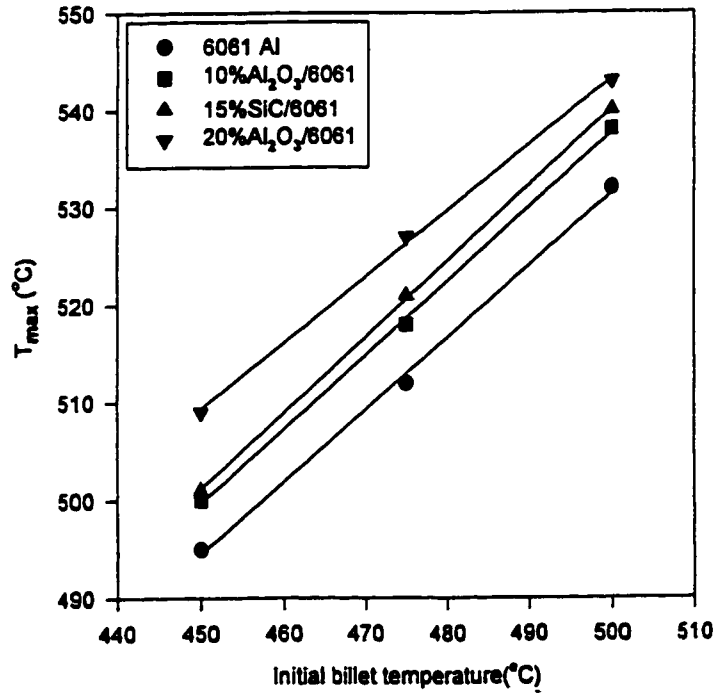

Figure 5.17: Effect of initial billet temperature on T_{max} for the alloy and the MMC (V_{ram}=2.6mm/s, R=31)

5.2.8 Effect of Ram Speed

An increase in ram speed results in an increase in ram load for all billet temperatures as shown in figure 5.18 for the 10% Al_2O_3/6061 MMC. Similar results are found for the 15% SiC/6061, 10% Al_2O_3/6061, and the 6061 Al as is evident from table 5.4. Almost doubling the ram speed resulted in an increase in load of approximately 12 to 15%. This is consistent with the effect of strain rate on σ as shown in figure 5.1 and 5.2.

Figure 5.19 shows the effects of ram speed on the maximum billet temperature reached during the extrusion. Since only two ram speeds were chosen, it is not certain if the relationship between ram velocity and maximum temperature is linear but it is certain that Tmax increases with ram velocity. The rate at which this occurs seems to increase with percent reinforcement although the 10% and 15% MMC have similar slopes.

The resulting maximum strain rate were plotted against ram speeds of 2.6 and 5 mm/s for the four materials as shown in figure 5.20a. As expected, an increase in ram speed results in a higher maximum strain rate and according to the simulation results the percent reinforcement has no effect on the maximum strain rate attained as demonstrated by the crossing lines. Figure 5.20b shows similar results for the relationship between ram speed and maximum extrudate velocity as for ram speed and maximum strain rate. The maximum extrudate velocity increases with ram speed but not enough different ram speeds were taken to determine if the relationship is linear or not. Percent reinforcement does not seem to affect the maximum extrudate velocity as demonstrated by the crossing lines.

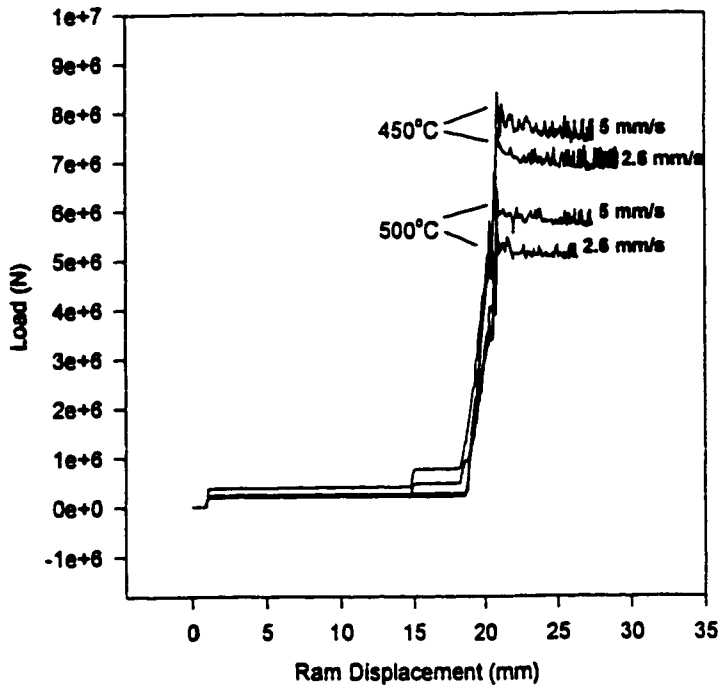

Figure 5.18: Effect of ram speed on ram load (10% Al_2O_3/6061 at 450 and 500°C)

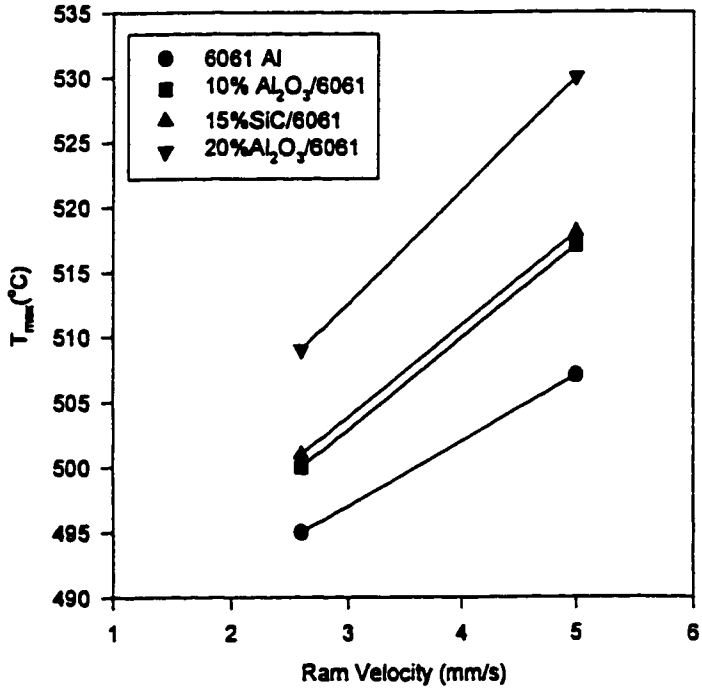

Figure 5.19: Effect of ram speed on Tmax (R=31, T_{billet}=450°C)

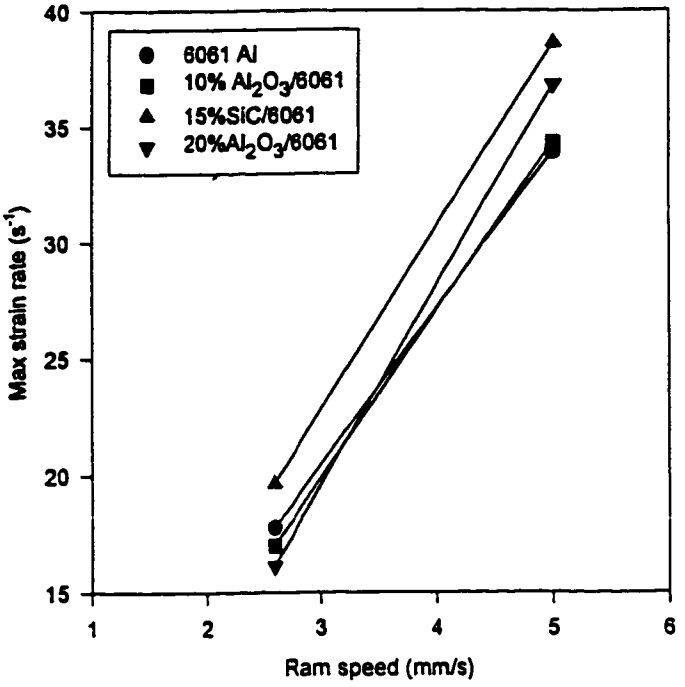

(a)

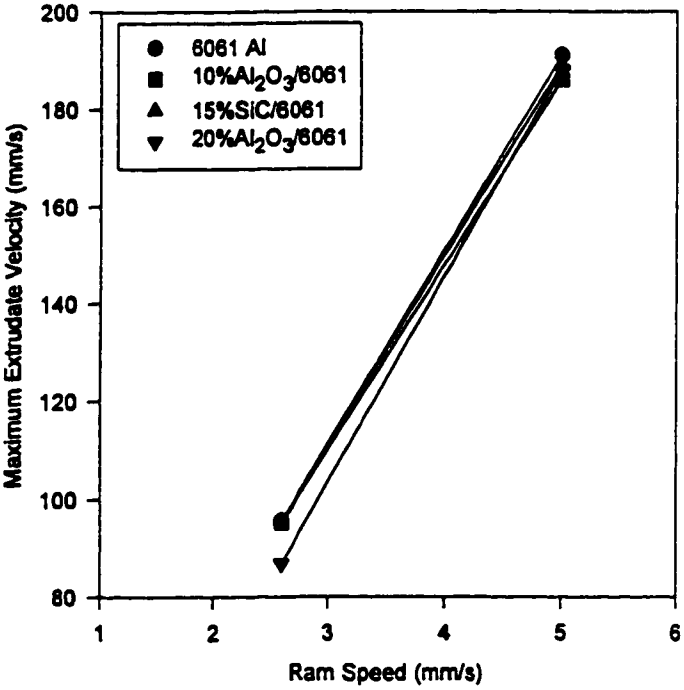

(b)

Figure 5.20 Effect of ram speed on: (a) maximum strain rate, (b) maximum velocity for (R=31, T_{billet}=450°C)

5.2.9 Effect of Extrusion Ratio

An increase in extrusion ratio from 31 to 64 resulted in an increase in ram load as shown in figure 5.21 for 20% Al_2O_3/6061. Similar results are found for the other MMC and the alloy. Load tended to decrease more rapidly with time (distance) for the extrusions having the higher ratio of 64.

Extrusion ratio has a significant and clear effect on the maximum temperature reached during extrusion. Figure 5.22 shows that maximum temperature increases with extrusion ratio and that percent reinforcement influences the rate at which this occurs. The slope of the lines increase with increasing percentage of reinforcement.

Figure 5.23a shows the influence of extrusion ratio on maximum strain rate. It can be stated that maximum strain rate increased with increasing extrusion ratio. Once again a linear relationship is only assumed. The rate at which maximum strain rate increases with increasing extrusion ratio tends to deminish more rapidly for the MMCs than the alloy. The difference between maximum strain rate values is greatest at the high extrusion ratios for all four materials due to the effect of percent reinforcement on the rate of maximum strain rate increase.

Figure 5.23b shows the relationship between extrusion ratio and maximum extrudate velocity. Maximum extrudate velocity increased with extrusion ratio and since the lines are parallel it indicates that percent reinforcement does not influence the rate at which this occurs. Maximum strain rate and maximum extrudate velocity are affected differently by a change in extrusion ratio. This could be related to the different location of

the maximum velocity (center of billet at die exit) and maximum strain rate (die exit corner). At the center of the die exit, strain rates are lower than at the die corner.

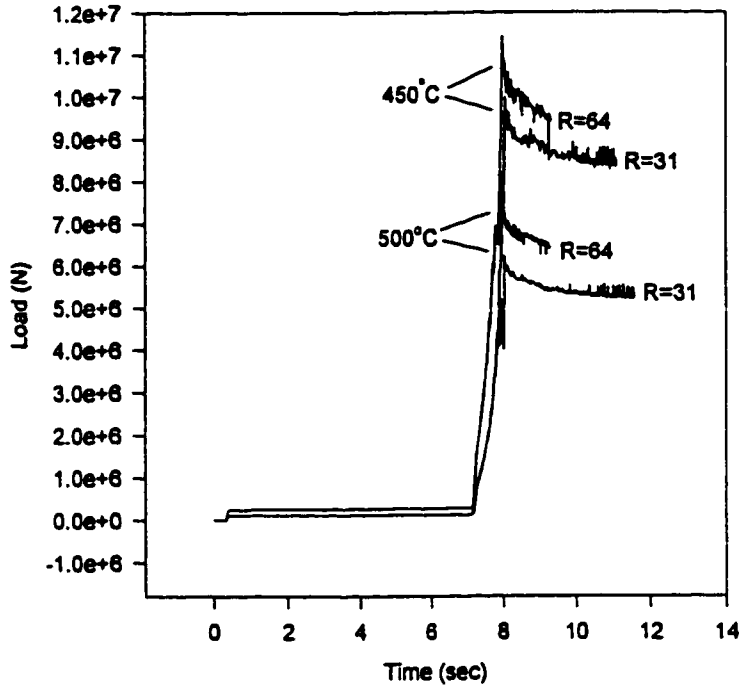

Figure 5.21 Effect of extrusion ratio on ram load (20% Al_2O_3/6061, T_{billet}=450 and 500°C, ram speed=2.6mm/s)

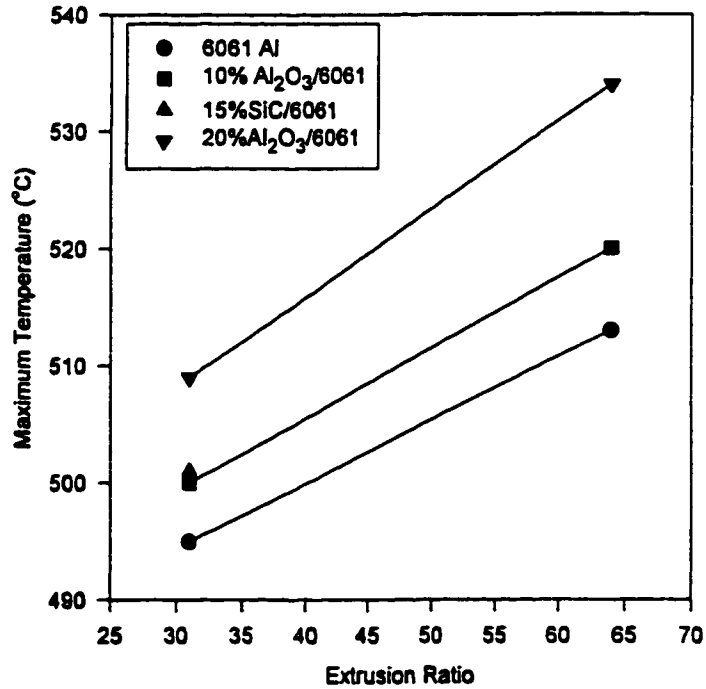

Figure 5.22: Effect of extrusion ratio on T_{max} (T_{billet}=450 °C, ram speed=2.6mm/s)

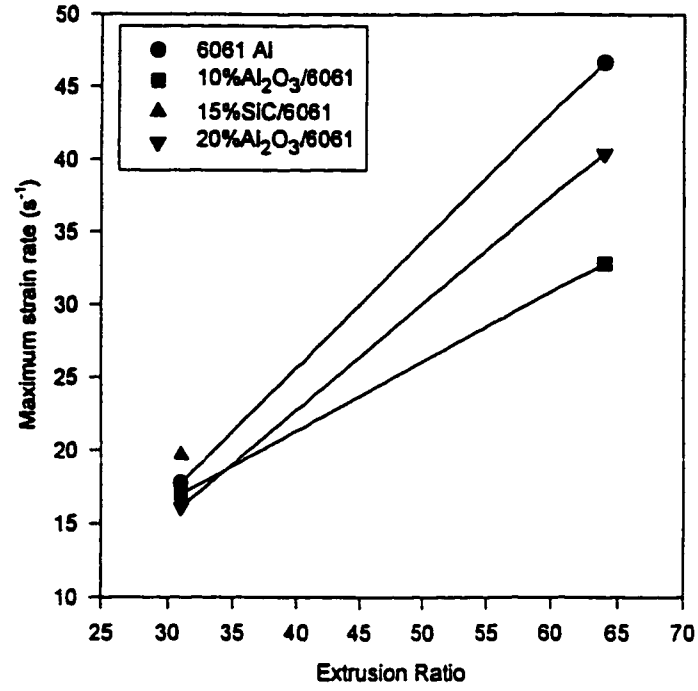

(a)

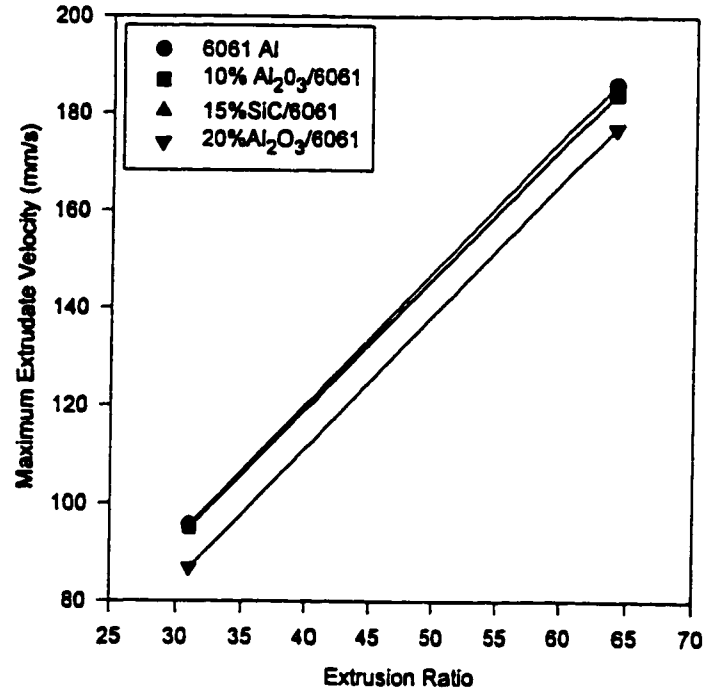

(b)

Figure 5.23: Effect of R on: (a) maximum strain rate, (b) Vmax. (T_{billet}=450 °C, ram speed=2.6mm/s)

5.2.10 Effect of Percent Reinforcement

Figure 5.24 demonstrates the effect percent reinforcement has on the load versus time (distance) curves at two different billet temperatures. At the lower initial billet temperature of 450°C there is a significant difference in peak load and the rate of decline of the load with respect to time. The 20% reaches the highest peak load and then declines most rapidly until a steady state is reached. As percent reinforcement decreases the peak load decreases and the rate of decline diminishes. At the higher billet temperature of 500°C, percent reinforcement has a much lesser effect on the load versus time (distance) curve. The 10% Al_2O_3/6061 and the 15%SiC/6061 for example have almost identical load versus time curves. The 20%Al_2O_3/6061 has the highest peak load and decreases most rapidly and the base 6061 alloy has the lowest peak load and remains almost constant through the extrusion which is somewhat similar to what occurs at the lower temperature of 450°C.

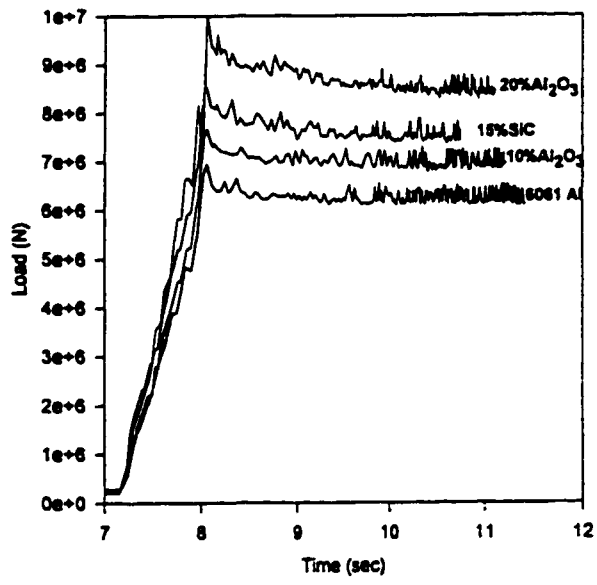

(a)

Figure 5.24: Effect of % particles on ram load for: (a) 450°C, (b) 500°C (T_{billet}=450 °C, ram speed=2.6mm/s)

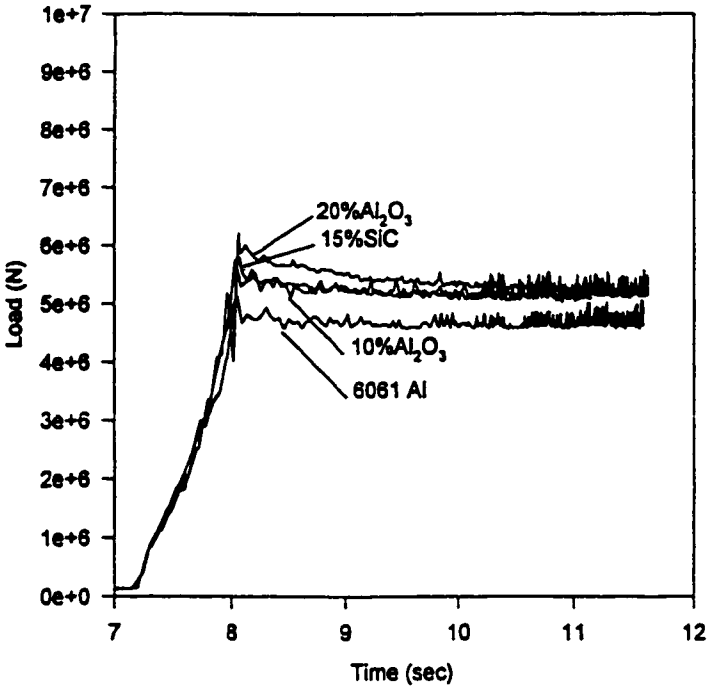

Figure 5.24 (b)

5.2.11 Interpolation of Results

Table 5.4 presents the results of simulations run with various extrusion conditions. One of the objectives of the present work was to determine under what conditions it is possible to extrude the MMCs with the same peak ram load as the 6061 alloy. Plotting the data from table 5.4 in the form of load versus initial billet temperature (figure 5.25), it is possible to interpolate the initial extrusion conditions required to obtain a desired peak ram load. For example, to extrude the MMCs with the same peak ram load as 6061 Al (ram speed of 2.6mm/s, extrusion ratio of 31, and initial billet temperature of 450°C), the MMC billets should be heated to the initial billet temperatures shown in table 5.5:

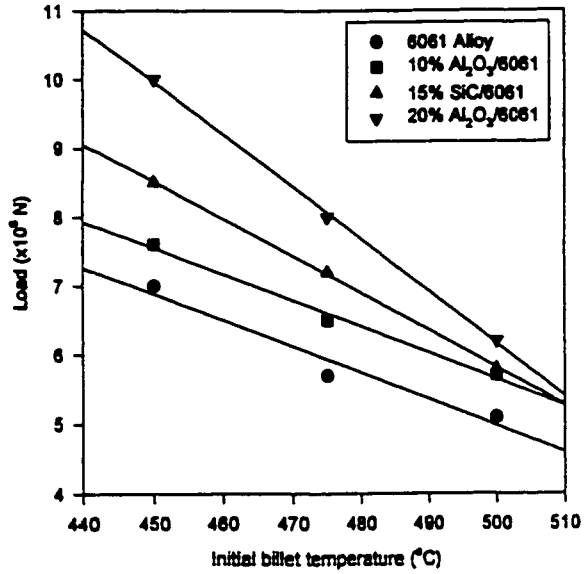

Figure 5.25: Interpolation of peak load for an initial billet temperature (R=31, ram speed=2.6mm/s)

Billet Material	Initial Billet Temperature (°C)	Tmax (°C)	Peak Ram load ($x10^6$ N)
6061 Al	450	495	7
10%Al_2O_3/6061	464	500	7
15%SiC/6061	479	501	7
20%Al_2O_3/6061	489	509	7

Table 5.5 Initial billet temperature interpolation results (R=31, ram speed=2.6mm/s)

The results in table 5.5 were obtained by drawing a horizontal line at a peak ram load of $7x10^6$ N, and reading the initial billet temperature from the points of intersection. Varying the initial billet temperature to achieve the same peak ram load for the production of a given extrusion from the four materials is but one method of achieving this. Varying ram speed is also possible as long as the maximum strain rate, maximum temperature, and maximum tensile stress are not exceeded. However, the extrusion limit diagram must be respected when interpolating initial extrusion conditions.

6. DISCUSSION

6.1 Load- Stroke Validation

According to extrusion theory, a direct extrusion with no lubrication should have a load versus ram displacement curve similar to curve #1 in figure 3.3a [37]. As discussed in chapter 3.3.1, once the peak load is reached, the load decreases with ram displacement and the rate at which this occurs decreases until a steady state value is reached. The reasons for the decline in ram load were found to be deformation and frictional heating which lowered the flow stress and as the billet proceeded into the extrusion, frictional stresses diminished. The load versus time or displacement for the present extrusion simulations were presented in figures 5.16, 5.24, and 5.9. An increase in initial billet temperature lowered the flow stress of the billet and resulted in a lowered load versus time curve. The curves for the alloy and the 10% Al_2O_3/6061 decrease less from the peak load to the steady state load than the 15%SiC/6061 and 20% Al_2O_3/6061 since there is less deformation heating in the materials with less percent reinforcement. The simulation results also showed that an increase in ram speed resulted in an increased ram load (figure 5.18) which is due to the flow stress increasing with an increase in strain rate as defined in the constitutive equation. Although it is not obvious from the load/ stroke curves in figure 5.18, it is expected that the rate of load decreasing would be greater for the case of higher ram speed since there is more deformation heating causing more softening. Increasing the extrusion ratio resulted in an increase in ram load as shown in figure 5.21. An increase in

extrusion ratio corresponds to more deformation therefore more work is required to extrude the billet and the load/ stroke curve moves up.

The present simulation results were validated by comparing the results to plant trials and simulations performed by Chen at UBC [32]. Two plant trials were modeled both with billets of 20%Al_2O_3/6061, ram speed of 2.6mm/s, extrusion ratio of 31, initial billet temperature of 430°C, but different billet lengths. Figure 6.1 shows the results of this comparison. Figure 6.1a shows that the peak values for ram load are almost identical for the present simulation, the plant trial and the UBC simulation but the time at which the peak value is reached varies. It was suggested by Chen that this shifting of the peak to the left for the simulations was probably due to the assumption of completely rigid tools (no deflection) in the modeling. In reality, there is deflection of the tooling which makes it necessary for the ram to advance further before the billet begins to extrude. The other significant difference between simulation and plant trial is the rate at which the peak load is reached. For both the present simulation and Chen's simulation, there is a rapid rise in load during the upsetting stage whereas this occurs much less rapidly for the plant trials. This variation between simulation and plant trial can be explained by tool deflection and the effects of a dirty chamber combined with oxide on the billet surface which would extend the time for completion in the plant trials. The disparity between the present simulation and Chen's are due to differences in boundary conditions and input values. Different constitutive constants were used for the material flow stress, a different interface heat transfer coefficient was used which affects the amount of heat transfer from the billet to the tools, different material thermal properties and different boundary conditions were

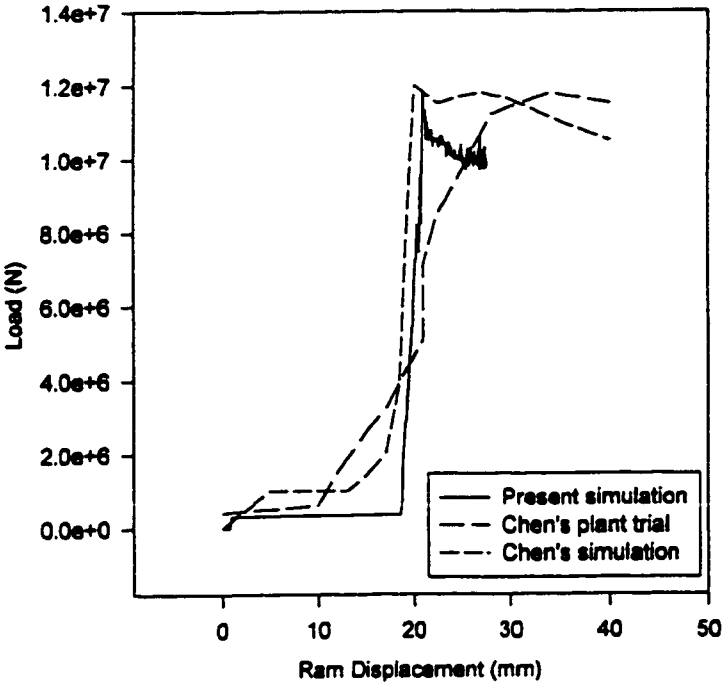

(a)

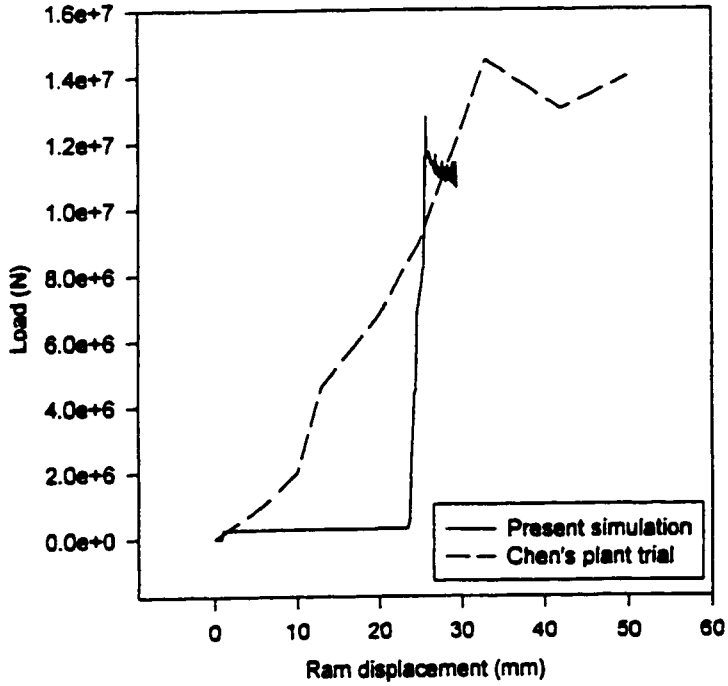

(b)

Figure 6.1: Comparison to Chen's work (20% Al_2O_3/6061, T_{billet}=430, V_{ram}=2.6mm/s, R=31): (a) billet length=305mm, (b) billet length=381mm [32]

applied. Chen assumed that the top of the ram and the bottom of the die were exposed to ambient air which would cool the tooling more rapidly than what occurs in real plant trials where the ram and die are in contact with other tools. In the present simulation, a stem was added to the dummy block, therefore conduction was the mode of heat transfer as opposed to convection to the environment as in Chen's model [32]. The present simulation exhibited a greater decrease in load with respect to time due to the slower cooling rate of the billet resulting from the choice of boundary conditions as mentioned above.

Fluctuation in the load prediction after the peak had been reached was found to be caused by a node in the billet losing contact with the die and consequently the extrusion force dropped. DEFORM attempts to compensate for the node separating from the die and causes a rapid increase in extrusion force, thereby creating the "jagged" fluctuations. A possible method of solving this problem is to refine the billet mesh at the die throat but this would increase computer processing time significantly [32].

6.2 Temperature Profile Validation

At the beginning of the extrusion, the billet is cooled from both ends due to the lower initial die and ram temperatures, which in turn heats up the ram and die. After the upsetting stage, heat is generated in the billet due to deformation heating. It was found that temperature increased approximately 60°C for the 20% Al_2O_3/6061 and 45°C for the alloy for an extrusion ratio of 31, initial billet temperature of 450°C, and a ram speed of 2.6mm/s. Chen found a temperature rise of 70°C due to deformation heating for the

simulation of 20% Al_2O_3/6061 with similar extrusion conditions. The present simulation had a greater temperature rise than Chen's since the initial temperature of the dummy block was 100°C higher in the present simulation. Figure 5.10 revealed that the temperature contour lines were much closer together in the tooling than in the billet which would indicate a greater thermal gradient in the steel. This is justified, since the thermal conductivity of aluminum is six times higher than that of H13 tool steel. It was also noticed in the work at hand and by Chen that at the interface, the tools had lower temperatures than the billet. This phenomenon is due to the thermal resistance at the tool-billet interface and is controlled by the interface heat transfer coefficient in the DEFORM software [32].

Grasmo et al. [47] found similar results to the present work and that of Chen's. It was found that ram temperature rose rapidly at the early stages of the extrusion due to the large difference in temperature between the billet and ram. The rate of increase in ram temperature then decreased as the ram moved forward. As the ram moved towards the die, the rise in temperature reduced the flow stress of the billet, resulting in less energy required to deform, therefore less deformation heating. As the relatively cold ram approached the die, a substantial amount of heat was transferred in the direction opposite to the extrusion direction. A more rapid loss of heat combined with decreasing frictional area and volume of the billet, caused the die temperature to flatten out and even decrease towards the end of the extrusion [47]. In the present work, die temperature rose to a maximum value and remained constant throughout the simulation.

6.3 Velocity Profile Validation

The velocities of the billet material at the die exit were higher than those in the container as shown in figure 5.11 because of the high extrusion ratio. The maximum velocity occurred just as the billet begins extruding which is the same instant that ram load, strain rate, and stress reached their maximum values. Stress in the billet near the die corner reaches a maximum value equal to the peak flow stress of the material. Since the billet behaves rigidly up until the flow stress is reached (negligible elastic deformation is assumed), there is a sudden and rapid flow of material which begins at the center of the billet. Frictional forces between the die and the extrudate impede material flow therefore the maximum velocity occurs at the point furthest from the die surface along the centerline. Once the "break-through point" (peak ram load) is reached, stress drops due to a rise in temperature and reaches a steady state condition as deformation heating is balanced by heat loss. Extrudate velocity and strain rate remain constant after the break-through point since ram velocity remains unchanged.

Bhattacharyya et al. [44] obtained velocity contours as shown in figure 6.2 in their FE modeling of lead extrusion using software called "PHOENICS". From figure 6.2a it is evident that velocity increases towards the deformation zone and a maximum is reached (arrow length is proportional to velocity) on the axis of symmetry where the material passes through the die. A dead zone exists at the corner of the die and container marked by a zero velocity contour line. However the dead zone is significantly smaller than in the present work due to lower frictional forces. Experimental work on the extrusion of lead revealed that lines of constant velocity formed concentric circular arcs of decreasing

magnitude moving away from the center of the die as shown in figure 6.2b [44]. Similar results were obtained in the present work as shown in figure 6.2c where the maximum velocity occurs along the centerline during the entire extrusion. Concentric contour lines of constant velocity shown in figure 6.2c are similar in shape to the experimental results in figure 6.2b.

(a) (b)

Figure 6.2: Bhattacharyya's velocity contours: (a) predicted, (b) experimental [44]

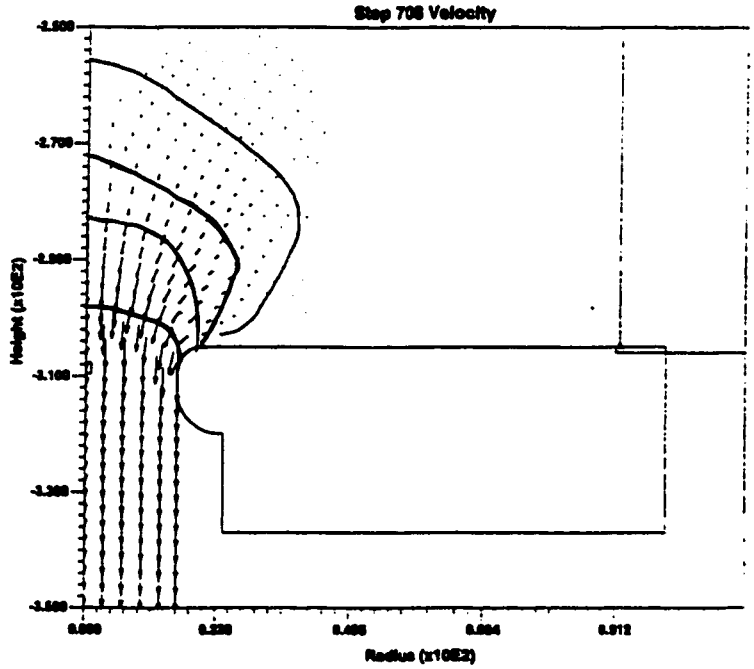

Figure 6.2 (c) Present velocity contours

6.4 Stress Profile Validation

The absolute value of the mean compressive stress in the container decreases from the pressure end to a minimum of zero at the die exit, which indicates that the billet seems to be in tension in the extrusion direction when approaching the die exit. At the die exit, tensile stresses exist as shown in figure 5.12a. These tensile stresses are primarily due to the faster flow of material in the center than at the surface where there is high friction stress at the die land surface [32]. Such tensile stresses at the surface in the die land region could lead to cracking particularly if it interacts with hard particles or weak phases as described in section 3.3.4.

6.5 Strain Rate Profile Validation

It is seen from figure 5.13 that the strain rate distribution is confined to the die corner zone and the contour lines are similar to those obtained by Chen [32] and Bhattacharyya [44]. The maximum strain rate occurs at the die exit corner where the surface of the extrudate forms from the extension of the interface between the shear zone and the dead zone [32].

6.6 Flow Pattern Validation

According to extrusion theory as discussed in chapter 3.3.1, the flow pattern is greatly influenced by the friction conditions between the billet and chamber. The flow pattern shown in figure 5.15 shows the early stages of the extrusion. Due to limitations of the DEFORM software, it was not possible to run the flownet or point tracking from the

beginning to the end of the extrusion therefore the flow pattern and tracking points do not reach the chamber wall. This makes the comparison to flow patterns such as the ones shown in figures 3.6 and 6.3 somewhat difficult. However, certain remarks and similarities between the present simulation results and the work of others can be stated.

Valberg et al. [60] obtained a flow pattern as shown in figure 6.3 for the actual extrusion of 6063 aluminum alloy. Initially, horizontal grid lines were machined into the right half of the billet and vertical grid lines on the left side. After partially extruding the billets to different stages, the diametral sections were cut to reveal the flow patterns. Step 1 of figure 6.3 shows an early stage of the extrusion where it is evident that sticking is occuring along the chamber wall and the material along the centerline is moving faster particularly near the die opening. The existence of a dead zone is evident from figure 6.3 and its size remains constant in the four steps shown [41]. In the present work, the existense of a dead zone was demonstrated by point tracking in figure 5.14 which shows that points selected along the die away from the die opening remained fixed during the extrusion. The flow pattern shown in figure 5.15 shows that the material in the center of the billet moves fastest and the elements along the container wall appear to be sticking. In order to completely validate the flow pattern obtained in the present work, a continuation of the flownet and the point tracking would be necessary.

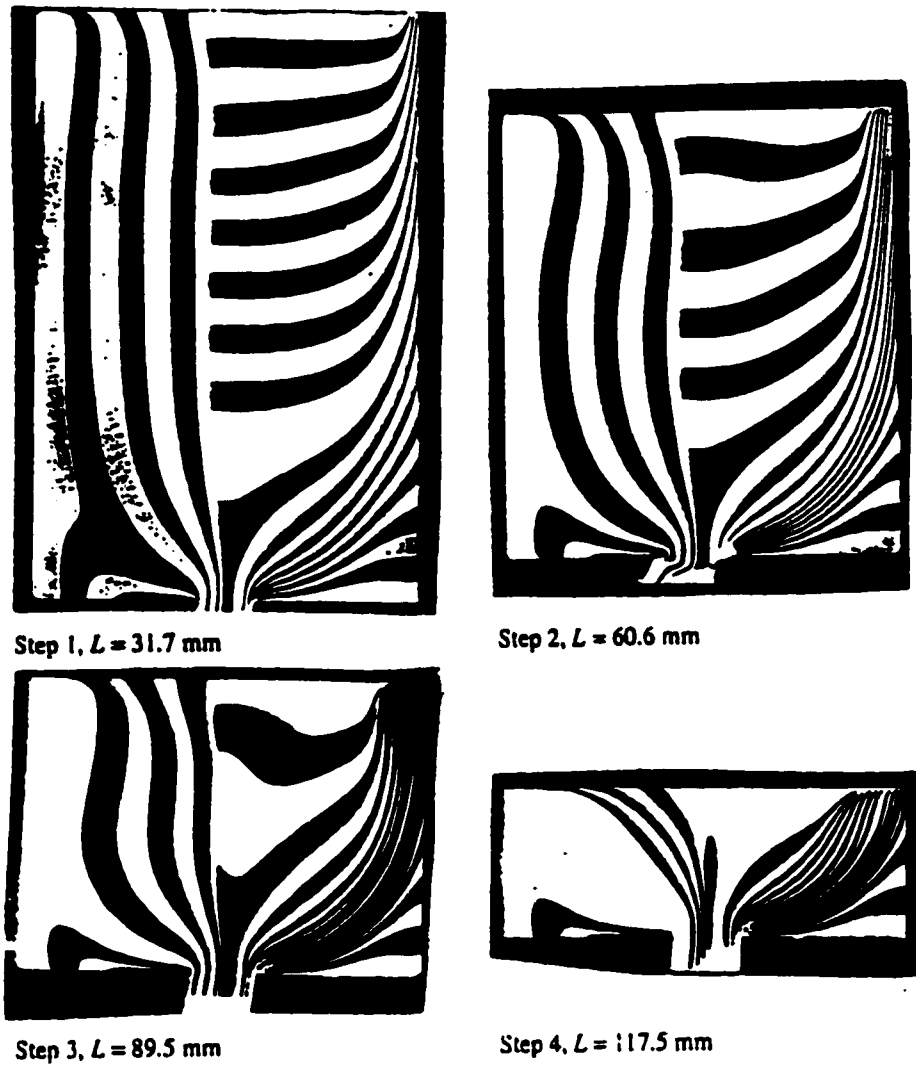

Figure 6.3: Valberg's experimental flow pattern for four steps in an extrusion [60]

6.7 Comparison to 2618 Al and the MMC

Extrusion modeling of 2618 Al alloy and the MMC reinforced with Al_2O_3 particles was undertaken by McQueen and Sauerborn using the same model and software as in the present work. Comparison of the present work with that of McQueen and Sauerborn will demonstrate the effects of changing the billet material on the extrusion process. The alloy, 2618 Al has the chemical composition as shown in table 6.1 and can be compared to that of 6061 Al.

Material	Composition (wt%)									
	Mg	Si	Cu	Fe	Cr	Zn	Ti	Mn	Ni	Al
2618 Al	1.6	0.18	2.3	1.1	—	—	0.07	—	1.0	rem.
6061 Al	0.97	0.71	0.28	0.58	0.24	0.045	0.016	0.04	—	rem.

Table 6.1; Chemical composition of 2618 Al compared to 6061 Al.

The higher percentages of Mg, Cu and Ni in 2618 Al results in higher tensile and yield stengths than the 6061 Al at all temperatures therefore the extrusion of 2618 requires a greater ram force and more heat is generated. Extruding 2618 Al and the MMC is considerably more difficult than extruding the present materials for several reasons;

- A greater ram force is required for 2618 because of its higher flow stress.

- The incipient melting point of 2618 is quite low (502 °C), therefore the danger of melting is greater. The solidus temperatures of 2618 and 6061 Al are 549 and 582°C respectively.
- The thermal conductivity of 2618 is lower than that of 6061 (146 W/m-K versus 180 W/m-K) therefore the heat that is generated during deformation is dissipated throughout the 2618 billet less easily [61].

The extrusion modeling of 6061 and 10% Al_2O_3/6061 was compared to 2618 and 10% Al_2O_3/2618 respectively for the same initial extrusion conditions (initial billet temperature=450°C, ram speed=2.6 mm/s, and extrusion ratio of 31). Figure 6.4 demonstrates the increased ram force required to extrude 2618 as compared to 6061 (approximately 30% more force). The curves decrease at roughly the same rate and level off which indicates that both alloys experience little deformation heating under these extrusion conditions. However, the addition of reinforcement particles to these alloys seems to have a greater effect on the 2618 alloy. Figure 6.5 shows that the required ram load for the 10%Al_2O_3/6061 increased approximately 8%, whereas the 10%Al_2O_3/2618 increased almost 40% when compared with the unreinforced alloy. It can also be noted that the curve decreases more rapidly for the 2618 MMC than the 6061 MMC which indicates greater deformation heating. The amount of deformation heating generated is sufficient to raise the billet temperature beyond the incipient melting temperature thereby causing localized melting. The maximum temperature reached under these extrusion conditions for the 2618 MMC was 517°C but the incipient melting point is 502°C which indicates that the initial extrusion conditions are not satisfactory. The maximum

temperature reached in the 6061 MMC was 500°C which is far below its solidus temperature of 582°C. The solidus temperature was taken as the limiting value of the maximum temperature for the 6061 and its MMC since it was assumed that the billets were homogeneous making the incipient melting temperature close to the solidus temperature. These results therefore demonstrate that 2618 MMC cannot be extruded with these initial conditions and that the extrudability of 2618 MMC is less than that of 6061 MMC.

McQueen and Sauerborn varied the initial billet temperature and ram speed in order to extrude the 2618 alloy, 10% and 20% Al_2O_3/2618 without exceeding the incipient melting temperature. Table 6.2 presents these initial extrusion conditions. It is evident from table 6.2 that to extrude the MMC, both initial billet temperature and ram speed needed to be reduced.

Billet Material	$T_{billet\ initial}$ (°C)	R	V_{ram} (mm/s)	T_{max} (°C)
2618 Al	425	31	2.6	491
10% Al_2O_3/2618	425	31	1.5	493
20%Al_2O_3/2618	425	31	1.5	495

Table 6.2; Acceptable initial extrusion conditions for 2618 Al and the MMC.

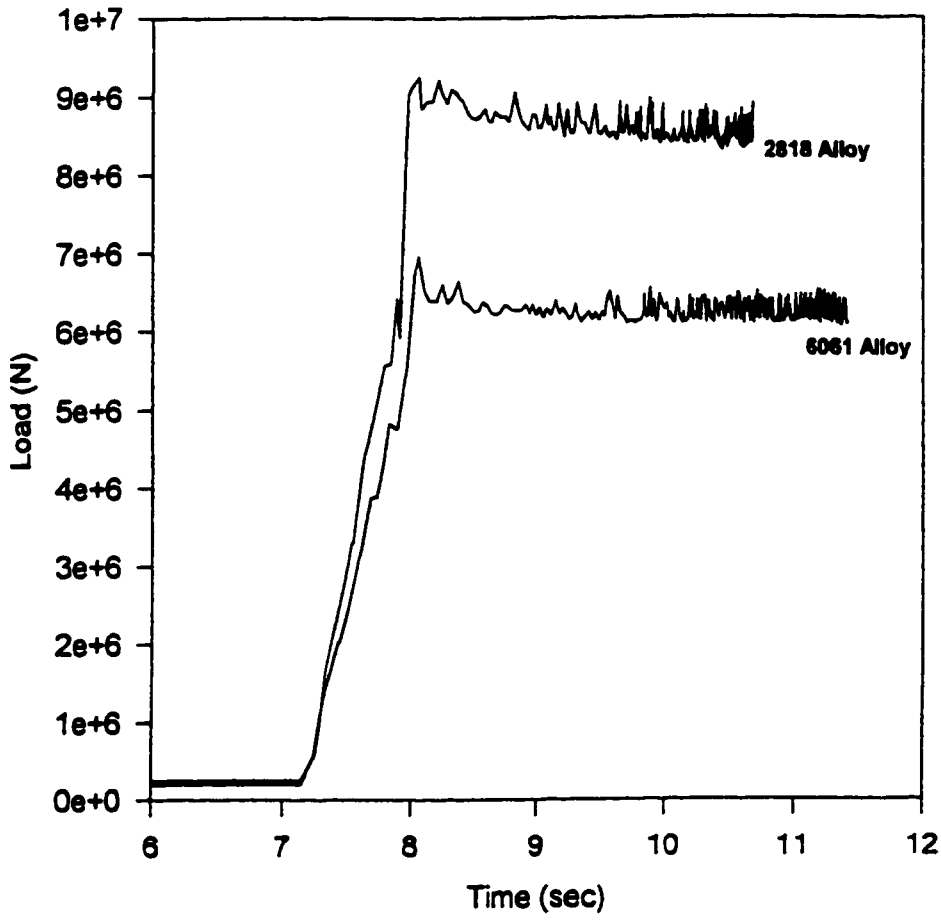

Figure 6.4: Comparison of simulation results of 6061 Al and 2618 Al. (T_{billet}=450 °C, ram speed=2.6mm/s, R=31)

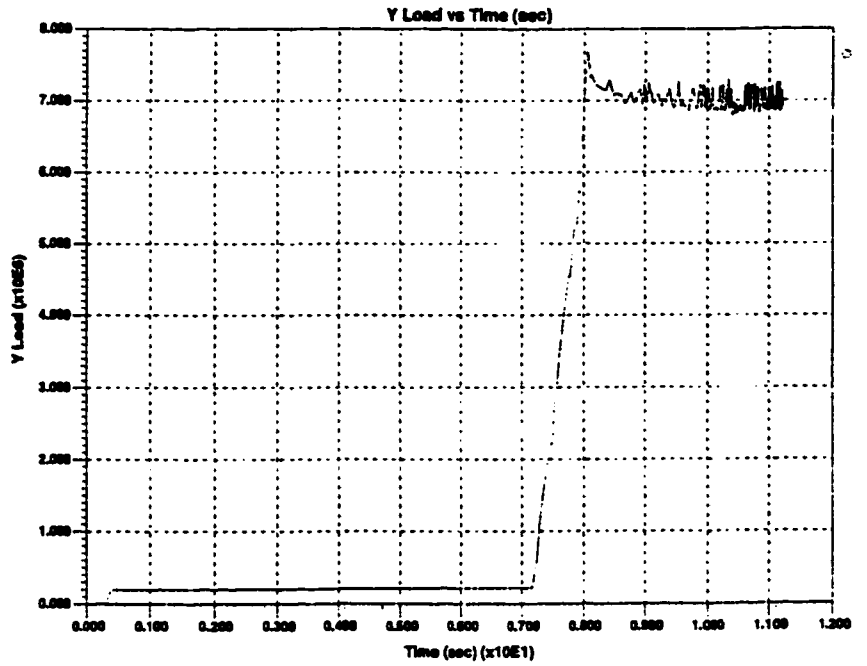

(a)

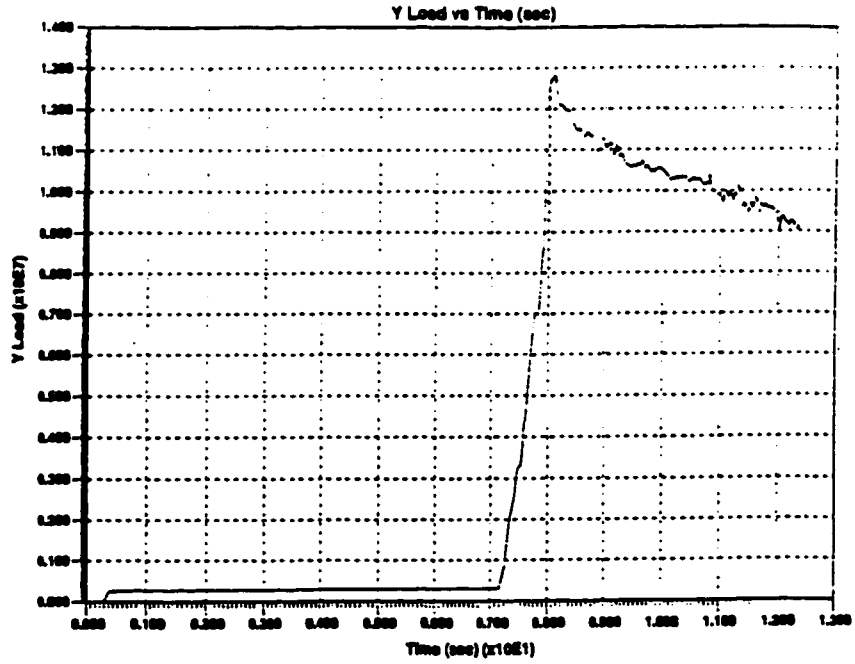

(b)

Figure 6.5 Comparison of simulation results of: (a) 10% Al_2O_3/6061 Al and (b) 10% Al_2O_3/2618 Al. (T_{billet}=450 °C, ram speed=2.6mm/s, R=31)

7. CONCLUSION

- The flow stress of the MMCs is significantly higher than the alloy at low temperatures but the difference diminishes as temperature increases. The flow stress as a function of strain rate and temperature was suitably represented by the hyperbolic sine equation for 6061 Al, 10%Al_2O_3/6061, 15%SiC/6061 and 20%Al_2O_3/6061. The constitutive equations were sufficiently accurate to be used as material input in the finite element model.
- The simulation results showed that an increase in billet temperature, a reduction in ram speed or a reduction in extrusion ratio, all had the effect of reducing the peak ram load. Maximum temperature reached during an extrusion increased with an increase in initial billet temperature, ram speed, or extrusion ratio. Maximum strain rate and maximum extrudate velocity increased with an increase in ram speed and extrusion ratio and were not influenced by percent reinforcement or initial billet temperature. The load versus stroke curves decreased more rapidly and had a higher peak as percent reinforcement increased due to greater deformation heating.
- As a result of varying the input conditions, interpolation can be used to determine a desired output. The results of the simulations were validated by comparing the results to actual real-life extrusions and other researchers' modeling results. Peak load predictions agree within ten percent of the simulations and plant trials performed at UBC.

- Discrepancies between the peak ram load in the present model and plant trials was primarily due to the assumption that the extrusion press was rigid. Variations in simulation results between the present work and other researchers was due to different input and boundary conditions.
- The model is suitable for macroscopic analysis, such as the development of extrusion limit diagrams, but is not sophisticated enough to predict deformation at the microscopic level such as grain deformation.
- Future work could entail refining the model to include press deflection and possibly microstructural deformation. Varying the friction conditions could also be undertaken to study its effect on the flow pattern. Die geometry could be changed from a square die to a more tapered die design.

REFERENCES

1. D.R. Askeland, **The Science and Engineering of Materials**, 3rd ed, PWS Publishing Company, Boston, 1994, pp 382-392.
2. P.Sakaris, "Hot Deformation Behaviour of SiC_p/Al Composites and Their Matrices and an Al-Mg-Si Alloy", Masters Thesis, Concordia University, April, 1993, pp 56-87.
3. H.J. McQueen and P. Sakaris, "Mechanical Shaping of Metal Matrix Composites", **Composite Structures and Materials**, S.V. Hoa and R. Gauvin eds., Elsevier Applied Science, London, 1992, pp 297-306.
4. D.J. Lloyd, "Metal Matrix Composites- An Overview", **Advanced Structural Materials**, Pergamon Press, Oxford, 1989, pp 1-21.
5. S. Krishnamurthy, Y.W. Kim, G. Das, F.H. Froes, "Applications of RS/PM to the Processing of Metal Matrix Composites", **Metal & Ceramic Matrix Composites: Processing, Modeling & Mechanical Behavior**, TMS, Pennsylvania, 1990, pp 145-155.
6. A.H. Nakagawa and M.N. Gungor, "Microstructure and Tensile Properties of Al_2O_3 Particle Reinforced 6061 Al Cast Composite", **Fundamental Relationships Between Microstructures and Mechanical Properties of Metal Matrix Composites, TMS, Pennsylvania**, 1990, pp 127-143.
7. J.E. Allison and G.S. Cole, "Metal Matrix Composites in the Automotive Industry: Opportunities and Challenges", **JOM**, vol 45, Jan. 1993, pp 19-24.

8. W. Dixon, "Extrusion of Particulate-Reinforced Aluminum-Based Metal Matrix Composites", **Proc. 5th Intnl. Aluminum Extrusion Technology Seminar**, The Aluminum Association, Washington, 1992, vol. 1, pp 429-436.

9. J. Kaneko, M. Sultan and R. Horiuchi, "Homogenization Heat Treatment and Hot Workability of the Ingots of Al-Mg-Si Alloys", **Z. Metallkde**, vol. 67, 1975, pp 8-15.

10. M. Isogai and S. Murakami, "Development and Application of Aluminum Extrusion for Automotive Parts, Mainly Bumper Reinforcement", **J. Mat. Proc. Tech.**, vol 38, 1993, pp 635-654.

11. H.J. McQueen, W.A. Wong and J.J. Jonas, "Deformation of Aluminum at High Temperature and Strain Rates", **Can. J. Phys.**, vol. 45, 1967, pp 1225-1234.

12. H.J. McQueen and W.J.M. Tegart, "The Deformation of Metals at High Temperatures", **Sci. Am.**, vol.232, no.4, April 1975, pp 116-124.

13. G.E. Dieter, **Mechanical Metallurgy**, McGraw-Hill Inc., New York, 1986, pp 212-219 and pp 503-539.

14. X. Xia, P. Sakaris and H.J. McQueen, "Hot Deformation, Dynamic Recovery and Recrystallization Behaviour of a SiC_p/6061 Al Composite", **Mat. Sci. Tech**, vol 10, 1994, pp 487-496.

15. X. Xia and H.J. McQueen, "TEM and SEM Investigation of Dynamic Recovery and Recrystallization in Hot Deformed Metal Matrix Composites", **Microstructural Science**, vol. 22, 1995, pp 285-296.

16. H.J. McQueen, X. Xia and M. Myshlyaev, "Dynamic Recrystallization in Hot Working of Aluminum Alloy Matrix Particulate Composites", **Third International Conference on Recrystallization and Related Topics**, Monterey, 1996, (in press).

17. H.J. McQueen, E. Evangelista, M.E. Kassner, "The Classification and Determination of Restoration Mechanisms in Hot Working of Aluminum Alloys", **Z. Metallk.**, vol.82, 1991, pp 336-345.

18. H.J. McQueen and K. Conrod, Recovery and Recrystallization in the Hot Working of Al Alloys", **Microstructural Control in Al Alloy Processing**, TMS-AIME, Warrendale, PA, 1986, pp 197-220.

19. R.W. Hertzberg, **Deformation and Fracture Mechanics of Engineering Materials**, John Wiley and Sons, New York, 1989, pp 125-145.

20. E. Morelli, A.A Ghilarducci, S.E.U. Pereyra, "Relation between Fabrication Parameters and Grain Boundary Internal Friction Peaks in Commercial Al-Mg-Si Alloys", **J. Alloys Comp.**, 211/212, 1994, pp 484-488.

21. A. Espedal, H. Gjestland, N. Ryum, H. J. McQueen, "Hot Deformation of Al-Mg-Si Alloys", **Scand. J. Metal.**, vol. 18, 1989, pp 131-136.

22. T.J. King, W.Z. Misiolek, R.N. Wright, "Microstructural Evolution on Billet Heating Practices of 6xxx Aluminum Simulating the Extrusion Process", **Advances in Hot Deformation Textures and Microstructures**, (J.J. Jonas, T.R. Bieler and K.J. Bowman, eds.), TMS, Warrendale, PA, 1993, pp 267-279.

23. Z. Xiong, L. Geng and C.K. Yao, "Investigation of High-Temperature Deformation Behavior of a SiC Whisker Reinforced 6061 Aluminum Composite", **Composites Science and Technology**, vol.39, 1990, pp 117-125.

24. H.J. McQueen and O.C. Celliers, "Application of Hot Workability Studies to Extrusion Processing: Part II. Microstructural Development and Extrusion of Al, Al-Mg, and Al-Mg-Mn Alloys", **Can. Met. Quart.**, vol. 35, 1996, pp 305-319.

25. H.J. McQueen, "Micromechanisms of Dynamic Softening in Aluminum Alloys During Hot Working", **Hot Deformation of Aluminum Alloys**, T.G. Langdon and H.D. Merchant eds., TMS-Aime, Warrendale PA, 1991, pp 31-54 and 105-120.

26. R.J. Arsenault, L. Wang and C.R. Feng, "Strengthening of Composites Due to Microstructural Changes in the Matrix", **Acta. Metall. Mater.**, vol. 39, 1991, pp 47-57.

27. J. Wang, M. Furukawa, Z. Horita, M. Nemoto, Y. Ma, T.G. Langdon, "The Age-Hardening Characteristics of an Al-6061/Al_2O_3 Metal Matrix Composite", **Metal. Mat. Trans. A**, vol. 26A, 1995, pp 581-586.

28. Alexander and Brewer, **Manufacturing Properties of Metals**, D.VanNostrand Company Ltd, London, 1963, pp 201-257.

29. **Metals Handbook Ninth Edition, Forming**, ASM International, Metals Park, Ohio, 1979, pp 315-326.

30. M. Furukawa, J. Wang, Z. Horita, M. Nemoto, Y. Ma and T.G. Langdon, "An Investigation of Strain Hardening and Creep in an Al-6061/Al_2O_3 Metal Matrix Composite", **Metal. Mat. Trans. A**, vol. 26A, 1995, pp 633-638.

31. S. Zajac, L.O. Gullman, and A. Johansson, "Hot Deformation Behaviour and Extrudability of AA 6005 Aluminum Alloy Microalloyed with Manganese", **The 3rd Intl. Conf. on Aluminum Alloys**, vol. II, The Norwegian Institute of Technology, Trondheim, 1992, pp 133-138.

32. W.C. Chen, "Extrusion of Alumina Particulate Reinforced Matal Matrix Composites", PhD Thesis, University of British Columbia, Dec. 1994, pp 65-93.

33. K.T. Yang, "Thermal and Friction Effects in Metal Extrusion and Wire Drawing", **Thermomechanical Aspects of Manufacturing and Materials Processing**, Hemisphere Publishing Corporation, Washington, 1992, pp 245-262.

34. Q. Ouyang, W. Wang and G. Zhang, "The Deformation Behavior of SiC Particle Reinforced Aluminum Composites and Its Influence on Properties", **39th International SAMPE Symposium**, Society for the Advancement of Material and Process Engineering, 1994, pp 659-670.

35. S. Brusethaug and O. Reiso, "Extrusion of SiCp Reinforced Al-Alloys", **Metal Matrix Composites- Processing, Microstructure and Properties**, RISO National Laboratory, Denmark, 1991, pp 247-255.

36. W.W. Krysko and M.W. Lui, **J. Mat. Tech.**, 1970, pp 83-89 & pp 127-137.

37. K. Laue and H. Stenger, **Extrusion**, ASM, Ohio, 1981, pp 1-42.

38. H.J. McQueen and O.C. Celliers, "Application of Hot Workability Studies to Extrusion Processing Part I, Extrusion Control Parameters and Constitutive Equations", **Materials Forum**, vol. 17, 1993, pp 1-13.

39. J.A. Schey, **Tribology in Metal Working- Friction, Lubrication and Wear**, ASM, Ohio, 1983, pp 408-431.

40. M.K. Surappa, "On the Nature of Particle Flow during the Extrusion of Cast 6061 Al/SiC_p Composites", **J. Mat. Sci. Let.**, vol.12, 1993, pp1272-1273.

41. B. Avitzur, "Die Design for Hydrostatic Extrusion", **Manufacturing Engineering Transactions**, vol. II, Society of Manufacturing Engineers, Michigan, 1973, pp 177-198.

42. E. Hinton and D. Owen, **An Introduction to Finite Element Computations**, Pineridge Press Limited, Swansea, I.K., 1979, pp 1-6.

43. A. Behrens, H. Schafstall, D. Landgrebe, "Semi-Automatic Rezone Algorithm for the Simulation 2-D Axisemmetric Extrusion Processes with FEM." **J. Mat. Proc. Tech**, vol 45, 1994, pp 671-676.

44. D. Bhattacharyya, P.J. Richards and A. Somashekan, "Modelling of Metal Extrusion Using the PHOENICS Package", **J. Mat. Proc. Tech**, vol 35, 1992, pp 93-111.

45. E.G. Thomsen, "Plane Strain and Axially Symmetric Velocities and Pressures in Extrusions", **Proc. Conf. on the Properties of Materials at High Rates of Strain**, The Institute of Mechanical Engineers, London, 1957, pp 77-85.

46. R. Akaret, "A Numerical Analysis of Temperature Distribution in Extrusion", **J. Inst. Metals**, vol. 95, 1967, pp204-211.

47. G. Grasmo, K. Holthe, S. Storen, and H. Valberg, "Modelling of Two-Dimensional Extrusion", **Proc. 5th International Aluminum Extrusion Technology Seminar**, The Aluminum Association, Washington, 1992, pp 367-376.

48. C.H.J. Davies, W.C. Chen, E.B. Hawbolt, I.V. Samarasekera, J.K. Brimacombe, "Particle Fracture During Extrusion of a 6061 /Alumina Composite", Scripta Metall. Mater., vol. 32, 1995, pp 309-314.

49. H.J. McQueen, J. Charlton, and E.M. Herba, "Constitutive Analysis and Extrusion Modeling of Aluminum Matrix Composites", 1996, (in progress).

50. S. Fulop, K. Cadien, M.J. Luton and H.J. McQueen, "A Servo-Controlled Hydraulic Torsion Machine for Hot Torsion Studies", J. Test. Evaluation, vol. 5, 1977, pp 419-426.

51. P. Sakaris and H.J. McQueen, "Comparative Hot Workability of SiC_p/A356 and SiC_p/6061 Al Composites and Their Matrices", Metal Matrix Composites-Fabrication and Technology, CIM, Pergamon Press, Oxford, 1992.

52. X. Xia, H.J. McQueen and P. Sakaris, "Deformation and Microstructure of Al_2O_3 Particle Reinforced 6061 Al Composite", Developments and Applications of New Ceramics and Metal Alloys, CIM, Montreal, 1993, pp 135-142.

53. X. Xia, H.J. McQueen and P. Sakaris, "Hot Deformation Mechanisms in a 10% Al_2O_3 Particle Reinforced 6061 Al Matrix Composite", Scripta Metall. Mater., vol. 32, 1995, pp 1185-1190.

54. Klaus- Jurgen Bathe, Finite Element Procedures, Prentice Hall, New Jersey, 1996, pp 143-147.

55. K. Raznjevic, Handbook of Thermodynamic Tables and Charts, Hemisphere Publishing Corporation, Washington, 1976, pp 50-51.

56. J.R. Pickens, T.J. Langan, R.O. England and M. Liebson, "A Study of the Hot Working Behaviour of SiC-Al Alloy Composites and Their Matrix Alloys by Hot Torsion Testing", **Met. Trans. A**, vol. 18A, 1987, pp 303-312.

57. D. Zhao and P. Chaudhury, "Hot Compression Behaviour of Wrought Al 6061", **Aluminum Alloys, Physical and Mechanical Properties**, (ICAA 4), pp 426-433.

58. C. Davies, E. Hawbolt, I. Samarasekera, and J. Brimacombe, "Constitutive Behavior of Composites of Al 6061 and Alumina", **Metal. Mat. Trans**, Sept. 1995.

59. E.M. Herba and H.J. McQueen, "High Temperature Deformation of 6061 Al with Comparison to 6201 Al Alloy", **Hot Workability of Steels and Light Alloys-Composites**, Met. Soc. CIM, Montreal, 1996, pp 53-60.

60. H. Valberg and T. Malvik, "An Experimental Investigation of Material Flow Inside the Bearing Channel in Aluminum Extrusion", **Intnl. J. Prod. Tech.**, vol. 9, 1994, pp428-463.

61. **Metals Handbook Ninth Edition**, Volume 2, **Properties and Selection: Nonferrous Alloys and Pure Metals**, ASM International, Metals Park, Ohio, 1979, pp 88-117.